BRNO UNIVERSITY OF TECHNOLOGY
VYSOKÉ UČENÍ TECHNICKÉ V BRNĚ

CENTRAL EUROPEAN INSTITUTE OF TECHNOLOGY BUT
STŘEDOEVROPSKÝ TECHNOLOGICKÝ INSTITUT VUT

CUSTOMIZED HYBRID BIOSCAFFOLDS FOR BONE REGENERATION

INDIVIDUALIZOVANÉ HYBRIDNÍ PODPŮRNÉ STRUKTURY PRO REGENERACI KOSTNÍ TKÁNĚ

DOCTORAL THESIS
DIZERTAČNÍ PRÁCE

AUTHOR AUTOR PRÁCE	Ing. Přemysl Šťastný
SUPERVISOR ŠKOLITEL	prof. Ing. Martin Trunec, Dr.

BRNO 2020

I hereby confirm that the doctoral thesis titled „*Customized hybrid bioscaffolds for bone regeneration*“ was work up on my own, using published data and informations as well as author´s original results.

………………………………….. …………………………

Date Signature

Abstract/Abstrakt

The doctoral thesis titled *"Customized hybrid bioscaffolds for bone regeneration"* is divided into two parts. The first part tries to reveal the theoretical background of a bone-to-implant interaction and the current state of the art in the research of calcium phosphate materials and calcium phosphate-based implants for bone tissue engineering. The customization concept and a careful selection of phase composition represents two main points of the second, experimental, part of the doctoral thesis. The customization concept in this work is not only just a simple shape and dimension optimization process of an implant, but additionally attention is paid to the microstructural features, phase composition and phase distribution allowing the rational design and a production of tailor-made materials for dinstinct medical applications. Cellular and biological responses to the ceramic materials were evaluated both by *in-vitro* and *in-vivo* tests and were discussed against the material composition and the microstructural features. The doctoral thesis shows how a fundamental understanding of physical and chemical properties of the material under question can help to design implants material with an outstanding biological response. The *in-vivo* application of the customized implant and its comparison with the current gold standard bone graft material – bone autograft is a unique and valuable outcome of the doctoral thesis.

Doktorská práce s názvem *Individualizované hybridní podpůrné struktury pro regeneraci kostní tkáně* je rozdělena do dvou částí. První část si klade za cíl ukázat vzájemný vztah mezi implantovaným materiálem a kostní tkání a současný stav poznání v oblasti vývoje matriálů na bázi fosforečnanů vápenatých a z nich vyráběných implantátů pro regeneraci kostní tkáně. Koncept individualizace a pečlivého výběru fázového složení implantátu představuje stěžejní body druhé části práce. Individualizace v této práci není chápána jako pouhé dosažení tvarové a rozměrové přesnosti implantátu. Velká pozornost byla věnována mikrostrukturním detailům, fázovému složení a distribuci jednotlivých fází, což umožňuje připravit specifický materiál na základě zamýšlené aplikace. Biologická odezva na připravené materiály byla vyhodnocena pomocí *in-vitro* a *in-vivo* testů. Doktorská práce ukazuje jak pochopení základních chemických a fyzikálních vlastností materiálu může pomoc při návrhu implantátu s vynikající biologickou odezvou. *In-vivo* aplikace navrženého materiálu a jeho srovnání s autograftním kostním štěpem, současným zlatým standardem, je jedinečným a cenným výstupem předložené práce.

Key Words/Klíčová Slova

Hydroxyapatite, tricalcium phosphate, bone healing, scaffolds, degradation

Hydroxyapatit, fosforečnan vápenatý, hojení kostí, scaffoldy, degradace

Bibliographical Citation

ŠŤASTNÝ, P. *Customized hybrid bioscaffolds and bone cemments for bone regeneration*. Brno: Brno University of Technology, Central European Institute of Technology BUT, 2020. 100 s. Supervisor prof. Ing. Martin Trunec, Dr.

Acknowledgement

I would like to pay a tribute to my supervisor Prof. Martin Trunec, who is always helpful and who brings the constructive criticism to my work. Furthermore, I would like to acknowledge all the colleagues who collaborated on the task to prepare novel hybrid ceramic material for a bone regeneration. I would like to deeply acknowledge the group of doc. Lucy Vojtová, being responsible for biopolymer filling of ceramic implants. The CT images of the ceramic foams and the spine fusion were provided by the group of Prof. Jozef Kaiser. Mechanical testing of porous ceramics was done in collaboration with Ing. Zdeněk Chlup from Institute of Physics of Materials, Czech Academy of Sciences. Ceramic foams after simulated degradation were tested in collaboration with the team of Ing. Radek Sedláček from Czech Technical University of Prague. *In-vitro* performance of ceramic materials was tested in collaboration with a group from Institute of Experimental Medicine, Czech Academy of Sciences, Prague, namely by RNDr. Věra Lukášová and Mgr. Michaela Rampichová. In-vivo tests were performed at Veterinari Research Institute Brno under supervision of MVDr. Martin Faldyna. All surgeries were performed by Prof. Ladislav Plánka and MUDr. Milan Krtička from University Hospital Brno supported by the other members of surgical team. It would not have been possible to accomplish such a broad and multidisciplinary research without all the people and the teams mentioned. Last but not least, I would like to deeply acknowledge Ceitec Nano Research Infrastructure and all operators who has supported me with the equipment trainings and the essential knowledge.

The doctoral research was supported by the following research grants:

Ministry of Health of the Czech Republic under the grant 17-31276A

Brno University of Technology under the grant STI-J-18-5307

Brno University of Technology, under the grant STI-J-17-4305

CEITEC Nano Research Infrastructure (MEYS CR, 2016-2019)

Contents

1 Introduction

Calcium phosphates (CaPs) have been researched by biologists, mineralogists, and chemists for decades. The reason is, among others, that CaP is one of the main building blocks of a bone matrix and the main inorganic compound of the bone matrix [1, 2]. CaPs are widely researched and tested as biocompatible and bioactive materials for bone regeneration [1, 3]. For over decades, the bioceramic materials based on calcium phosphates has become the first choice ceramic materials for bioactive coatings [4-8] and temporary bone replacements – bioceramic scaffolds [3, 9-18]. Although a lot of work has been done in this particular field, there is still a huge space for an improvement of our knowledge. This space, located mainly at the border between material and life sciences, needs to be filled.

The first mentions about studies related to CaPs can be found in the texts of Danish merchant and scientist Antonie Philips van Leeuwenhoeken from the 17th century. Leeuwenhoeken has been titled the father of microbiology and he was the scientist who had found small crystals of calcium phosphate mineral in dentine. The first recorded utilization of the CaP material as a bone replacement took place on the 20th of May in 1890 [19]. In that day, German surgeon Themistockles Gluck used an ivory embedded in calcium phosphate cement as a replacement for a knee joint. The surgery of a wrist joint followed in quick sequence. It is worth mentioning that the first patient with an artificial knee joint could walk pain-free 35 days after the surgery. The level of joint movement was preserved. Unfortunately, in a longer horizon, all replacements failed because of chronic inflammations. The first mention of an artificially synthethised CaP material used in medicin was recorded in 1920 [19]. Fred Houdlette Albee was the first surgeon who used artificial calcium material for a bone defects treatment. From that time a rapid devolepment has started.

Calcium phosphates (CaPs) consists of three essential elemets:

- Calcium (Ca)
- Phosphor (P)
- Oxygen (O)

Many CaPs have hydrogen (H) as a part of anion complex (HPO_4^{2-}) or hydroxy group (OH), which is the case of hydroxyapatite, $Ca_{10}(PO_4)_6(OH)_2$. The structures of some calcium phosphates consist of water molecules ($Ca(H_2PO_4)_2.H_2O$) in a crystallographic structure. Morever, CaPs can be substituted by ions as Sr^{2+}, F^-, Mg^{2+}, SiO_4^{4-}, CO_3^{2-} etc. [20, 21] Unsubstituted, stoichiometric CaPs can be derived from $CaO – P_2O_5$ [22] or $CaO – P_2O_5 – H_2O$ [23] phase diagrams. Based on the anion CaPs are divided into three basic groups – orthophosphates (PO_4^{3-}), pyrophosphates ($P_2O_7^{4-}$) and polyphosphates ($(PO_3)_n^{n-}$) [20]. Orthophosphates (Table 1) are materials used for the production of bioceramic implants preferentially, which is the case of this work as well.

The main goal of this doctoral thesis was to unveil the relationship between material characteristics of sintered calcium phosphate scaffolds and describe biological response to

these materials. This knowledge is then used for production of hybrid calcium phosphate scaffolds with enhanced biological properties. The first part of doctoral thesis reviews the current state of the art in the field of biocermics, focusing on their interaction with a host´s body and on the challenges inevitably connected with their use as the biomaterial. The research part of the doctoral thesis is focused on calcium orthophosphates. Porous calcium phosphate scaffolds with different phase compositions were prepared and investigated both from material and biological point of view. The multilevel implant customization was studied. The influence of microstructural features and a phase composition on biological response is discussed. Changes of mechanical properties under simulated *in-vivo* condition were investigated and discussed against the microstructural changes of the scaffolds. The phase evolution during sintering and the phase distribution on a grain level were investigated. Thanks to the collaboration with colleagues from life sciences and medicine, *in-vitro* and *in-vivo* trials were conducted. The *in-vitro* tests helped to find out the best composition of the ceramic scaffolds further used for a preparation of the hybrid bone scaffolds. The hybrid bone scaffolds were tested in an animal model. The results were compared with the results obtained from a control group treated with a current gold standard among the bone grafts – autologous bone grafts.

Table 1 Calcium orthophosphate family

Ca/P Molar Ratio	**Compound and abbreviation**	**Chemical formula**	**Solubility at 25°C (g/L), pH 7**
0.5	Monocalcium phosphate monohydrate (MCPM)	$Ca(H_2PO_4)_2.H_2O$	18
0.5	Monocalcium phosphate anhydrous (MCPA)	$Ca(H_2PO_4)_2$	17
1.0	Dicalcium phosphate dihydrate (DCPD)	$Ca(HPO_4).2H_2O$	0.088
1.0	Dicalcium phosphate anhydrous (DCPA)	$Ca(HPO_4)$	0.048
1.33	Octacalcium phosphate (OCP)	$Ca_8(HPO_4)\ (PO_4)_4.5H_2O$	0.0081
1.5	Tricalcium phosphate (alpha) (α-TCP)	$Ca_3(PO_4)_2$	0.0025
1.5	Tricalcium phosphate (beta) (β-TCP)	$Ca_3(PO_4)_2$	0.0005
1.2-2.2	Amorphous calcium phosphate (ACP)	$Ca_xH_y(PO_4)_z.nH_2O$ $n=3-4.5$	-
1.5-1.67	Calcium deficient hydroxyapatite (CDHA)	$Ca_{10-x}(HPO_4)_x\ (PO_4)_{6-x}(OH)_{2-x}$ $0<x<1$	0.0094
1.67	Hydroxyapatite (HA)	$Ca_{10}(PO_4)_6(OH)_2$	0.0003
1.67	Fluorapatite	$Ca_{10}(PO_4)_6F_2$	0.0002
1.67	Oxyapatite (OA)	$Ca_{10}(PO_4)_6O$	0.087
2	Tetracalcium phosphate (TTCP)	$Ca_4(PO_4)_2$	0.0007

2 State of the Art

2.1 Bone Biology

At least a basic knowledge of a bone biology is needed for a correct design of calcium phosphate scaffolds. The interdisciplinary origin of this task brings together groups of researchers with different scientific backgrounds. The connection of material sciences with biology and medicine brings new challenges. The purpose of this chapter is to summarize the basic knowledge about the bone biology. The summary should contribute to better understanding of the crucial biological processes by material scientists, which could help to define important parameters during development of bone scaffolds.

A bone is not just an internal scaffolding holding body in an upright position and an armour protecting internal organs. Bone tissue is the main storage of calcium and phosphor in every human body [24, 25]. Bone marrow produces new blood and contributes to a number of metabolic processes [26]. If we talk about bones as a connective tissue, then the bones are a perfect natural composite combining rigidity and strength with a certain degree of flexibility. Here we can see a big difference between sintered ceramic scaffolds and the bone. The natural bone is a composite material composed of an organic matrix (30 %) with embedded calcium phosphates deposits (70 %) [27]. The organic matrix is created mainly by type I collagen giving bone its elastic properties. Type I collagen is in an abundance (95 wt. % of the organic matrix), remaining 5 % are created by proteoglycans and noncolagenous proteins [25]. Calcium deposits, mainly hydroxyapatite and substituted hydroxyapatite in a form of platelets approximately 30 nm in size with a thickness around 4 nm are embedded in collagen matrix [3, 25, 27]. There are two types of bones from morphological point of view – cortical and cancellous. The cortical bone is dense, composed of tightly packed collagen fibres in a form of concentric lamellas. The structure of a cancellous bone is far less topographically organised. Differences mentioned reflect the purpose of these two kinds of bone tissues. Whereas the cortical bone supports a body and protects internal organs, the cancellous bone provides metabolic functions.

There are two ways of a skeleton formation (ossification). Direct (intramembranous) ossification takes place during fetal development by a direct transformation of mesenchymal cells to osteoblasts [25]. This process forms flat bones of the skull, mandibles and clavicles. Indirect (endochondral) ossification is the process of growth of long bones [25, 28]. All bones in a body, except these mentioned above, are created by endochondral ossification. Chondrocytes form a template of a long bone which is calcified (Figure 1 A – C [28]). The primary ossification centre occurs, a bone cavity is set, and bone cells modified calcified cartilage in the cavity to the spongy bone (Figure 1 D, E). Connective tissue forms periosteum around the bone connecting the bone with surroundings. The bone continues to grow as cartilage cells at the epiphyses divide. Then, at the last stage of prenatal development, the secondary ossification of epiphyses takes place (Figure 1 F, G) converting the cartilage to the spongy bone and creates growth plates (Figure 1 H). The growth plates are responsible for prolongation of the bone during growing (Figure 1 I). The growth of the bone is finished when the growth plates ossificate. There are three main stages of bone development during a lifetime [25]. The first stage is defined mainly by a bone modelling (age 0 – 20). The second stage is a remodeling stage, when the bone mass is kept constant (age 20 – 50). The last stage is a bone osteoporosis when the bone mass starts to decrease (age 50+).

Bone remodeling process keeps bones healthy. A normal remodeling process is a never-ending story during which an old bone is replaced by a new one. The remodeling process is of a high importance even during bone healing. Since CaPs ceramic materials are used as temporary bone replacements, the bone remodeling process is a crucial step in the case of wounds treated with CaPs grafts [29]. If the graft is supposed to be replaced by a new bone body must inevitably resorb ceramic structures. The resorption process is secured by anatomical structures called basic multicellular units (BMUs) (Figure 2 [30]) [2, 25]. The basic multicellular unit is composed of different type of cells – osteoblasts – bone forming cells, osteoclasts – bone resorbers, osteocytes – bone mechanosensors [2, 3, 24, 25, 28-31]

2.1.1 Bone Cells

This part will describe the role of individual bone cells during the remodelation process and their importance with respect to resorption of the ceramic grafts and a healing of damaged bones. After an implantation of artificial bone grafts a migration of the cells

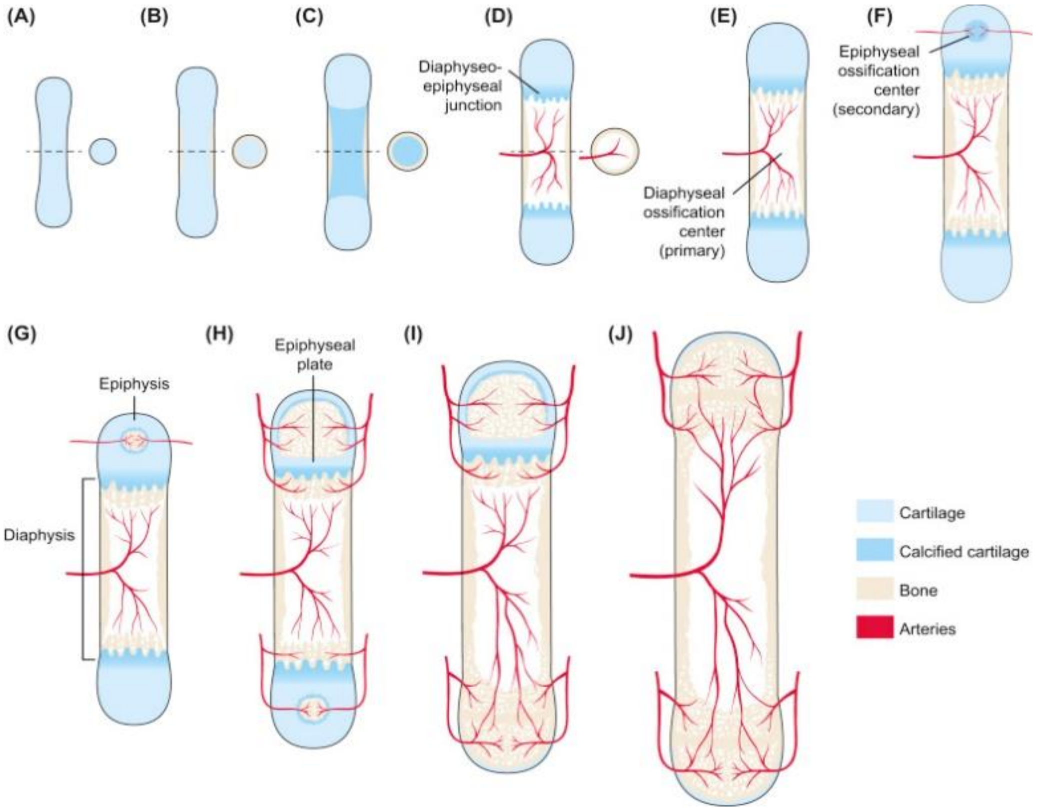

Figure 1 Endochondral ossification of a long bone

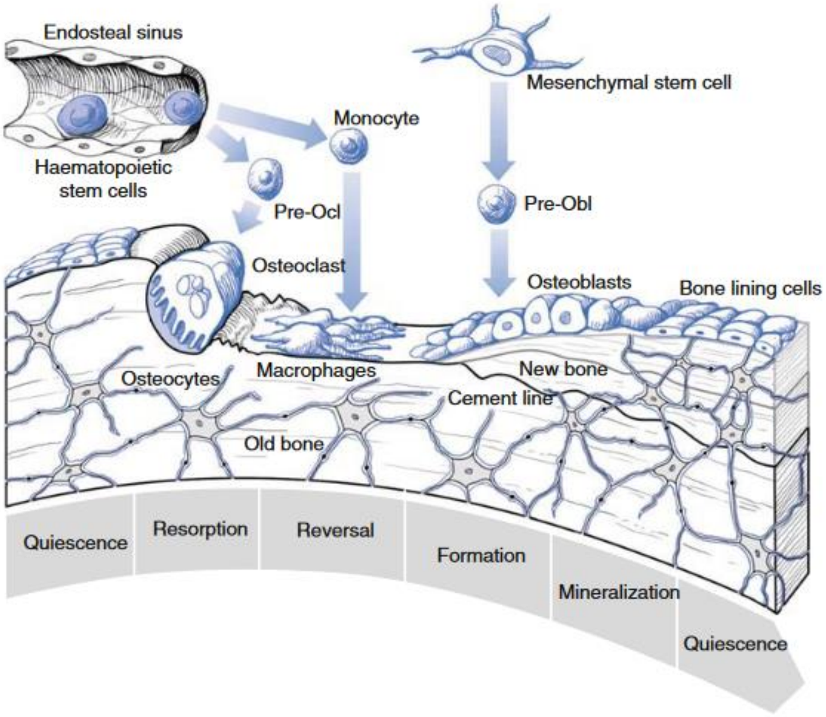

Figure 2 The basic multicellular unit during the bone healing

(including bone cells and their early stages) from surrounding tissues takes place followed by the bone formation and, ideally, the resorption of a bone graft.

Osteoclasts

Osteoclasts are cells playing the key role during the bone resorption. Osteoclasts originate from hematopoietic monocyte – macrophage lineage [2, 28]. The earliest recognized stage of preosteoclast cells comes from bone marrow. The preosteoclastic cells are recruited to the bone surface. They undergo a proliferation, differentiation, and fusion, forming multinucleated cells – the mature osteoclasts. The mature osteoclasts are polarized cells [2, 28]. There are two main domains in mature osteoclasts – an apical membrane domain (attaching to the bone) and a basolateral domain (away from the bone). This polarization plays a crucial role during an attachment, migration, and resorption of the mineralized bone matrix by osteoclasts. Once the resorption process is finished osteoclasts undergo a programmed cell death (apoptosis)[2, 28].

Process of the highest superiority before the bone degradation can take place is creation of a sealing zone (Figure 3 [28]) [28]. The sealing zone separates surrounding environment from a resorption lacuna under the osteoclast. There is a membrane domain located within the boundaries of sealing zone called ruffled border. The purpose of the ruffled border is to release hydrolytic enzymes and degrades the mineralized bone matrix by an acidification of the environment bordered with the sealing zone[25]. It is worth mentioning that the sealing zone is created only in a direct contact with the mineralized extracellular matrix. The osteoclasts binds via $\alpha_v\beta_3$ integrins to noncollagenous bone proteins – mainly sialoprotein and osteopontin [2, 32].

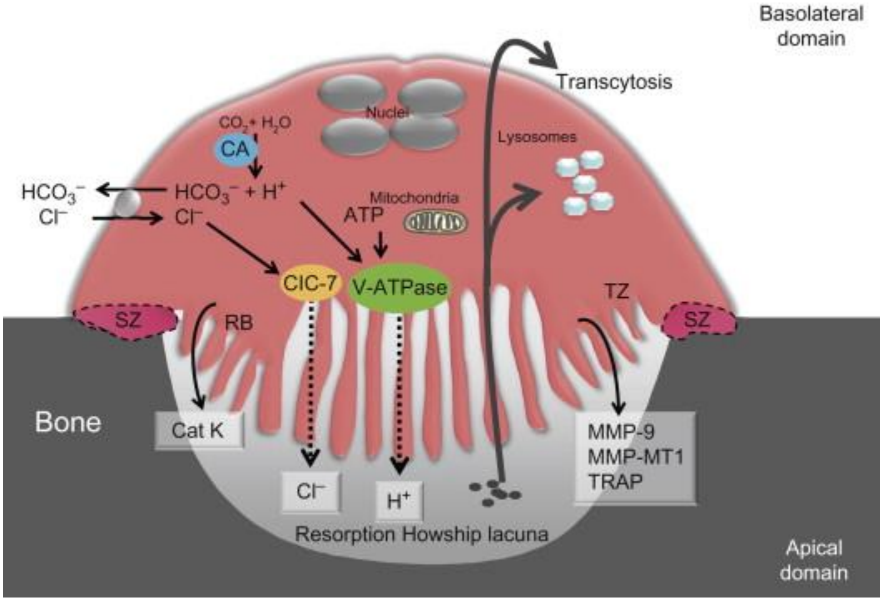

Figure 3 The osteoclast sealed on a bone surface. SZ – sealing zone, RB – ruffled border.

Osteoblasts

Osteoblasts are big cuboidal cells with pronounced Golgi apparatus and rough endoplasmic reticulum. Osteoblasts are responsible for the formation of the bone matrix and its mineralization [2, 25, 28]. Osteoblasts originate from mesenchymal stem cells [25]. A maturation of osteoblasts is governed via a highly sophisticated signaling pathway. During the bone formation osteoblasts express high levels of alkaline phosphatase (ALP) and osteocalcin [28]. Collagen I type is secreted by osteoblasts in an abundance. A mineralization of the bone matrix is a two-stage process [2]. The first stage is called vesicular phase. During vesicular phase the matrix vesicles are released from apical membrane domain. The matrix vesicles bind to proteoglycans and other organic compounds. A negative charge of proteoglycans immobilizes calcium ions. Calcium ions cross the membrane of matrix vesicles and combine with phosphates released by ALP activity. The outcome is precipitation of HA crystals. The second stage of the mineralization is fibrillar stage when the vesicles rupture and HA is deposited in the organic matrix. Upon completion of bone matrix formation some osteoblasts are entrapped in the newly formed bone matrix becoming osteocytes [25, 28]. The rest of the osteoclasts either change to bone lining cells or undergo apoptosis [25, 28].

Bone Lining Cells

Bone lining cells are flat cells on the bone surface. They originate from osteoblasts and they can be reactivated if they are needed [2, 25, 28]. Their exact function is not absolutely clear. Bone lining cells are connected to osteocytes via gap junctions. Lining cells probably play an important role during the first stage of the remodeling creating a canopy over the area where BMU is needed. The canopy separates BMU from surrounding space, creating an environment suitable for osteoclasts and osteoblasts maturation (Figure 4 [28]).

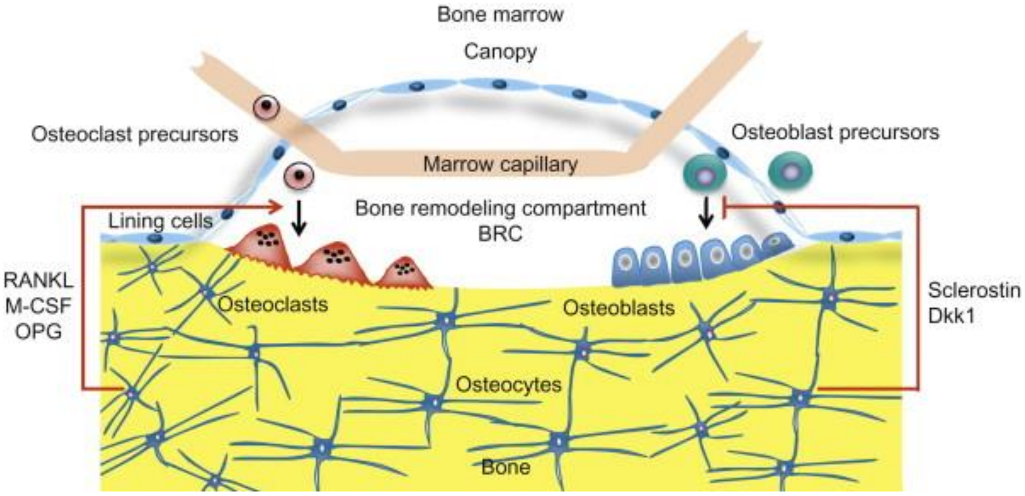

Figure 4 The bone remodeling compartment (BRC) created by the bone lining cells

Osteocytes

Osteocytes are osteoblasts entombed in a bone matrix [2, 25, 28]. They are the most abundant bone cells. They were supposed to be cells without a specific activity. The latest researches have shown that osteocytes are very active instead. Enclosed in lacunas, cytoplasmatic dendritic processes run through canaliculies connecting the adjacent osteocytes creating neuron-like structures. Osteocytes serve as conductors of bone remodeling [28]. They down or upregulate the activity of osteoclasts and osteoblasts. Osteocytes sense a mechanical loading and detect microdamages of a bone matrix. The microdamages are detected due to dense network of connection between the adjacent osteocytes. A disruption of the connection or apoptosis of neightboring osteocytes is recognized and osteocytes in surroundings can release chemical signals [33]. The response to changes in a level of mechanical loading or level of circulating ions and hormones is up or down regulation of factors secretion (osteoprotogerin, RANKL or sclerotosin [28]). These factors directly affect the activity of osteoblasts and osteoclasts, keeping the bone tissue healthy.

Bone Healing

Bone fractures and other mechanical or surgical damages of bones lead to a bone matrix discontinuity. The discontinuity sensed by a complex signaling mechanism provided by osteocytes results in the bone reparation. This mechanism is valid even for surgeries involving utilization of bone grafts. Bone grafting procedures result in a state when continuity of the bone is disrupted by a graft inserted between bone endings. Subsequently, the bone healing takes place restoring a normal anatomy and function of the bone. The bone healing (Figure 5 [28]) is a complex and unique process composed of several steps [28]:

1. Infalammatory response
2. Soft callus formation
3. Hard callus formation
4. Bone remodeling

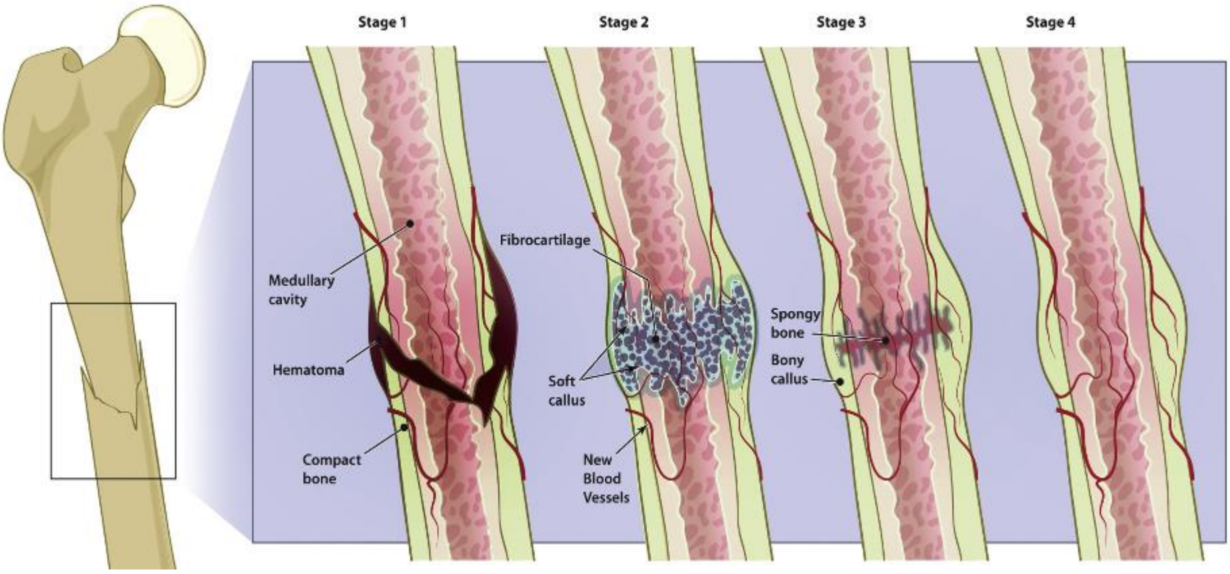

Figure 5 Bone healing process

An injured bone violates surrounding tissues and blood vessels. The wounded site is surrounded by a hematoma. During the first few hours after injury, several types of various factors are released –platelets, macrophages, leukocytes. Inflammatory period [2, 25, 28, 34-36] peaks within 24 hours after injury and lasts for 7 days. The following step is a formation of soft callus [28, 36]. Cells at the injured site are stimulated to restore disrupted vessels and intracellular matrix. The hematoma is gradually replaced by a fibrovascular tissue –soft callus. Soft callus stabilizes dislocated bone endings. This period during which soft callus is formatted peaks within 7 and 10 days after an injury. The stabilized site of an injury undergoes a change from the soft to hard callus by endochondral ossification [2, 28, 35]. The calcified cartilage is then replaced by a woven bone. The woven bone is remodeled by BMU [2, 25, 35, 36]. Osteoclasts decompose the woven bone and a new bone is formed by an osteoblast activity. This period can take several years to be accomplished and cannot be fully successful, mainly at a higher age [37].

2.1.2 Bone Grafts

The bone grafts should be a nomenclature for natural materials used as bone space fillers [38]. According to a type of material bone grafts transplantation (living cells) or implantation (non-living cells) can occurs. Regarding to this rule, nonviable materials should be called implants. However, precise use of this terminology is not common even in a literature [39]. Therefore, as bone grafts either natural or artificial (synthetic) materials used as space fillers are called. With more than two millions of transplantations and implantations worldwide in 2013 [40] and as the second most common tissue transplantation in the reconstructive and trauma surgeries in the USA (2019) [41] the bone grafts are considered to be essential treatment tools.

The ideal bone graft materials must satisfy following demands [38, 39]:

1. Osseointegration
2. Osteoconduction
3. Osteoinduction
4. Osteogenesis

The osseointegration is defined as an ability of the graft to be chemically bonded to a bone surface without any intervening fibrous tissue being formed [39].

The osteoconduction is defined as an ability to support a bone growth on the graft surface [39].

The osteoinduction is defined as an ability to induce a differentiation of pluripotential stem cells from surrounding tissue to the osteoblastic phenotype [39].

The osteogenesis is a formation of a new bone by osteoblastic cells attached on the graft material [39].

Natural Bone Grafts

Natural bone grafts are sorted to groups according their origin and a type of the bone they are harvested from [38, 39, 41, 42]. The natural grafts can be harvested from the same living organism - autologous grafts (autogenous, autografts) [38, 39, 41-43], from different organism but same species (allografts)[38, 39, 41-43] or from different species (xenografts) [42].

Autografts

The autografts are the gold standard among grafting materials [38, 44, 45]. As the only group autografts satisfy all demands required from the ideal bone grafts [39]. The autografts are harvested from the same body as they are implanted afterward. The most commonly, the autografts are harvested from iliac crests, femurs, proximal tibias and ribs [40, 41]. They can be in a form of cancellous, cortical, cortical – cancellous or bone marrow aspirate (BMA) [41].

Since they are from the same body, they introduce a low risk of immunological rejections [41, 46]. The autografts contain mature osteoblasts, osteoclasts and osteocytes, body morphogenic proteins and growth factors [41]. Even though survival rate of mature osteoblasts after transplantation is low, there are still great numbers of preosteoblastic cells surviving grafting and transplantation. The revascularization and remodelling on an acceptor-site is affected mainly by method of a graft harvesting and handling [42, 47]. Handled carefully, the vascularization can progress in a rate of 0.2 – 0.4 mm/day [48]. The vascularization of traumatised grafts is slowed down to 0.15 – 0.3 mm/day [48]. The vascularization and remodelling are further dependent on the type of autograft. Faster vascularization and remodelling are observed in the case of cancellous grafts [49]. On the other hand, cortical grafts possess an excellent mechanical strength. Vascularized and non-vascularized form of cortical grafts are utilized in trauma surgeries and post-trauma treatments [50]. The non-vascularized bone grafts are preferred for wounds not larger than 6 cm [51]. Disadvantages of the autologous bone grafts are following: infections, donor-site morbidities, the second traumatised sites, limited availabilities and prolonged surgical times [41, 42, 44, 45, 51, 52].

Allografts

The allografts introduce an alternative to the autografts. They are harvested from the same species but a different organism [42]. The allografts are normally harvested from tibias, femurs, ribs or iliac crest of living or non-living donors [40, 42]. The allografts are harvested as structural and non-structural (morselized) types, available as fresh-frozen, freeze-dried frozen or demineralized and freeze-dried grafts [40]. The fresh allografts are rarely used due to big risk of an immunological rejection [53]. To avoid virus transfers, donors must undergo thorough screening [54]. The lowest possibility of viral infection and immunological rejections are in the case of the demineralized bone matrix grafts where mineralised matrix is extracted by a leaching in acids. The allografts are usually sterilized by gamma irradiation [55]. The gamma sterilization deactivates proteins and kill dangerous agents, unfortunately affecting *in-vivo* performance in a negative sense as well. The allografts, even thoroughly screened ones, still pose risk of viral infection (hepatitis B, C, HIV). But it is worth mentioning that only two cases of HIV transfer were noted from 1989 to 2013 [40]. More common complications are related to inflammations, non-unions and fractures of treated sites [53]. Compared to autografts, allografts are usually available even in large quantities and can be kept frozen in stock.

Xenografts

Xenograft are bone grafts harvested from different species [42]. This group contains bone like minerals derived from corals and algae as well. The most researched xenograft material is deproteinized bovine bone [56-58], widely used in dentistry. Protein extraction during deproteinization prevents immunological rejections of grafts on the acceptor site. The xenografts provide mainly osteoconductive properties [42]. The most discussed feature of xenografts is their resorption. Deproteinization extract all proteins, so arginine-glycine-asparagine sequence is missing [42]. The Arg-Gly-Asp sequence is crucial for osteoclasts attachment and the bone graft resorption [32]. In case of natural bone, this sequence is available mainly in bone sialoprotein, osteopontin, and in a lower amount in collagen I [59, 60]. Xenografts can be harvested in an abundance and stored for a long time. The most common disadvantages are linked with their interspecies origin and a poor *in-vivo* performance [61, 62].

2.2 Artificial Bone Grafts

As mentioned before, bones are the second most transplanted body material after blood [41]. Development of synthetic bone graft materials with characteristics at least close to the current gold standard in grafting – autologous bone grafts [38, 44, 45], would be highly appreciated. If we consider a material owing all appreciated characteristics of autografts related to bioactivity and *in-vivo* performance, we must ask: Which negatives of autografts could be improved by a synthetic material? The main disadvantage related to autografts is their harvesting [42, 47, 52]. The graft harvesting lead to secondary wounds at donor sites and means prolonged surgical time [41, 42, 44, 45, 51, 52]. Volume of autograft material is also limited. *In-vivo* performance of graft is dependent on harvesting techniques [63]. Grafting procedure itself can result in traumatised graft material with deteriorated properties [42, 47]. In case of theoretical synthetic graft material, completely comparable with autografts, at least logistic issues can be solved instantly. Theoretically, the grafting material in stock can be utilized on an operational theatre within few minutes. Prepared artificially, there are no restrictions related to material volume, shapes or harvesting procedures. It means, the development of synthetic bone graft material with, at least, similar properties to the autografts would instantly remove the problems associated with the logistic procedure hidden behind the graft harvesting and delivery.

Over the last decades, many types of synthetic graft materials have been tested [6], ranging from polymer materials [64-69] to metals [70-73] and ceramics [3, 12-15]. Ceramics and cements based on calcium orthophosphates seems to be auspicious. There are no reports on systemic toxicity or negative immune responses *in-vivo*. Calcium orthophosphates are biocompatible allowing osteointegration and osteoconductivity. As all synthetic graft materials, osteoinductive properties of pure calcium phosphates are arguable [39, 74] mainly attributed to the structural features allowing an adsorption of different factors on the surface of ceramics [75-78]. The osteoinductivity of calcium phosphates can be "incorporated" using proteins and similar factors [16, 79-83]. Mechanical characteristics of sintered calcium orthophosphates and calcium orthophosphates cements are not top ranked [10, 74, 84, 85]. Low mechanical properties are further deteriorated if the materials are utilized porous under body conditions [17]. Porous calcium orthophosphate materials are often called scaffolds. Porous structures are not designed as long-term implants. The main idea behind the bioceramic scaffolds is their short time utilization as a scaffolding assisting during a new bone formation. The scaffolding does not act only as a mechanical support, but as a stockpile of essential minerals for bone development as well. Considering the mechanical support, structure of the scaffolds must be able to withstand loadings associated with handling and implantation techniques.

2.2.1 *Ceramic Materials for Porous Bone Scaffolds*

There are several biocompatible ceramic materials currently used as ceramic scaffolds [3, 14, 86-90]. Only the most promising bioactive ceramic materials based on calcium orthophosphates are going to be discussed in this part focusing on their physical, chemical, and biological properties.

Hydroxyapatite

Hydroxyapatite (HA) has been extensively studied and used for more than 40 years [1, 91-93]. The exact chemical formula of crystalline hydroxyapatite is $Ca_{10}(PO_4)_6(OH)_2$. Calcium to phosphorous ratio is $Ca/P = 1.67$. The crystal structure of HA belongs to hexagonal crystallographic system, space group $P6_3/m$. Nanocrystalline HA is the main inorganic part of bone tissue [3, 25, 28]. HA can be extracted from natural sources - eggshells, bones, sea corals and seeds [91, 94-96]. Being extracted from natural sources hydroxyapatite composition is enriched with variety of elements [96]. Nonstoichiometricity and/or doping of HA can significantly affect *in-vivo* performance of the materials. Hydroxyapatite is prepared mostly by solid state synthesis [97], hydrothermal synthesis [98, 99] or precipitation from solutions [100, 101]. To mimic naturally occurring apatites crystal lattice of the HA can be substituted by variety of elements [20, 21].

The solid state synthesis of hydroxyapatite are high temperature synthesis when suitable reagents ($CaHPO_4$, $Ca(OH)_2$, $Ca_3(PO_4)_2$) reacts creating HA and gas products. Higher partial pressure of H_2O in a reactor is recommended, otherwise thermal decomposition of HA to $Ca_3(PO_4)_2$ can occur [102, 103].

HA prepared by the hydrothermal methods have high crystallinity and phase purity. Different crystal morphologies can be prepared (whiskers [104], plate like crystals [98]...). Reactants used are the same as in the case of solid state synthesis [105].

The precipitations methods are very common for HA preparation. The reaction environment is kept basic and temperature can range from 20 to 100 °C under normal atmospheric pressure [100, 101, 105].

Since some heat treatment is the essential step during ceramic processing temperature stability of HA is crucial. The beginning of sintering process, a neck formation, is observed around 900°C under atmospheric pressure in the air atmosphere. Standard sintering temperatures for HA range from 1100°C to 1400°C. The conventional sintering of HA is usually applied, but the spark plasma sintering, or the microwave sintering is possible as well. Being sintered above 1350°C the conventional sintering of pure HA can lead to a thermal decomposition [102, 103, 106]. HA decomposes to oxyhydroxyapatite and further to calcium phosphates [102, 103]. The end products of thermal decomposition are calcium oxide and phosphorous oxide [102, 106]. Temperature stability of HA is affected mainly by a partial pressure of water vapors in the sintering atmosphere [102] and a purity of initial powders [107]. A possible thermal decomposition of HA must be taken in account during heat treatment. The parameter of high importance is the chemical composition because some dopants can affect thermal stability of HA significantly. Addition of silicon [108] or calcium pyrophosphate [108, 109] can result in decomposition of HA phase during sintering and final phase structure is usually multiphasic.

Tricalcium Phosphate

Tricalcium phosphate $Ca_3(PO_4)_2$ abb. TCP, Ca/P=1.5, is a stable polymorphic phase in binary diagram of CaO – P_2O_5 (Figure 6 [110]).

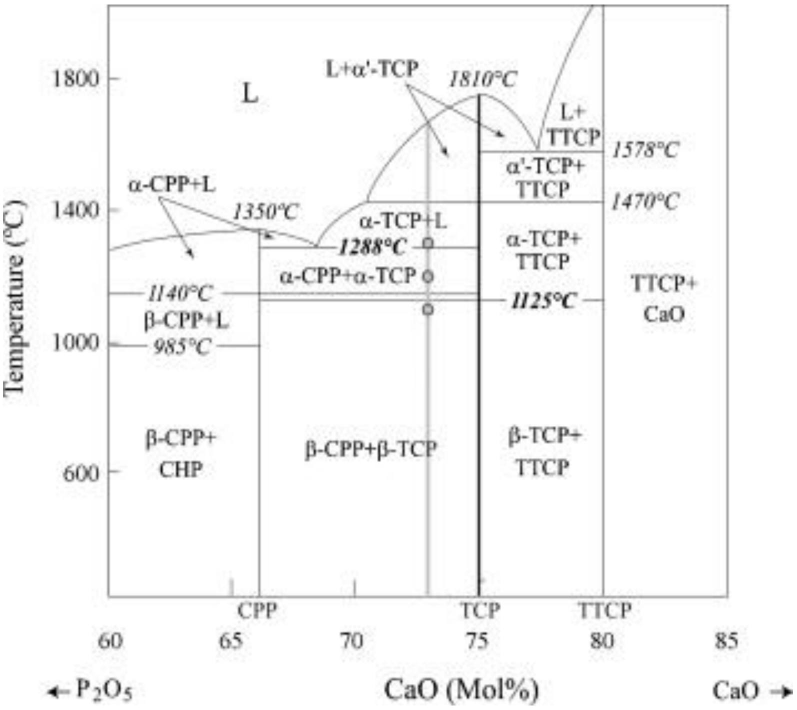

Figure 6 CaO – P_2O_5 phase diagram

There are three polymorphs of TCP called alpha (α), high temperature alpha (α´) and beta (β) [3, 105]. Sometimes, noncrystalline amorphous TCP is listed [105, 111]. Both α and α´ are high temperature polymorphs [112]. Since polymorph α´ cannot be stabilized at room temperature, this phase has no importance for the bone tissue engineering [112]. Polymorph β is stable at room temperature and it is a material which is often used for biomedical applications [18, 110, 113-115]. Polymorph α has monoclinic crystal lattice and is stable over 1125 °C to 1450 °C where undergoes transformation to α´ [112, 113]. Polymorph β is stable from room temperature to 1125°C where the transformation to α occurs [112, 113]. Phase α can be stabilized to room temperature by rapid cooling [112] or by thermal decomposition of HA phase [102, 108, 109]. Phase α has a lower stability under acidic conditions than β modification [15]. Phase α can be hydrolysed and reprecipitated in the form of nonstoichiometric calcium deficient HA (CDHA) [15]. This process creates needle-like structures characteristic with their self-interlocking mechanism [15, 17]. The self-interlocking mechanism can be used as a hardening mechanism and therefore α phase is essential part of apatite bone cements being responsible for self-hardening (setting) [15]. Ceramic scaffolds consisting of β-TCP are usually sintered at high temperatures to obtain solid ceramic body [110, 112]. There are some drawbacks related to alpha to beta transformation during sintering, mainly related to a volume expansion. The volume expansion during sintering may produce cracks decreasing the mechanical strength of porous TCP scaffolds [17, 110, 116]. TCP cannot be precipitated from water solution [105]. The most common preparation method is a high temperature synthesis of TCP by reaction of salts with Ca/P = 1.5 [117, 118]. If stoichiometry is not fulfilled, there is certain amount of calcium pyrophosphate ($Ca_2P_2O_7$) in final powder product [110]. Crystal lattice of TCP can be substituted at Ca^{2+} sites by variety of elements [119-121]. The substitution of the crystal lattice affects mainly temperature stability of β-TCP [121] and biological response of the material [113, 119, 120]. The substitution usually deteriorate mechanical characteristics of sintered TCP samples [119, 120].

Multiphasic Calcium Phosphates

Multiphasic calcium phosphates are typically composed of a mixture of α, β-TCP and HA phase [14]. Biphasic mixtures consisting of β-TCP + HA [109, 122], β-TCP + α-TCP [9, 117, 123], α-TCP + HA [124], β-TCP + $Ca_2P_2O_7$ [123, 125] or triphasic mixtures consisting of β-TCP + α-TCP + HA [126, 127] are commonly known. Theoretically, other mixtures of calcium phosphate salts can be prepared but they usually form HA and α, β - TCP during sintering [128]. Phase structure of the sintered multiphasic calcium phosphates is mixed on a grain level [14]. Overall phase composition can be estimated by XRD analysis [9, 109, 117, 122-125, 127, 129, 130]. Studies focusing on a distribution of the phases at a grain level are quite rare and little attention has been paid to this topic so far [109, 129]. The main problem is a very similar chemical composition of calcium phosphate phases [14]. Therefore, they are undistinguishable by standard spectroscopic methods (EDX, WDS methods). Phases can be distinguished by diffraction pattern [109, 131]. Methods based on diffraction phenomena must be utilized to describe distribution of the phases in a sintered body. Some work has been done utilizing a diffraction in a transmission electron microscope (TEM)[131]. Larger areas can be described by electron backscatter diffraction (EBSD)[109, 132]. At least basic knowledge of the phase distribution in calcium phosphates can bring better insight and understanding to the behavior of calcium phosphate scaffolds *in-vivo*. Due to different stability of different phases under in-vivo conditions, multiphasic compositions are believed to posses the key for controlled degradation of scaffolds [17]. Multiphasic calcium phosphates can be prepared by sintering of non-stoichiometric hydroxyapatite [122] or by thermal decomposition of amorphous calcium phosphates [133]. Sintering of Si doped HA results in a mixture of HA and α-TCP [124], the amount of α-TCP is dependent on the amount of Si doping. Multiphasic calcium phosphates can be prepared by the reaction of HA with $Ca_2P_2O_7$ [109, 124]. Reaction takes place approximately at 900°C resulting in a mixture of HA + TCP or pure TCP in a sintered body [124]. The reaction and associated phase changes can explain some discrepancy in a literature related to a shift of the phase composition after sintering [134, 135]. Multiphasic compositions can be prepared even by a direct mechanical mixing of different phases [17, 123].

2.2.2 *Solubility and Degradation of Calcium Phosphates*

What makes calcium phosphates attractive material for bone scaffolds is ability to be degraded and resorbed under physiological conditions [3, 12, 29]. Calcium phosphate scaffolds are almost exclusively used in a sintered form. The high temperature treatment does not leave any other possibility of a degradation but acidic dissolution of a structure mediated by osteoclasts [29]. Therefore, the stability of calcium phosphates in the acidic environment is of the high importance. Several models of dissolution for calcium phosphates has been proposed [136]. At pH 7 solubility of calcium phosphates is very low (Table 1). The lower the pH is the faster dissolution runs. Standard pH in the sealing zone of an osteoclast was found out to be between 3-5 [25]. If we compare solubilities of the most extensively used calcium phosphates the lowest solubility has HA, followed by β-TCP and α-TCP (Figure 7) [137]. These differences enable to design a rate of degradation of multiphasic scaffolds by their phase composition and their phase distribution [109]. The more HA in a structure, the lower rate of degradation. Exceeding 75% HA osteoclasts are not able to resorb the sintered structure [78].

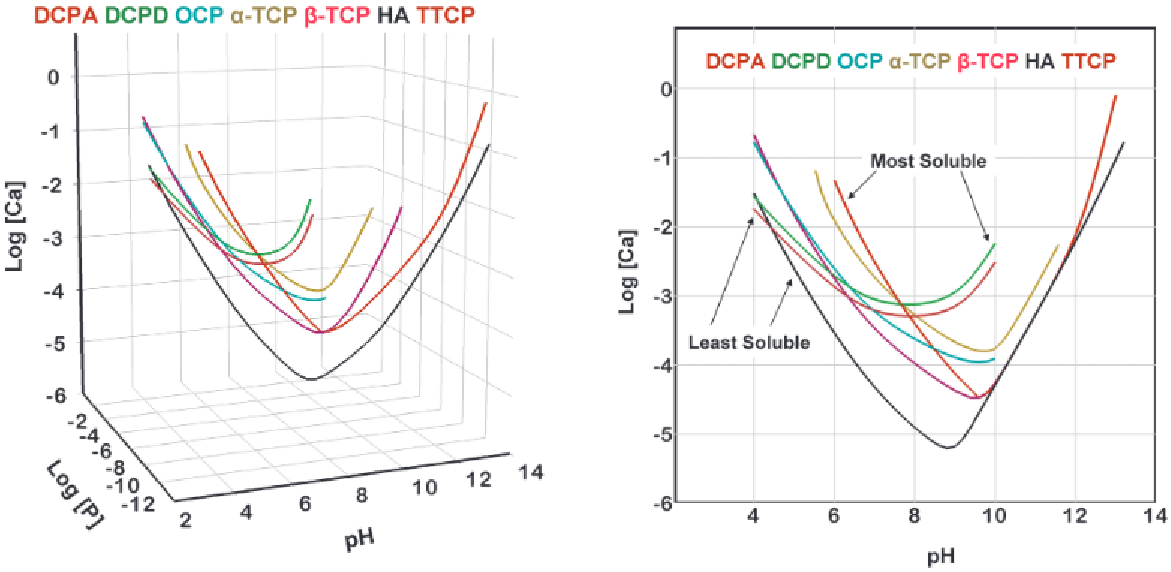

Figure 7 Solubility of different calcium phosphates as a function of pH

When calcium phosphate is implanted the material gets in contact with a harsh environment of a body. Many chemical and physical processes take place resulting in degradation and resorption of calcium phosphate materials [138]. Immediately after implantation dynamic equilibrium between material and implant is established by dissolution [136] and precipitation [17]. Ion exchange and structural rearrengement on the ceramic surface is done[138, 139]. Chemotaxis, attachment of the cells and their spread come afterward [78, 138]. The attached cells start to proliferate, and a healing process is launched. Basically, there are two different approaches how living organisms can resorb implanted material [29]. Being broken mechanically to the fragments smaller than 100 μm, these can be engulfed by macrophages. If the parts undergoing resorption are bigger than 100 μm, extracellular degradation must take place. Hence, extracellular degradation is mechanism for the resorption of sintered scaffolds. Osteoclasts attached to the surface create sealing zone [2, 25, 28]. The creation of sealing zone is dependent on an availability of the integrin binding sites [25, 32, 41, 59, 60]. Chemotaxis of the proteins with available binding sites from surrounding tissue or an artificial incorporation of these proteins into scaffolds before implantation is crucial. When osteoclasts are attached on the surface of the scaffold, they can dissolve calcium phosphate material by acidic leaching.

2.2.3 Mechanical Properties of Calcium Phosphates

Mechanical characteristics of calcium phosphates are generally poor. Bending or compressive strength of dense sintered HA ceramics is around 40-250 MPa and 120- 900 MPa, respectively [140]. In case of porous samples, the compressive strength is generally reduced to 1-5 MPa [10, 85, 140]. Fracture toughness usually does not exceed 1 MPa.m$^{1/2}$ [140]. Bending strength of compact (cortical) human bone is 160 MPa along the long axis of a bone [140]. Fracture toughness of a compact human bone is between 2-12 MPa.m$^{1/2}$ [140]. Since sintered calcium phosphates are ceramic materials, they behave as a brittle material under normal conditions. Mechanical characteristics of calcium phosphates scaffolds are further deteriorated by their porous structure, which is necessary for osteoconduction and related healing processes [11, 74]. Moreover, cracking during sintering caused by phase transformation of TCP affects mechanical properties [116]. Scientific reports have shown direct correlation between mechanical strength of TCP material and sintering temperature. The deterioration of mechanical properties of TCP materials sintered at a temperature higher than alpha to beta transformation temperature have been reported (Figure 8)[116].

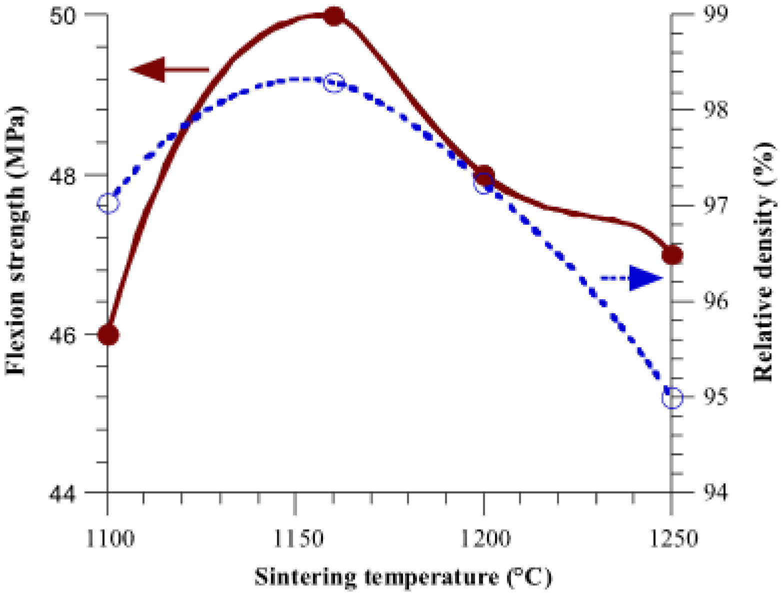

Figure 8 Mechanical properties of sintered TCP samples as a function of sintering temperature

Several attempts trying to improve mechanical properties of calcium phosphates has been made. They were focused on incorporation of secondary phases as zirconia [89] or alumina [141, 142]. These composites can improve mechanical properties. Unfortunately, both zirconia and alumina are not resorbable and stay inbuilt in a bone structure forever. Zirconia even reacts with HA and strengthening effect is often lost during sintering [143]. Moreover, incorporation of nonresorbable material within a new bone matrix is not desired. Therefore, calcium phosphates are supposed to be just short term replacements utilized for no or light load-bearing applications [3]. Being designed as bioresorbable, the porous calcium phosphates change their behavior during healing [17]. The ideal speed of a bone healing should match implant degradation compensating the loss of the mechanical strength of the scaffold by the development of a new bone tissue[17, 144-146]. To sum it up there are two antagonistic demands (mechanical strength and resorbability). Because of these antagonistic demands, bioresorbable implant must be designed as compromise between the mechanical performance and the biodegradation performance. Mechanical strength of the scaffolds must be high enough to withstand handling and implantation procedures. Once the implant is fixed in a position, loading of the implant is kept at the lowest level. But even normal loading of bones does not often exceed 4 MPa [140] which is not a value beyond the realms of possibility for CaP materials. The biodegradation rate is often balanced using multiphasic compositions of porous implants [14]. The ratio between the most stable calcium phosphate phase (HA) and less stable calcium phosphate phases (TCPs) governs the biodegradation process [14]. The distribution of phases in the volume of sintered materials is of high importance, governing an evolution of the implant interior and evolution of mechanical strength [109].

2.2.4 Internal Structure of Scaffolds

The internal structure of scaffolds is an important parameter for an ingrowth and proliferation of the cells. According to the manufacture process there are two general routes – precisely defined internal microstructure achieved by methods of an additive manufacturing and more or less stochastic approach using pore forming agents and template methods. Influence of the different pore shapes on biological responses has been tested (Figure 9) [147]. It was shown, no matter what the initial pore shape was, growing cells always reduced a shape of the pore to the circular. Starting from the corners and continuing along the surface, the cellular web was always denser in the starting point. No significant differences were found in the total amount of tissue produced as a function of pore shape. This means that the mean layer thickness was similar in a different geometries despite the local variation in tissue distribution within the pores [147]. It seems that curvature is variable driving tissue growth [147, 148]. If put on flat surface, cells do not have a tendency to form new layers unless

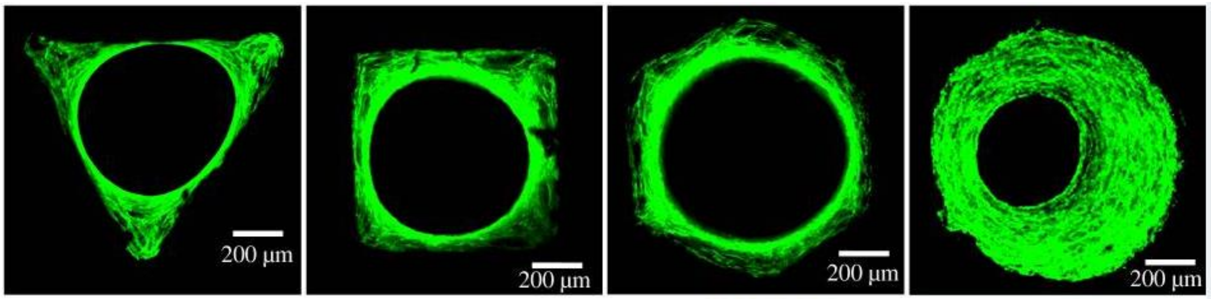

Figure 9 Tissue growth in differently shaped pores

surrounding become curved by the tissue growing from the corners [148]. Curved shape of inner structure of trabecular bone is the key to the mechanical performance [149]. It is known, that mechanical stress can trigger the assembly of filamentous stress fibres [150, 151]. It means that in the physical systems containing interfaces for which surface tension is important tissue evolves in such way that the local motion of the interface is controlled by the local curvature [147]. Moreover, keeping the curvature constant, the rate of the growth inside this structure would be the more or less the same at every time point [147, 150]. It can be derived from these results that the three-dimensional structure enabling constant ingrowth rate of the tissue is structure composed of spherical pores.

Not only the shape of pores, but even their size matters. It has been reported that there is a strong correlation between a pore diameter and *in-vivo* performance [152-157]. Pores on the boundary between implant and bone tissue provide mechanical stability and anchor the implant by bone ingrowth [138, 158]. Porosity of the implant determines whether new bone will have evolve through its structure [155, 156, 159, 160]. Speaking about pore size in case of scaffolds for bone tissue engineering, they are divided into micropores (smaller than 5 µm) and macroporous (bigger than 100 µm) [74, 161]. Pores between 5 µm and 100 µm are sometimes called mesopores. Microporosity can significantly enlarged surface area of scaffolds, enabling better adsorption of specific proteins and allows easier cell attachment [74, 162]. Although, some research has shown that there is no correlation between microporosity and osseointegration and osteoconductivity [163]. Microporosity of the sintered scaffolds is influenced mainly by sintering regime [110, 164]. The higher the sintering temperature is, the lower the microporosity is. Unfortunately, high microporosity usually means worse mechanical performance [10, 116]. The minimum recommended pore (macropore) size is 100 µm [74, 161]. Optimal size is believed to be bigger than 300 µm [74, 161]. Pores smaller than 100 µm do not allow early vascularization of tissue formed in the pores. As a result, the unmineralized fibrous tissue develops [157, 165]. Pores larger than 300 µm favour direct osteogenesis since blood vessels can freely penetrate porous structure and the level of the oxygen is stable [166]. Smaller macropores (100 µm) favour osteochondral ossification [74]. The pore size itself is not enough. Open porosity is the second crucial parameter of an internal structure of the scaffolds. The higher the porosity is the better permeability of the structure is observed. Moreover, there is less material which needs to be resorbed during healing process. High porosity (more than 80 %) and an interconnectivity allow penetration of the scaffold by essential factors and bone cells, allowing cell proliferation, formulation of vascular system and development of new bone [115, 153, 161, 167, 168]. Simultaneously higher porosity and micropores enlarge specific surface area and scaffold can be then considered as a catalysator for biological processes. Interconnections between pores must be large enough to allow deep penetration of blood vessles and bone cells to the volume of the scaffolds [165]. The size of interconnection should be at least 50 – 100 µm [74, 161].

2.2.5 Improvement of Biological Properties

Concept of pure calcium phosphate scaffold is overcome, and research is now focused on osteoinductive scaffolds where the osteinduction is reached by incorporating different polymeric substances, grown factors, proteins and even living cells. In this chapter the most promising materials which can be combined with calcium phosphates will be revised.

Collagen

Collagen is a structural protein found in the majority of soft and hard tissues. Collagen creates approximately 30 % of a protein mass in a human body [169]. Collagen do not possess great danger of antigenicity and immunogenicity [170]. Poor immunogenic properties of collagen has been researched and it has been shown, that major antigenic determinants in the collagen were located in a non-helical region [171]. Having been removed, collagen material was free of immunogenic properties. The same result can be obtained by cross-linking which even improve mechanical properties of pure collagen scaffolds [170]. There are 28 different types of collagen recognized so far [169]. The most abundant is collagen I, II and III. These collagens are created by three polypeptide chains knitted together in the form of triple helix [169, 170]. Collagen is bioresorbable material, which can be break down by enzyme collagenase [172]. The resorption rate is attenuated by cross-linking. Pure collagen has very limited mechanical properties. Collagen structures are often loaded with factors and cells serving as a carrier material [173, 174]. In the case of bone repairs, collagen is beneficially delivered mixed with calcium phosphate powders [175, 176] or as a filling of porous calcium phosphate scaffolds [177, 178].

Oxidized Cellulose

Oxidized cellulose (6-carboxycellulose) is an antibacterial, antivirotic, biodegradable and non-toxic material used for a wound healing [179] and as a hemostatic material [180-182]. Oxidized cellulose is usually prepared by leaching of the cellulose in a mixture of acids (N_2O_3, HNO_3, H_3PO_4, H_2SO_4) [183, 184]. Oxidation of cellulose induces conversion of glucose residues to glucuronic acid residues containing –COOH groups which makes this material quite acidic in a water environment [185]. Therefore, oxidized cellulose is often functionalized with arginine with basic side chain [186] or chitosan [187]. Oxidize cellulose is a great carrier for drugs and factors delivery [188].

Calcium Polyphosphate

Inorganic polymeric phosphate is a physiological polymer accumulated in bone cells [189]. Osteoblastic like cells can cleave the chain and use energy and material for bone mineralization process. It has been shown that a presence of calcium polyphosphate can increase the level of alkaline phosphatase enzyme and upregulate the levels of bone morphogenic protein 2 and osteoprotegerin indicating upregulation of an osteoblastic activity [189, 190]. It has been reported on osteosarcoma cells *in-vitro* that combination of HA and calcium polyphosphate can induce upregulation of gene coding formation of collagen I and alkaline phosphatase (ALP). These results suggest improving the osteoinductivity of the surface treated by calcium polyphosphate. The treatment of dental hypersensitivity can be mentioned as an example of practical use of polyphosphate [191].

Polydopamine

Polydopamine is a material well known for its versatile coating properties on majority of surfaces including non-wetting surfaces as polytetrafluoroethylen [192]. Polydopamine is final oxidation product of dopamine[193], which is both hormone and neurotransmitter[194]. Surface can be functionalized by polydopamine by a simple dip-coating method [195, 196]. Dip-coated polydopamine samples induce faster cell spreading on non-wetting surfaces [192]. Polydopamine-treated surfaces can immobilize different factors including bone morphogenetic proteins [197, 198]. Polydopamine has a great affinity to both calcium phosphate [199, 200] and collagen [196, 199, 201] therefore calcium phosphate surface treated with polydopamine can serve as a bond coat for collagen coatings and for drug delivery applications [199]. Moreover, polydopamine has been proven to have an anti-inflammatory effect, which can help in the first days after scaffold implantations [202].

Fibroblast Growth Factors

There are 22 members in the fibroblast growth factor (FGF) family. FGF factors are associated with various biological functions including skeletal formation. FGF2, FGF9, and FGF18 are regarded as possible candidates useful for bone regeneration [203, 204]. FGF alone do not induce osteoblast differentiation but it modulates osteoblast differentiation. The most common ligand in regenerative medicine is FGF2. The essentiality of FGF2 has been shown on FGF2-deleted mice [205]. Missing FGF2 resulted in the decrease of the bone mass and bone marrow stromal cells demonstrated lower will for osteoblast differentiation. FGF2 is frequently utilized as the bone promoting factor in a bone tissue engineering speeding bone growth. Beneficial effect of FGF2 has been proven for both critical and non-critical bone defects in a wide dosage range starting from 10 ng/ml [206] to 5 μg/ml [207] using collagen as a carrier in the rat in-vivo model and from 200 μg/ml to 800 μg/ml using gelatine hydrogen as a carrier in the human model [208]. Nevertheless, it has been shown, that high dosage of FGF-2 in the mice model has rather negative affect on bone formation and excessive dosage of FGF-2 can cause inhibition of the osteogenesis [206].

Bone Morphogenic Proteins

Bone morphogenetic proteins (BMPs) belong to a group of growth and differentiation factors called transformation growth factors (TGFs) [209]. There are more than 20 different types of BMPs. The most commonly known factor BMP-2 is osteoinductive [209]. Being used properly BMP-2 has a potential to improve a bone healing and shorten recovery times. Open tibial fractures treated with the help of BMP-2 (1.5 mg/ml, total dose 12 mg) decreased the risk of failure of the treated site and the necessity for invasive interventions compared with a control sample [210]. In the case of a spinal fusion 100 % fusion rate has been reported without any worsening of related neurological symptoms and 75 % of patients reported improvement in the terms of pain from affected site [211]. It has been assumed that high dosage (more than 40 mg/ml) of BMP-2 could potentially increase the risk of cancer mainly if BMP-2 is used off-labeled. Extensive researches have not confirmed the correlation of cancer incidence and use of BMP-2 [212, 213] and further research in this area is needed.

2.2.6 Biomedical Applications of Calcium Orthophosphate - Based Bone Grafts

Calcium orthophosphate ceramic materials are nowadays widespread in the many medical applications. Hydroxyapatite and beta tricalcium phosphate bone artificial grafts are utilized in an abundance in alveolar ridge augmentations, tooth replacements, maxillofacial reconstructions, spine fusions and repairs of bone defects [3, 14]. Artificial replacements can be delivered to the wound site in the form of pastes, granules and blocks, often combined with biodegradable polymers or factors. A variety of different products are approved for a surgical use. The overview of commercially available products can give us a hint of current trends in the bone healing and even show us the direction for an improvement.

Hydroxyapatites products are supplied, among the others, by Baxter company (US), Lasak (CZ), Olympus Terumo Biomaterials (JPN), and Corebone (ISR). Baxter product Altopore^{TM} cosists of granules 1-2 mm large with open porosity 80 – 85 %. Material of the granules is silicon substituted HA with 0.8 % silicon by weight. HA granules are dispersed in resorbable aqueous gel carrier. Putty can be mixed with bone marrow aspirate to improve biological performance and is approved to be used as a standalone graft or autografat extender. Altapore is non-loadbearing and resorbable material. Altopore^{TM} material has been clinically-tested and Si-doped HA has appeared to provide stable osteoconductive scaffolds, which supported faster angiogenesis and bone apposition [214]. The same material (Si-HA) are supplied in the form of granules or blocks under the trademark Actifuse. It has been shown that the Si doped-HA in the form of Actifuse has similar behavior as grafts treated with BMP-2 [215]. Lasak provides material called OssaBase-HA^{TM} which is synthetic carbonated HA in the form of granules used for a bone regeneration independently or in a combination with the autologous bone grafts, blood, or platelet rich plasma. Granules are 0.3-2 mm in size with macropores bigger than 100 μm. This material has low substitution rate and is recommended for periodontology, orthopedics, and neurosurgery. Material has been tested and it was reported that the performance of OssaBase is comparable with deproteinized bovine bone xenograft [216]. Olympus Terumo Biomaterials produce HA material under the brand name Boneceram P^{TM}. This material is a pure stoichiometric hydroxyapatite with a porous structure. The porosity differs between 35 – 48 % with a pore size 50 – 300 μm. The material is available in the form of blocks, cylinders, granules, and spacers. Company also provide material under the brand name Boneceram K^{TM} which is the same in the terms of chemical composition but has a dense and a porous layer. Boneceram (P, K) is claimed to be unresorbable material [217], which is common problem of pure HA materials especially with low porosity. Corebone is a company focusing on coralline HA. Corebone produce Corebone^{TM} material by conversion of marine corals to the HA-like material. Being grown in a closed aquatic system changes in chemical composition of the material caused by water pollution is avoided. The final material is produced in the form of granules or porous block. Porosity and pore size are not stated. No references using Corebone has been found.

Tricalcium phosphate products are supplied by Ceraver (F), Ceramed (PT) and Synthograft (USA). Ceraver supplies product called Calciresorb^{TM} which is β-TCP material in the form of blocks and granules. Calciresorb^{TM} is claimed to be fully resorbable. The structure of the material is interconnected macroporous structure. The resorbability is claimed to be finished from 6 to 24 months. Nevertheless, there are reports suggesting that calciresorb is not pure TCP material but biphasic mixture of HA and TCP (25/75) [218]. In vivo tests have suggested that this material promotes osteoblastic differentiation and in vivo bone formation [218]. Ceramed supplies material called Trioss^{TM}. This material is manufactured in the form of blocks, wedges, cylinders and granules. Total porosity of the material is 60 – 80 % with the pore size between 200 – 500 µm. Material has very low compressive strength of 0.2 MPa. Manufacurer claims that the material is resorbed up to 6 months after implantation. Synthograft company produce β-TCP granules under Synthograft trademark. Being claimed as resorbable the material should disappear after 3 months. Even in the case of Synthograft^{TM} has been shown that the phase composition is not pure β-TCP but rather mixture of β-TCP and 9 % of β-$Ca_2P_2O_7$ [219]. Nevertheless, human histology showed that this grafting material is suitable for bone regeneration in maxillofacial complex and new bone formed was detected within 3 months after implantation [219, 220].

Since a positive synergic effect of multiphasic calcium phosphate is known the private companies offer multiphasic calcium phosphate materials for bone regenerations as well. Among these companies are Straumann (CH), Exactech (USA), Teknimed (F), Biotechone (TW) and Ceramisys (UK). Straumann supply a bone grafting material called BoneCeramic^{TM} and Maxresorb. Composition of granules or blocks is 60 % HA and 40 % β-TCP with 80 % of the porosity and a pore size between 200 – 800 µm. Manufacturer claims a full resorbability of the material and the material is recommended for implantology, periodontology and oral surgery. It has been tested *in-vivo* on a rat model for treatment of 5 mm calvarial defect [221]. The BoneCeramic^{TM} had an osteoconductive potential but lower than autologous bone graft. It was concluded that slower resorption rate had been caused by 60 % HA in the composition of BoneCeramic^{TM}. This conclusion is in good agreement with work where 100 % β-TCP was used for the same type of the calvarial defect [222]. In this work pure β-TCP performed even better than autologous bone graft or β-TCP loaded with BMP-2 (Figure 10). Exatech company produce material called OpteMx^{TM} which is a porous mixture of HA and β-TCP (60/40) with open porosity reaching 60 -80 %. The composition is the same as in the case of BoneCeramic^{TM} and Maxresorb^{TM}. Pore size is between 300 – 600 µm. Material is produced in the form of granules and shaped blocks. In the case of porous blocks larger than 5 mm, it has been shown

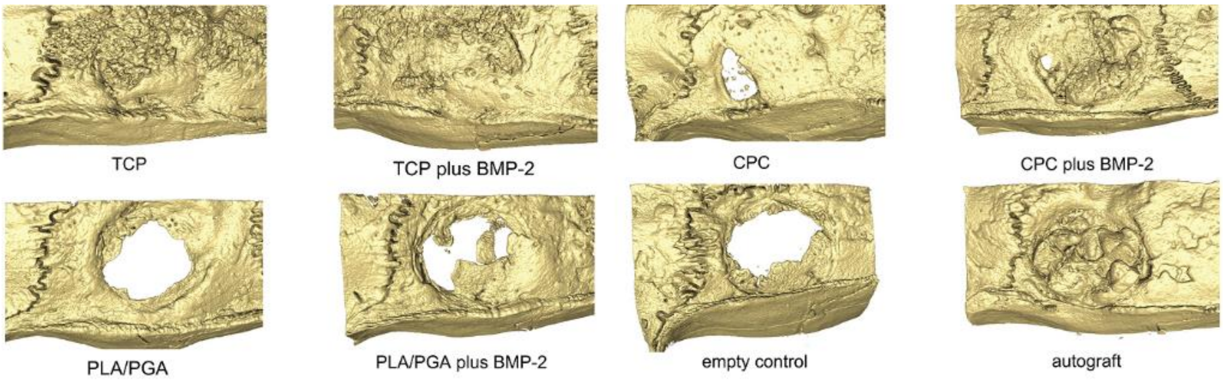
TCP
TCP plus BMP-2
CPC
CPC plus BMP-2
PLA/PGA
PLA/PGA plus BMP-2
empty control
autograft

Figure 10 Rat calvarial defect treated with different types of grafts, CT scan after 45 days postoperative. CPC – calcium phosphate cement, PLA/PGA - polylactic and polyglycolic acid gel

that the maximal penetration depth of newly formed bone was 2.5 mm per year [223]. Resorption after on year reached 44 % of the weight of initial material. Teknimed company produce a material called Ceraform® which is a mixture of HA and β-TCP (65/35). Material is claimed to be osteoconductive and resorbable. The material is supplied in the form of granules and porous blocks. The material has been used for spinal fusions, as a filler for bone tumours cavities, non-unions and fractures [224]. The results have suggested that for limited bone loss the Ceraform® is good alternative to allografts. BiotechOne company produce material called BonaGraft™ in the form of porous HA/ β-TCP granules (60/40), claiming that material is suitable for void filling applications in the bone. Ceramisys produce material called ReproBone® in the form of granules and blocks. The material has 80 % porosity and an interconnected pore structure. The phase composition is claimed to be HA and β-TCP mixture (60/40). Material has been used in the *in-vivo* study on a mice model where good biocompatibility and osteoconductivity has been confirmed mainly if the material was combined with BMP factors [225].

Researches conducted on commercial materials suggest the same trend as researches conducted on the laboratory materials [226]. A high HA content makes implant unresorbable with worse osteoconductive properties. Biphasic calcium phosphates seem to be the most promising materials for further development in the field of porous ceramic bone substitutes. It is worth to mention, that HA/TCP ratio in commercially available products is HA/TCP = 60/40 or at least very close to this ratio. More biomedical applications of calcium phosphates can be found elsewhere [14, 78].

2.2.7 Manufacturing Methods and Customization

Customized scaffolds can be produced by two basic approaches. The older approach is a gradual removal of material by the milling, drilling, or cutting. New approach is free-form fabrication, where the final part is printed layer by layer.

Considering the first approach, we need a block of porous material which can be machined to a desired shape. In the case of the calcium phosphate materials it means to machine a ceramic material. Ceramic materials are known for a high hardness and brittleness. It is almost impossible or hardly possible to machine sintered ceramic materials by conventional methods. Therefore, machining of ceramic materials is almost exclusively done in green or presintered states, when ceramic material does not posses its full brittleness and hardness [227, 228]. Porous green ceramic blocks with sufficient strength to withstand handling and machining can be produced by templates methods or direct foaming methods [10, 85].Templates and direct foaming methods utilize ceramic suspension as a raw material [229]. Ceramic suspensions must have quite high solid loadings and be stable in a sense of a sedimentation and a clustering. Stability of the suspensions is achieved by dispersants bringing repulsive forces to the system overcoming attractive forces between dispersed particles [230]. If the particles are in the range of hundredths of nanometres the sedimentation does take place but very slowly or does not take place at all, mostly if the system is stirred. The basic idea of templates methods is to incorporate suitable template in the form of polymeric foams, natural templates, or particles in the volume of the suspensions. After consolidation of ceramic suspensions these templates are burn out resulting in porous structure [229]. Problems of these systems are associated with cracks development during polymer burn-out, when the gas created by thermal decomposition of a template must diffuse through the ceramic walls [231]. Direct foaming methods are based on incorporation of gas bubbles into the suspensions and their subsequent consolidation [229]. The main difference between these two approaches is the final structure which is in the case of template methods more or less an exact replica of the template. In the case of direct foaming methods the final structure is a randomly distributed porous structure with circular pores [10, 85]. The direct foaming methods are highly efficient and the final structure is defined by circular pores, which are crucial for even formation of a new tissue [147]. The consolidation of suspensions is normally provided by curing of dispersed monomers after foaming and the kinetics of curing determines the final structure [10]. If the curing is too slow than Oswald ripening takes place and the foamy structure degrades [229]. Therefore, balance between the curing and the foam ripening is crucial. Ceramic blocks can be used for machining [232, 233]. The CAD/CAM custom made implants can be produced and used even for an extensive cranioplasty. Results has shown low adverse reaction and low morbidity rate with high aesthetic and functional results [234]. It is worth to stress that the dimensions of part machined in a green or a presintered state must be enlarged because of the shrinkage occurring during final sintering of the product [10, 228].

As a counter pole for a machining approach stays the free-form fabrication techniques. These techniques involve stereolihtography, extrusion, selective laser melting and many others [235]. The main advantage is that the final structure and the shape of the part is restricted, theoretically, only by our imagination. The main disadvantages are the technical demands on equipment and usually a lower production efficiency. Even though free-form fabrication methods are challenging they evolve rapidly becoming a good method for production of customized parts [236]. Unfortunately, printing of structures similar to the structures prepared by template or direct foaming methods is highly demanding and therefore additive manufacturing cannot compete with these methods so far.

The challenging part of the implantation of ceramic scaffolds is their emplacement at a wounded site during surgery. The stability of implants is crucial for healing and a new bone development. Micromovements of implants can cause fatal failure of implants or healing process itself. The bright idea, improving a progress during the surgery, is 3D printing of the model of a wounded site. In this case surgeons can test a strategy of implantation and a method of implant stabilization beforehand. There are several possibilities how to fix a position of an implant. The most common is its fixation by titanium screws and plates [232, 233]. The main disadvantage of this approach lies on unresorbability of the hardware. After healing hardware must be either extracted or let be inside for the rest of a patient life. The other methods rely on fixation using resorbable sutures [234] or a fixation of the implants by bone cements [237].

3 Research Part

The research part describes preparation and multiscale evaluation of porous ceramic scaffolds. The main stress is put on ceramic technology, processing of the porous samples and their evaluation from the viewpoint of material sciences. To describe the materials completely, there are parts focusing on biological response of cell cultures to the materials as well. The multiscale evaluation enabled to choose the best material for scaffold preparation being subsequently used for *in-vivo* tests on animal model.

The research part is divided into five subchapters. Each subchapter deals with certain part of scaffolds manufacturing process, their characterisation and *in-vitro* and *in-vivo* testing. The subchapters were arranged in the logical order starting from development and processing of the materials, followed by *in-vitro* and finally *in-vivo* tests. There is a brief summary after each chapter helping to sum up the results and outcomes of every part and highlighting the main ideas important for following sections. The research part gives an entire picture about the doctoral research focused on calcium phosphate biomaterials.

3.1 Aims of Doctoral Research

The main goal of the doctoral research was an investigation of processing and properties of multiphasic, hybrid and customized calcium phosphate scaffolds for bone defects treatment. The main goal was achieved by fulfilling several tasks:

1. Preparation of porous bioceramic materials based on calcium phosphates
2. Description of porous structures of the sintered calcium phosphate foams
3. Implant customization by conventional milling
4. Mechanical characterization of the porous calcium phosphate materials in simulated *in-vivo* conditions
5. Description of calcium phosphates phase distribution in the multiphasic samples on a grain level and correlation of the phase distribution with their mechanical and biological properties
6. *In-vitro* evaluation of different types of porous calcium phosphate materials
7. *In-vivo* study of a spinal fusion on the animal model

3.2 Production of Machinable Calcium Phosphate Foams for Medical Applications

As it has already been discussed in the part 2.2.7 *Manufacturing Methods and Customization* conventional CAD/CAM milling is one of the possible approaches for implant customization. Since a milling is well-known and widespread industrial technology, we exploited CAD/CAM as a manufacturing method suitable for customization of porous calcium phosphate implants with a high potential to become the first-choice processing method for suchlike applications. The main goal of this part of the research was to explore easily utilizable method for a production of a large quantity of porous ceramic materials being further used as a feedstock material for the milling. Since the brittleness of sintered ceramic materials is well known issue, being even more pronounced in cellular structures, different types of heat treatment of ceramic blanks were tested, and their milling performance was described and evaluated. Eventually, the performance of 3D milling was demonstrated on a complex ceramic part as a proof 3D milling customization concept. The material was prepared by a novel epoxy-based gelcasting method derived from common gelcasting process which has been known since the first mention in 1985 [238]. The main objective of this part was to prepare porous calcium phosphate (hydroxyapatite) blocks with open porosity. Targeted median pore size was between 300 and 500 µm. Diameter of interconnections between individual pores wanted was around 150 µm with an overall open porosity reaching at least 75 % better 80 %. All parameters mentioned were designed to meet geometrical requirements being agreed in the literature as basic requirements for successful vascularization, osteogenesis, and new bone formation. Since the literature reports shows, that the spherical pore shape is very promising [147], simple direct foaming method, ensuring spherical shape of the pores, was used. Main advantage of the novel epoxy-based gelcasting process is an elimination of exfoliation phenomena occurring during the traditional gelcasting [239]. The traditional gelcasting relies on a radical curing reaction. This process can be prematurely terminated by oxygen presented in the atmosphere. Therefore, in the case of traditional gel-casting foaming and curing of the foam must be carried out under nitrogen atmosphere. This fact complicates the whole preparation of the ceramic foams. Hence, we tested system where curing was provided by the chemical reaction between epoxy groups and amine hardener. This ring-opening polymerization reaction is not influenced by the oxygen in the ambient atmosphere and, therefore, preparation process can be carried out under normal laboratory conditions. Due to environmental hazards the systems containing organic solvents were not considered and water-based system was investigated.

3.2.1 Scaffolds Preparation

Several epoxy compounds can be found in a literature as possible candidates for water-based epoxy gel-casting systems [239]. By trials we had found that at least 15 wt. % of monomers containing epoxy group had to be dispersed in water to ensure decent handling properties in the green state keeping internal cellular structure of the foam stable. Considering this fact, the epoxy resin ethylene glycol diglycydyl ether (EGDGE), which has been successfully used before for similar systems [239] was utilized. Moreover, relatively low viscosity of EGDGE in comparison with other substances described in [239] did not substantially increase viscosity of the system and allowed to use powders with a particle size in the range of hundreds of nanometres. Dipropylentriamine (DPTA) was used as a hardener stimulating the curing of EDGDE monomers in suspension. The reaction of the hardener and epoxy monomer is schematically represented in the Figure 11. The gel (polymer network) formed by this reaction consolidates green body and prevents the green body of any further shape degradation, bestowing handling strength to the green body and decent mechanical properties.

For the proof of 3D milling customization concept, we decided to prepare porous ceramic samples consisting of pure hydroxyapatite (HA) phase to avoid any difficulties connected with the other CaPs phases. Namely phase transformation and high temperature reaction which can lead to crack development and structure degradation in the case of TCP [110]. The flowchart of the scaffold manufacturing process is depicted in the scheme (Figure 12).

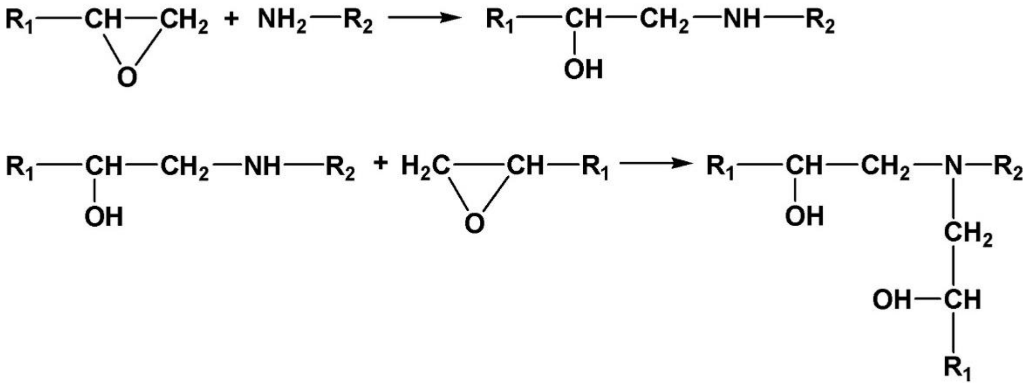

Figure 11 Scheme of curing reaction of an epoxy group with an amine hardener

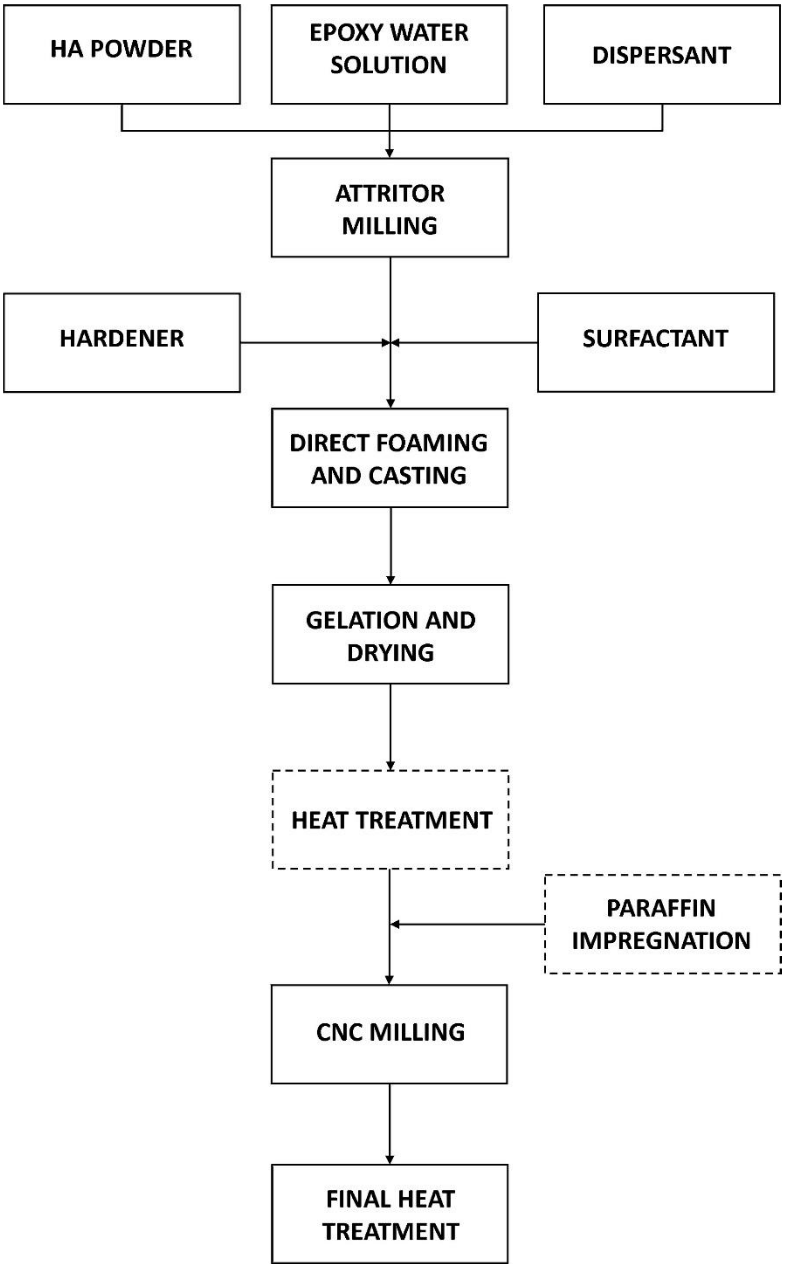

Figure 12 Flowchart of the scaffold preparation

Hydroxyapatite nanopowder (tri-calcium phosphate, extra pure, Riedel-de Haen, Seelze, Germany) was used. The HA powder was calcined at 1000°C for 3 hours before use. The calcination of HA powder decreased specific surface area from 66 $m^2.g^{-1}$ to 4.7 – 4.2 $m^2.g^{-1}$. The reduction of specific surface area was crucial for preparation of ceramic suspensions with relatively high solid loading (31.8 vol.%). The calcined hydroxyapatite powder was dispersed in the premix solution of deionized water (DI water) and epoxy resin ethylene glycol diglycidyl ether – EGDGE (Quetol 651, Electron Microscopy sciences, Hatfield, PA, USA). The overall epoxide-hardener content was 20 wt.% with respect to the liquid phase of the system. Overall volume solid loading used, based on previous experiments, was set on 31.8 vol. % or 58.5 wt.%, respectively. The exact composition of the hydroxyapatite suspensions is in Table

2. The ceramic particles in the suspensions were homogeneously dispersed and stabilized using commercial dispersant based on ammonium polyacrylate salt (Darvan 821A, R.T. Vanderbilt Co., Norwalk, CT, USA). Darvan 821A is 45 wt.% water solution of ammonium polyacrylate salt with average molecular weight of 3500 g/mol. Darvan 821A was chosen due to the fact that the chemical formula did not contain any elements which could serve as dopants of hydroxyapatite (Mg, Na, Si), leading to unwanted phase changes during sintering [240]. The optimum amount of the dispersant was found by steady shear rheological measurements at 1.2 wt.% of Darvan 821 A (calculated with respect to the powder).

Table 2 Composition of the hydroxyapatite suspensions

	HA powder	DI water	EGDGE	DPTA	Darvan 821 A	Triton X 100
Wt. %	58.5	31.0	6.0	1.8	0.3	2.4
Vol. %	31.8	53.3	8.9	3.3	0.5	2.2

The mixture of hydroxyapatite powder, dispersant and deionized water was milled in attritor (HD-01, Union Process, Akron, OH, USA) for 3 hours. Zirconia balls with a diameter of 1 mm were used as a milling medium. Milling speed was set to 500 rpm. The double-wall milling cylinder was used for milling, being cooled down during milling process by steady flow of the water, keeping the temperature of the suspension during milling under 20 °C. Milling cylinder was kept close during milling to minimize evaporation and a possible contamination of the suspensions. The median particle size in the suspensions after milling was measured by light scattering method and characterised with d_{50}=130 nm. After milling, zirconia balls were extracted. To ensure a foaming capacity, surfactant was added in that point (Triton X-100, Sigma-Aldrich, Saint Luis, MO, USA). The optimal amount of surfactant was 22.77 µl/g of suspension [85]. With surfactant added, suspensions were thoroughly mixed for 10 minutes to homogenize surfactant in the volume. Hardener (bis(3-aminodipropyl) amine, Sigma-Aldrich, Steinheim, Germany), also referred as DPTA, were dosed to the hydroxyapatite suspensions. Prior foaming, the hardener was added to the vigorously stirred suspension to ensure even distribution of the hardener in the volume. In order to exclude any effects and differences caused by different volume of the suspensions being foamed, the volume of the suspensions was 60 ml in all cases. The main reason is exothermal character of curing reaction, where a high volume could lead to an overheating and significantly change curing kinetics affecting the final microstructure. The foaming of the suspensions was carried out by a blender (Bamix Swiss Line, ESGE, Switzerland). Foaming time was set as a 3 minutes since previous test indicated that after 3 minutes no further increase in the foam volume had taken place [85]. Prior curing, the foamed suspensions were casted into cylindrical polypropylene moulds treated with paraffin oil. As soon as the foams were casted, polypropylene moulds were sealed to minimize drying during curing. Diameters of polypropylene moulds were 20 mm, 40 mm and 100 mm with height 30 mm, and 15 mm, respectively. The curing of casted foams took place at different temperatures ranging from 20 °C to 50 °C in order to optimize foam consolidation and corresponding internal microstructure of the samples. The cured samples were extracted from polypropylene moulds. Attention was paid to a stress-free extraction from the moulds where no compression or bending of cured samples occurred, because that could lead to damage of fine internal structure of the samples. The cured wet samples were dried under controlled temperature of 20 °C and relative humidity 98 % and 80 % in climatic chamber (Weiss, WK3-180/40, Germany) until water loss achieved at least 60 %. Reaching the water loss of 60 %, samples were taken out of climatic chamber and let dried under ambient laboratory conditions for at least 48 hrs before any further treatment. Samples with diameter of 40 mm were produced for milling tests. To describe the impact of a heat treatment on the precision of 3D milling, samples were divided into three groups according to their heat treatment regime – green state, presintered at 1150 °C/2 h, sintered at 1250 °C/2 h. All groups were prepared in a version impregnated with paraffin wax. The purpose of the impregnation was to fill the pores with material which would have shored up a thin and delicate internal structure of the ceramic foams and which would have secured an accurate machining without any damage. Moreover, the paraffin impregnation could help to attenuate vibrations during machining and, therefore, eliminate damages caused by the vibrations. The impregnation was carried out by a submerging the samples into molten paraffin wax (90°C for 15 minutes). The soaked samples were cooled down to a room temperature being constantly rotated. The rotation of the samples during cooling ensure an even distribution of the wax. The presintered and sintered samples for milling were prepared by heating to the 500°C at a rate of 50°C/h, followed by a heating to the presintering or sintering temperature at a rate of 120 °C/h with a dwell of two hours at the final temperature. The milling tests of porous samples were performed on a high-speed computer numerical controlled (CNC) milling machine with maximal rotation speed of 28 000 rpm (Ultrasonic, Sauer, Stipshausen, Germany) equipped with a diamond coated milling tool with a diameter of 1 mm. The finishing cutting speed was set to 2000 mm/min. The depth of cut and the width of cut were 0.13 mm and 0.08 mm, respectively. After the milling all samples, no matter what their previous heat treatment had been, were heat treated with the regime described above. The final sintering temperature was 1250 °C/2 h. Sintering at 1250°C for two hours preserved the single-phase hydroxyapatite structure of the samples.

3.2.2 Characterization of Structure and Mechanical Characterisation

Since the curing was crucial for final foam microstructure the curing process in the suspensions was monitored by small-strain oscillatory shear measurements performed on a rotational rheometer (HAKE MARS II, Thermo Scientific, Karlsruhe, Germany) equipped with sensors with parallel plate geometry. A diameter of the detector plates was 35 mm. The measurement set-up was covered with a solvent trap module to diminish drying effects during curing. To keep the environment in the measurement cell saturated with water vapours constant flow of moist nitrogen was secured and the closest vicinity of the measuring module was covered with a wet cloth. The size distribution of pores and pore windows was evaluated using microphotography taken by scanning electron microscope (SEM) (Verios 460L, Thermofisher Scientific, Czech Republic). The images were taken from randomly chosen fracture surfaces. In the SEM micrographs the largest dimension of the pores, which were expected to be spherical, and a pore windows, which were expected to be circular, were measured. No correction factor taking into the account the skewness of the projection was applied. The results were plotted as histograms of pore size and window size (diameter) on a frequency by volume or by an area, respectively. The number of bins was calculated according Sturge´s formula. Frequency by volume was calculated as the total mean volume of the measured pores in a bin divided by the total mean volume of all pores in all bins. The same calculation was applied for the evaluation of pore windows. Instead of mean volume, mean surface of the windows was calculated. These plots gave a better idea about internal structure of the scaffolds then mere plotting the size of the pores (windows) against number of incidences. The results obtained from SEM microphotographs were compared with results obtained from a computed tomography (CT) (phoenix v|tome|x L240, GE Sensing & Inspection Technologies, Huerth, Germany). The three dimensional CT scan was carried out with a voxel resolution of 20 µm. It means that the smallest distinguishable volume element scanned was 20 µm x 20 µm x 20 µm. The structural data scanned by CT were processed by an analysing software (VGStudio MAX 3.0, Volume Graphics, Heidelberg, Germany). The pores and pore windows were localized on a gradient parametric map on which the local extremes were searched and measured by watershed algorithm. The local extrema corresponds to the places being the air pores in original structure. The open porozity of sintered scaffolds was measured by the Archimedes method. The theoretical density of hydroxyapatite used for calculation had a value of 3.16 g.cm^{-3}. The compressive strength of green and sintered samples was measured using an universal testing machine (Instron 8862, Norwood, MA, USA). The compressive strength of the samples was measured on cylindrical samples with the height to diameter ratio equal to 1.5, corresponding to the sintered samples with a diameter of 14.5 mm and height of 22 mm [85]. Bases of the cylindrical samples were carefully grinded to be plan paralell. There was a thin leather pad inserted between sample and a cross-head during measurements to minimize an effect of uneven mechanical loading during test caused by local inhomogeneities of topography of bases. The crosshead speed of 0.5 mm.min^{-1} was applied and force deflection traces were recorded. The compressive strength of the sample was calculated as the first maximum on the loading curve before a rupture. Work of fracture was calculated as an integral area under a loading curve up to the fracture divided by a sample´s cross-section. The Weibull strength and the parameters of a Weibull strength distribution were calculated numerically according the EN 843-5 Standard.

3.2.3 Results and Discussion

The scheme of the epoxy – amine cross-linking curing reaction is shown in the Figure 11. This reaction occurs in the ceramic suspension by cleavage of epoxy rings located in the EGDGE molecule by the action of hardener molecule (DPTA). The active hydrogen in primary amine reacts with an epoxy group to form secondary amine. The secondary amine reacts with epoxy group. The resultant tertiary amine polymerizes epoxy groups. Aliphatic amine hardener (DPTA) allowed curing of the suspensions both at a room temperature and at elevated temperatures. The polymeric network created during this reaction consolidates ceramic foams and prevents their degradation during drying. As it has already been explained above, epoxy based gelcasting system allowed curing in the ambient atmosphere and no exfoliation phenomena related to the free-radical curing reaction of the traditional systems took place. However, in the water environment the epoxy ring can be cleaved under basic conditions. Unfortunately, the pH of the hydroxyapatite suspensions had to be kept at pH of 9 – 10 to ensure maximum stability of the colloidal system. According to the theory [241], hydrolysis of epoxy groups can cause the formation of alcohols, which are inactive and cannot contribute to the polymerization (Figure 13).

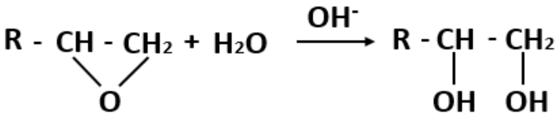

$$R - \underset{\diagdown O \diagup}{CH - CH_2} + H_2O \xrightarrow{OH^-} R - \underset{OH}{CH} - \underset{OH}{CH_2}$$

Figure 13 The hydrolysis of epoxy group in water

Because of partial hydrolysis of epoxy groups density of crosslinked polymer network after curing is lower. This lower density was indirectly observed by the small strain oscillatory measurements. The time dependence of the absolute value of complex viscosity, $|\eta^*|$, of the suspensions aged for different time is shown in the Figure 14. The experimental values measured were fitted with Hill equation, standardly used in the modeling of polymerization kinetics [242]. Hill equation is usually written as:

$$|\eta^*(t)| = |\eta^*(\infty)| \frac{t^n}{t^n + \theta^n} \tag{1}$$

Where $|\eta^*(\infty)|$ is the final absolute value of an equilibrium complex viscosity of the system, θ is the half – curing time and n is a coefficient relative to the asymptotic slope at the half-curing time θ. This model consists of the parameters which can be further used to determine the equilibrium viscosity of the cured polymeric system. Moreover, the total curing time defined as the time necessary to achieve 95 % of final viscosity can be derived from this equation as well. The parameters derived from this equation for the suspensions aged for different time are in the Table 3. The effect of an aging on a final curing behavior of the hydroxyapatite suspensions is obvious both from Figure 14 and Table 3. A viscosity drop related to the hydrolysis of epoxy groups was the most pronounced within the first 24 hours. During the first 24 hours steep drop of the equilibrium viscosity occurred. The equilibrium viscosity derived from eq. (1) reached 104.4 kPa.s for suspensions 2 hours old. The same suspensions aged for 24 hours reached equilibrium viscosity of 51. 3 kPa.s, which means 50.9 % decrease for the system. After initial 24 hours the rate of the final viscosity drop-off considerably ceased. The difference between 24 hours and 72 hours was just 5 kPa.s. It seemed, that equilibrium conditions were reached after 72 hrs of aging. In order to avoid the differences in the curing of the samples which could possibly lead to different mechanical and microstructural characteristics of final samples, these were prepared from the suspensions aged for 24 hrs.

Despite the degradation of epoxy groups in the suspensions it was still possible to reach final viscosities higher than in the case of the traditional polyacrylamide-based systems (51 kPa.s vs 44 kPa.s, respectively) [85].

Table 3 Curing parametres of the hydroxyapatite suspensions

Suspension HA X/Y *	Idle Time (s)	Total Gelation Time (s)	Final Viscosity (Pa.s)
HA 25/2	3150	18330	104440
HA 25/21	3050	12340	56570
HA 25/24	3200	11400	51330
HA 25/48	3490	12120	44690
HA 25/72	3490	17270	46270
HA 35/24	910	2180	56240
HA 50/24	230	-	-

*X Curing temperature (°C), Y aging time (h)

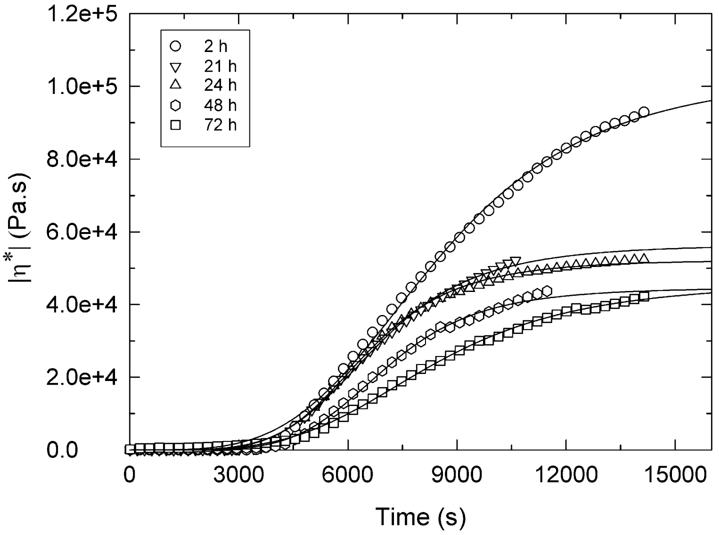

Figure 14 Time dependences of complex viscosity during gelation at a temperature of 25°C for hydroxyapatite suspensions aged for different times.

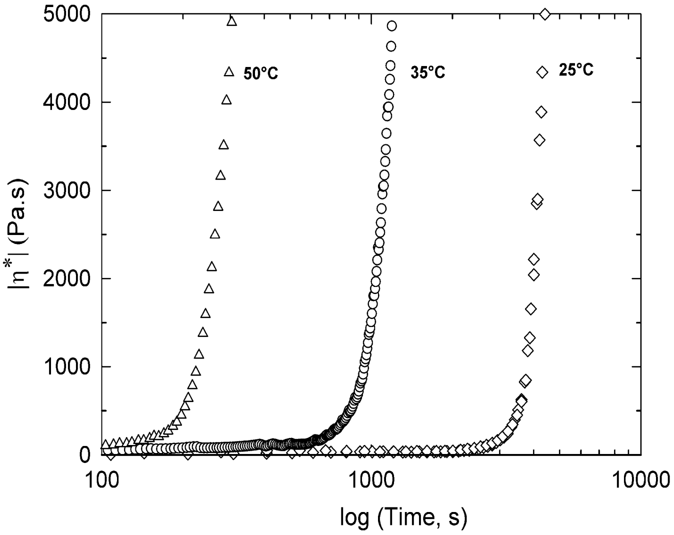

Figure 15 Time dependences of the complex viscosity for hydroxyapatite suspensions cured at different temperatures. The suspensions were aged for 24 hrs before measurements.

The kinetic of curing reactions of epoxy-based system is temperature dependent and a curing rate increases with an increasing temperature. The faster the curing is the lower degradation of initially prepared foam structure occurs. On the other hand, speeding up the reaction, the idle time (defined as time before any pronounced cross-linking in the suspensions occurs and the viscosity of the system starts to rise rapidly) is shorten. The idle time long enough is necessary for the successful foaming and foam-casting into the moulds. In the case of our epoxy-based system, the idle time was determined as a time point where tangent of the viscosity curve in logarithmic coordinates changed at the highest rate. The onset of the curing can be seen in the Figure 15. Heating the reaction environment for 25 °C (from 25 °C to 50 °C) caused shortening of the idle time for more than 14 times (from appr. 3300 s at 25 °C to 230 s at 50 °C). The idle time of 3300 s for suspension cured at 25°C was too long to preserve foamed structure in undegraded state. If suspension was cured at 50 °C the idle time (230 s) was to short for both foaming and casting. The optimal temperature from technological point of view seemed to be 30 °C. Unfortunately, there could be deviations in the results due to slight time and temperature differences during processing. Therefore, we proposed and investigated methods utilizing foaming and casting of the suspension at 25 °C with subsequent curing of the samples at elevated temperature of 35 °C or 50 °C. It turned up to be crucial for having both processing time long enough for foaming and casting step and quick curing of the foam after casting diminishing the degradation of the foam and preserving its fine and homogeneous internal structure. This approach was possible to apply since there were no profound effects of the elevated curing temperature on the equilibrium viscosity of epoxy gels.

The internal structure of the foams prepared was strongly dependent on the temperature of the suspension during foaming and curing. The different variants of foaming temperature, T_{foam}, and curing temperature, T_{gel}, used in our investigation are in the Table 4.

Table 4 The processing details, porosity and average pore and window size of the sintered samples

Foam Structure	T_{foam} (°C)	T_{gel} (°C)	$t_{process}$ (s)	Open Porosity* (%)	Pore Size (µm)	Window Size (µm)
A	35	50	540	76.1±1.2	214	46
B	35	35	540	74.2±4.0	172	48
C	25	50	240	82.1±4.2	644	135
D	25	35	360	78.1±0.9 (65.8)¥	317 (260)¥	78 (79)¥
E	25	35	660	82.4±1.0	464	117
F	25	35	960	73.2±0.9	287	73

*Mean of the open porosity given with 95 % confidence interval

¥ Values determined by CT analysis

The hardener was dosed to the suspensions at a foaming temperature (T_{foam}). Foaming and casting were performed at this temperature, as well. Once the suspensions were foamed, casted and sealed in the moulds temperature was changed to the curing temperature (T_{gel}). The processing time, $_{foam}$, between the hardener addition and a final placement of the sample to the environment with temperature set on the curing temperature varied from 240 s to the 960 s. The SEM microphotographs of the samples from the Table 4 after final sintering at 1250 °C are in the Figure 16. The microstructure of the sintered foams consisted of spherical pores with numerous circular interconnections between adjacent pores (referred as pore windows). The open porosity of the samples determined by the Archimedes method varied from 73 % to 82 %. The lowest values were measured for samples prepared from pre-heated suspensions and for the samples prepared with the longest processing times. The foams prepared from the suspensions preheated to the 35 °C were cured rapidly and the final microstructure of the samples (Figure 16 A and B) consisted of small pores (around 200 µm) and the open porosity of the samples reached 76 % and 74 %, respectively. On the other hand, the structure prepared at 25 °C and cured at 50 °C was defined by pores with the median size over 640 µm with open porosity reaching 82 % (Figure 16 C). We assume that main reasons for the biggest pore size of all prepared samples was caused by the synergic effect of Ostwald ripening and air expansion in the bubbles during curing. Structures with the pore size and porosity the closest to the ideal cellular structure described in the literature (see part 2.2.4 Internal Structure of Scaffold) were obtained by foaming of the suspensions at 25 °C with subsequentially curing at 35 °C with processing time of 6 minutes (Figure 16 D).

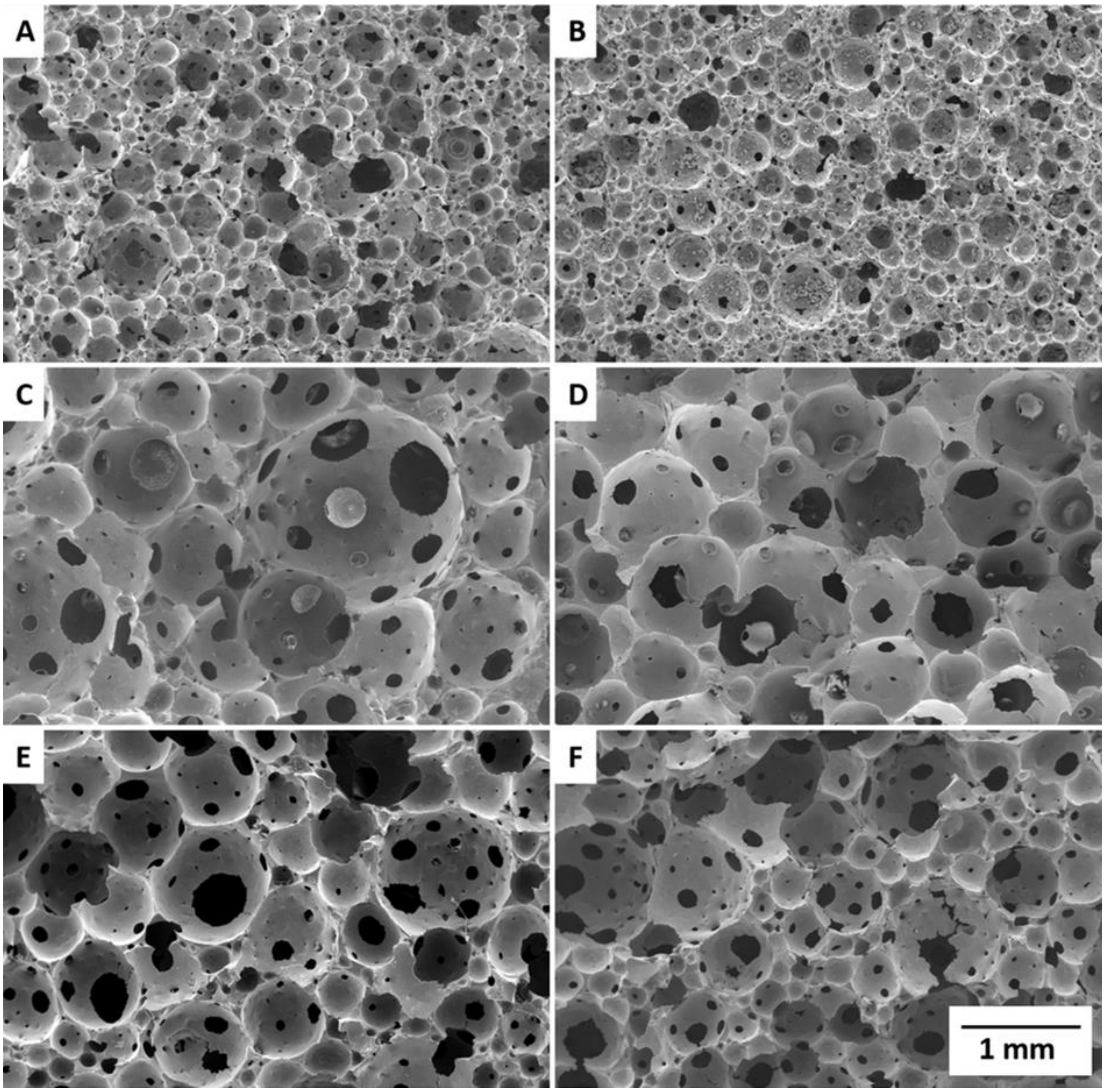

Figure 16 SEM microphotographs of sintered foam structures prepared with different processing parameters. (A) foam temperature: T_{foam} = 35°C, gelation temperature: T_{gel} = 50°C, and processing time: $t_{process}$ = 540 s; (B) T_{foam}= 35°C, T_{gel} =35°C, $t_{process}$ = 540 s; (C) T_{foam} = 25°C, T_{gel} = 50°C, $t_{process}$ = 240 s; (D) T_{foam} = 25°C, T_{gel} = 35°C, $t_{process}$ = 360 s; (E) T_{foam} = 25°C, T_{gel} = 35°C, $t_{process}$ = 660 s; (F) T_{foam} = 25°C, T_{gel} = 35°C, $t_{process}$ = 960 s.

Pore size, pore window size and open porosity of the all samples in the Figure 16 are in the Table 4. The structural characteristics of the sample D, which were found to be optimal for the purpose of the scaffolds preparation, were studied by CT analysis as well. The internal structure of the sample captured by CT is shown in the Figure 17. The most frequent pore size (volume-based) was in the case of both SEM and CT analysis the same with the most frequent diameter around 430 µm (Figure 18 A). The distribution of the pore windows differed and in the case of the SEM analysis the most frequent pore window diameter (by area) was 130 µm whereas the distribution acquired by CT was more broad with the most frequent pore windows diameter shifted to 150 µm (Figure 18 B). To explain this difference the size of dataset acquired must be taken in account. In the case of SEM analysis hundreds of pores were evaluated, CT scan evaluated hundreds of thousands microstructural features defined as pores and pore windows, respectively. Moreover, this shift can be cause by the projection skewness of the sample´s 3D surface captured in 2D microphotography. The histograms based on CT datasets were slightly skewed to the right (Figure 18). This skewing was caused probably by Ostwald ripening phenomena leading to foam degradation characterised with gradual coarsening of the foam microstructure.

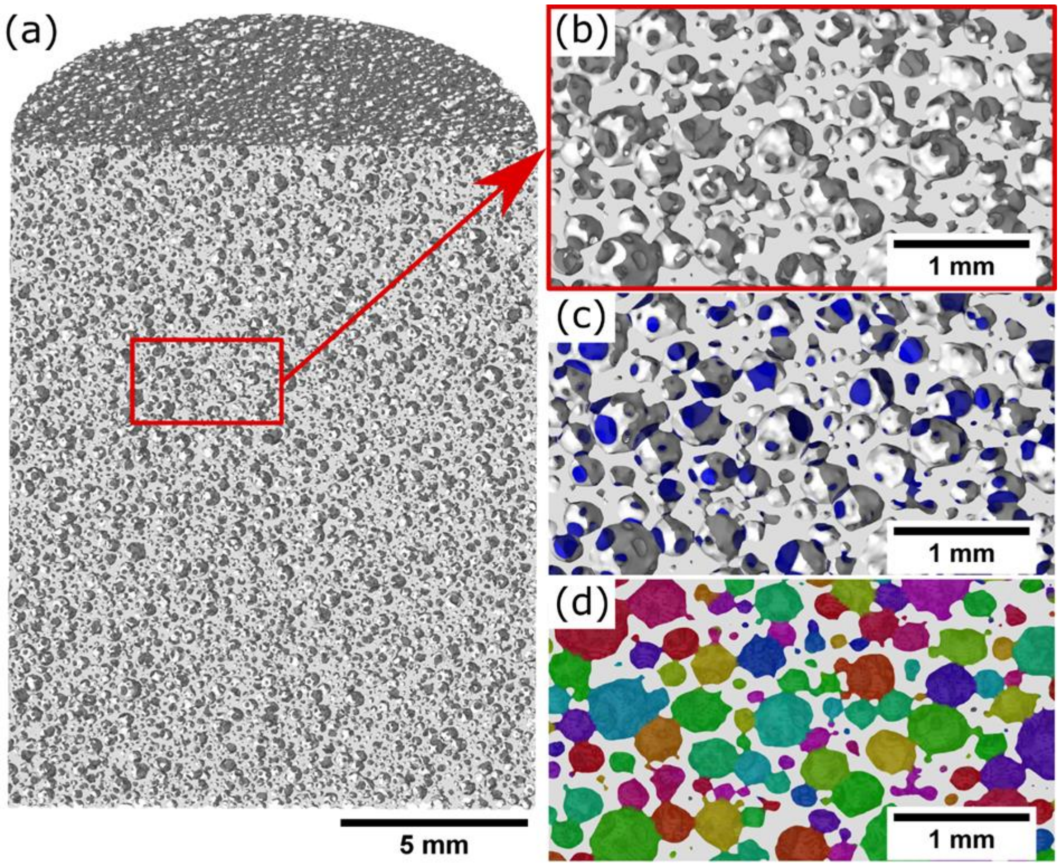

Figure 17 CT images and pore structure analysis of sintered foam (D). (a) cross section of the foam, (b) detail of the foam structure, (c) pore windows analysis, (d) pore size analysis.

This skewness is not obvious in case of datasets measured on SEM photos probably due to low number of individual measurements. Nevertheless, this quite well-matching comparison of internal microstructure justifies the utilization of the relatively simple SEM method as method valid for the basic evaluation of cellular-like structures and foams.

To characterize mechanical performance of porous structures, the compressive strength was evaluated. The average values and the Weibull parameters of compressive strength of hydroxyapatite foams are in the Table 5. The compressive strength of the foams in different processing stages was evaluated including the foams impregnated with paraffin wax which was supposed to improve milling accuracy. The paraffin impregnation significantly increased the compressive strength of dried foam. Moreover, paraffin impregnation improved the toughness of the dried structure as well. The work of fracture was increased from 0.33 mJ.mm^{-2} to 0.74 mJ.mm^{-2}. The internal structure of dried samples was flawless. Flawless internal structure was indicated by relatively high Weibull modulus reaching a value of 25.2. Paraffin wax impregnation increased the spread of compressive strength values and therefore decreased the Weibull modulus. The decrease of Weibull modulus was an indication of uneven distribution of paraffin wax rather than any indication of a damage on the foam microstructure. This explanation was supported by following findings. Pronounced benefit related to the paraffin impregnation was observed on the strength of the sintered samples. The impregnation of the green body followed by sintering of the samples impregnated with paraffin significantly improve strength of the sintered foam. If we compared compressive strength of samples sintered with and without previous impregnation, the strength of sintered samples increased by 108 % from 1.59 MPa to 3.32 MPa for samples impregnated with paraffin wax in a dried state. The reason could be explained by strength analysis of the samples sintered without paraffin impregnation. This group, consisting of 45 samples, could be divided into two groups – high and low-strength population (Figure 19). The low-strength population (32 samples out of 45) had Weibull strength of 1.07 MPa and Weibull modulus of 2.61, whereas the high-strength population (13 samples out of 45) had Weibull strength of 3.37 MPa and Weibull modulus reaching 6.59.

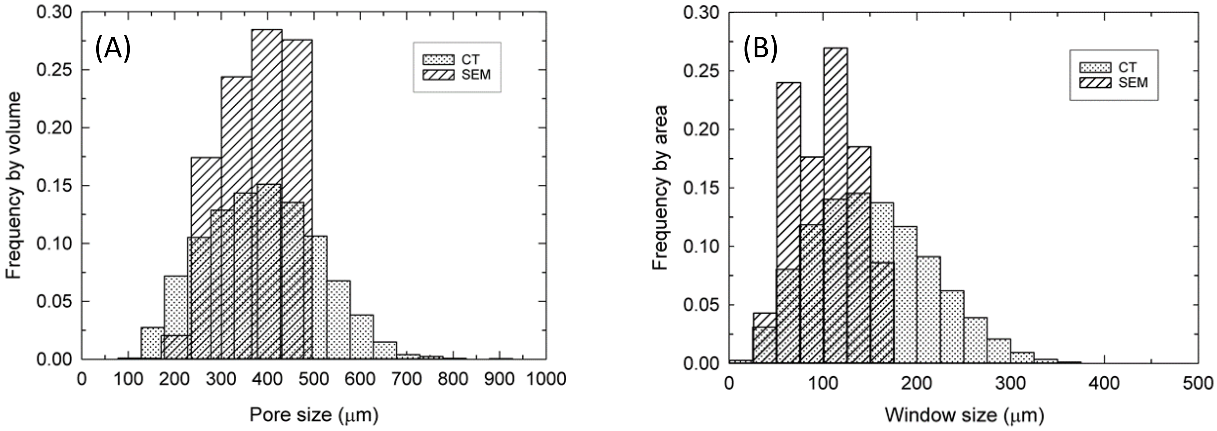

Figure 18 A) Pore size distribution of the structure D B) Pore window size distribution of the structure D. Comparison of SEM and CT analysis. Sintered foam

The results suggested different failure mechanism and presence of flaws of some kind. Mechanical strength of high-strength population could be correlated with mechanical strength of the samples sintered after paraffin impregnation. Such samples were characterised with Weibull strength of 3.58 MPa and Weibull modulus of 5.85. These results suggested, that the low strength population was eliminated in the case of the samples impregnated with paraffin. To explain this phenomena, debinded cylindrical samples with and without previous paraffin impregnation were inspected. Defects in the form of central cracks which did not always reach surface of samples, were found after cutting the sample perpendicular to its long axis (Figure 20). No suchlike defects were found in the case of samples impregnated with paraffin before sintering. The central crack is common drying defect of green bodies [243]. Uneven drying of a gel results in internal stress field in a dried body. The stress field do not have to result in a crack formation in a green body, where the polymeric part is strong enough to withstand forces originated from the internal stress field. During debinding, polymeric network is removed, and stress is released. The stress release could lead to crack formation and consequently to lower strength of sintered ceramic. To explain the effect of paraffin, thermal analysis was conducted. It was shown that infiltrated

Table 5 Compressive strength of the hydroxyapatite foams tested at different processing stages

Sample	Average Strength (MPa)	Number of Samples (-)	Weibull Strength (MPa)	Weibull Modulus (-)
Dried	0.38	10	$0.38^{+0,01}_{-0,01}$	$25.2^{+18,2}_{-11.0}$
Dried and impregnated	1.64	10	$1.77^{+0,26}_{-0,22}$	$5.47^{+3,95}_{-2,40}$
Sintered (dried only)	1.59	45	$1.07^{+0,17}_{-0,15}$ * $3.37^{+0,34}_{-0,31}$¥	$2.61^{+0,76}_{-0,79}$ * $6.59^{+3,12}_{-3.35}$¥
Sintered (dried and impregnated)	3.32	36	$3.58^{+0,23}_{-0,22}$	$5.85^{+1,59}_{-1.66}$

*Low-strength population of the samples

¥ High-strength population of the samples

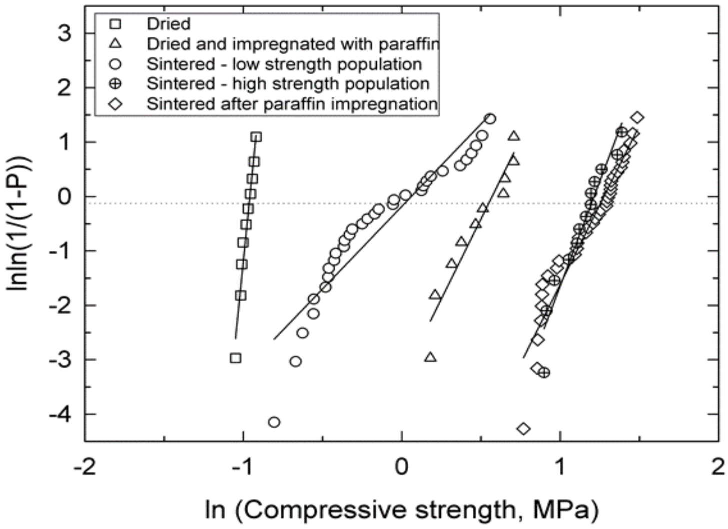

Figure 19 Weibull plots of compressive strength of the hydroxyapatite foam at a different processing stage

paraffin got melted during debinding and affected the degradation and the removal of epoxy-based polymeric network. The temperature range of paraffin decomposition (boiling point 300 °C) coincided with epoxy-based gel decomposition (200 – 350 °C). In this temperature range about 80 wt. % of epoxy gel was removed. Therefore, we hypothesized that capillary forces of molten paraffin could rearrange ceramic particles during the gel removal. The particle reorganization eliminated inhomogeneity in the ceramic body caused by drying process. The elimination of inhomogeneities resulted in a low intensity or no internal stresses at all. Low or no internal stresses prevented crack formation in debinded bodies and resulted in improved compressive strength of sintered ceramic foams.

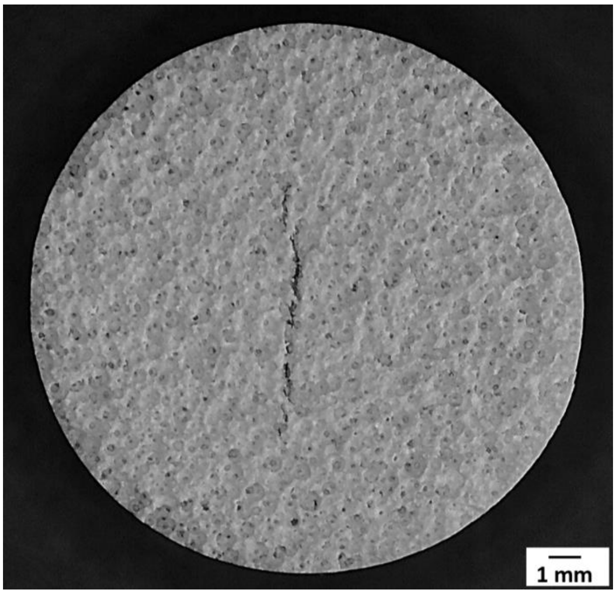

Figure 20 Image of cross-section of debinded body with an internal crack

The milling tests were performed using the milling pattern shown in the Figure 21(a). Milling pattern with distinctive features allowed us to evaluate the precision of milling. Namely: smoothness, sharpness and continuity of edges, quality of tiny details and fragile features. The diameters of the pins were 3 mm, 6 mm and 9 mm. Angle of the wedge was 30° and step-like feature was designed with 1 mm steps and thickness of individual steps equal to 2 mm, 4 mm and 6 mm, respectively. Based on the previous results described in this work, only the structures referred a D, providing structural properties needed for bone regeneration, were used for milling tests. The foam blanks (cylindrical samples, d = 40 mm, h = 30 mm) were milled in different stages of heat treatment (dried, presintered, sintered). All samples were tested with and without the paraffin impregnation to compare influence of paraffin on milling performance. The milled parts after final sintering are shown in the Figure 21 b - f. The best results were obtained by milling blanks in a dried-only stage and dried-and-impregnated stage (Figure 21 b, c). Paraffin impregnation significantly improved the precision of cut and sharpness of edges. Moreover, the paraffin layer on a dried ceramic body improved stiffness during milling and acted as scaffolding of the fragile ceramic structure. The only drawback related to the paraffin impregnation was creation of a paraffin-dust mixture which had a tendency to be stuck-in some pores. It was not possible to clean this mixture before final sintering. Therefore, after final sintering the blockage of some surface pores by ceramic dust was observed. Blanks milled in the pre-sintered state did not posses enough ductility and strength to withstand the milling without any damage (Figure 21 d).

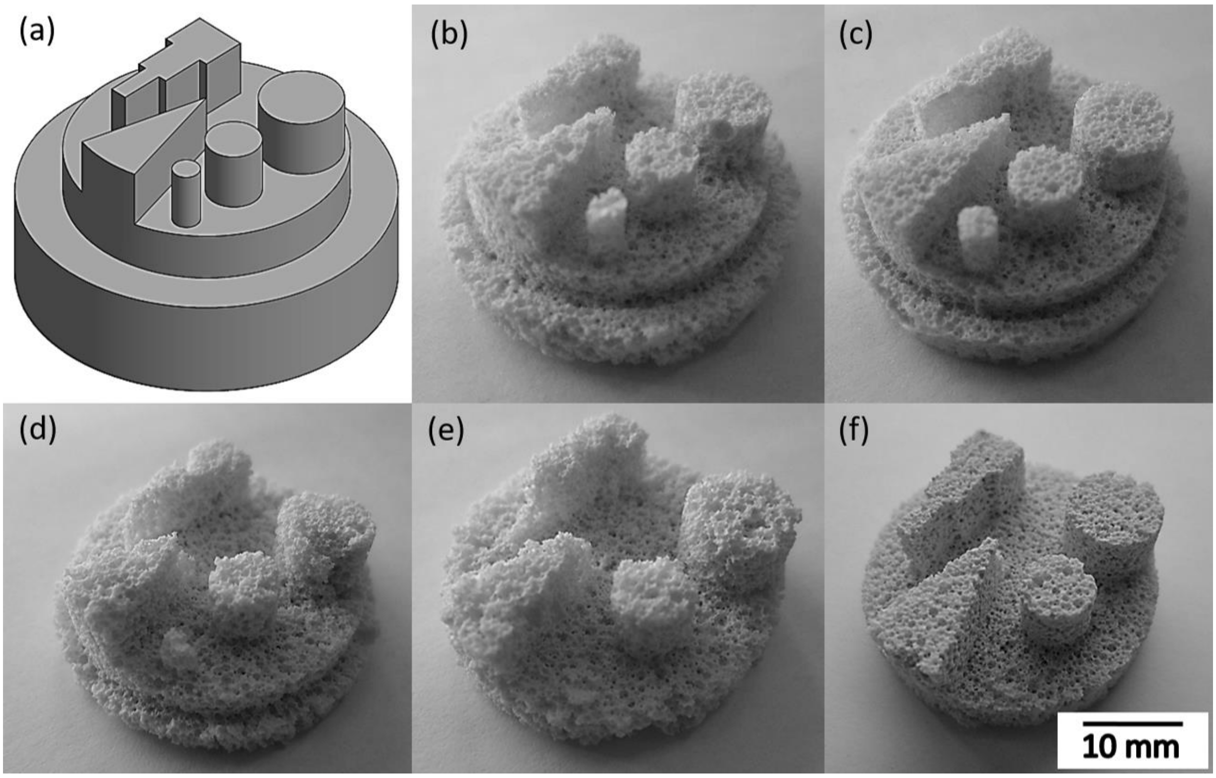

Figure 21 Results of milling test. All samples a – f after final sintering (a) milling pattern, (b) dried foam. (c) dried foam impregnated with paraffin wax, (d) presintered foam at 1150°C/2 h, (e) sintered foam at 1250°C/2 h, (f) sintered foam at 1250°C/2 h and impregnated with a paraffin wax.

The presintered samples impregnated with paraffin wax were destroyed during final sintering due to insufficient strength of the ceramic structure. The most plausible explanation was that presintered structures were destroyed by paraffin expansion in micropores in the porous walls during heating of the sample to the sintering temperature. The blanks milled in sintered state were too brittle to be machined with a high precision (Figure 21 e). The milling of sintered samples resulted in damaged parts with poor overall quality. As in the case of dried sample, paraffin impregnation of sintered blanks resulted in substantial improvement in the quality of milled parts (Figure 21 f). Unfortunately, brittleness of the sintered blanks did not allow to machine the tiniest details. The overview of the milling tests is summarized in the Table 6. The evaluation was performed by using qualitatively based scale. The milling performance and customization capacity of 3D ceramic scaffolds by milling were demonstrated by preparation of a large ceramic scaffold for mandible treatment. The CT-scanned data were used for both 3D printing of polymer model of the mandible and for milling of the ceramic scaffold (Figure 22). Thanks to high resolution 3D scan, part with outstanding dimension and shape accuracy could be obtained. The perfect fit of the scaffold in the defect

Table 6 Evaluation of milling tests

Thermal Treatment	Impregnation	Milling Results	Notes
Dried	-	Good	Rough edges and surfaces, tiny parts ok
Dried	Paraffin	Excellent	Sharp edges, smooth surfaces, tiny parts ok
1150°C/ 2 h	-	Bad	Jagged edges, very rough surfaces, tiny parts broken
1150°C/ 2 h	Paraffin	N/A	Destroyed during dewaxing
1250°C/ 2 h	-	Bad	Jagged edges, very rough surfaces, tiny parts broken
1250°C/ 2 h	Paraffin	Good	Sharp edges, smooth surfaces, some tiny parts broken

site is shown in Figure 22 a and non-trivial internal structure of the scaffold is shown in Figure 22 b.

3.2.4 Summary

This chapter described the preparation of the HA foams. Several types of the foam preparation were tested and evaluated. The structure with median pore size of 317 µm and open porosity of 78 % was evaluated as the best one with respect to intended applications. The compressive strength was evaluated on the samples D. The compressive strength of 3.3MPa was obtained. Positive effect of paraffin impregnation both on mechanical properties and machining was described. The foaming method and paraffin impregnation will be used in following chapters for preparation of porous calcium phosphate scaffolds.

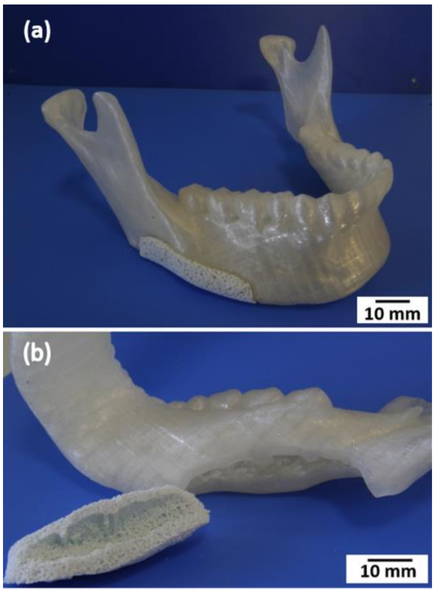

Figure 22 (a)Model of human mandibula with a defect filled with the customized hydroxyapatite scaffold, (b) detail o the defect in madibula and the internal shape of the scaffold.

3.3 Strength and Structure Degradation of Calcium Phosphates under Simulated In-Vivo Conditions

The method of the calcium phosphate foam preparation by novel direct foaming method based on water-based epoxy system, successfully tested, and described in previous chapter, was exploited for preparation of calcium phosphate foams with different phase compositions. The multiphasic composition was tested as a possible solution for biodegradable scaffolds. Moreover, the multiphasic calcium phosphates are believed to be the key for governing of the dissolution/degradation rate of the ceramic scaffolds *in-vivo*. The main target of this part was to test CaP foams with different phase compositions in simulated *in-vivo* conditions. The effect of the phase composition both on the structural and mechanical properties is discussed in this chapter.

3.3.1 Scaffolds Preparation

Three types of ceramic foams (scaffolds) were prepared differing in the phase composition. Namely, pure hydroxyapatite (HA), β – tricalcium phosphate (TCP) and biphasic calcium phosphate (BCP) foams were prepared. The basic steps of the scaffolds preparation coincided with the steps having already been described in the chapter 3.2 (schematically depicted in Figure 12). Here only slight differences in a preparation of TCP and BCP suspensions are described. Hydroxyapatite suspensions were prepared in the same way as described previously using hydroxyapatite powder (tri-calcium phosphate extra pure, Riedel-de Haen, Germany). Tricalcium phosphates (TCP) suspensions were prepared using tricalcium phosphate powder (Calcium phosphate, purum p.a. > 96 %, Honeywell, Germany). The preparation of TCP suspensions were the same as HA suspensions with one exception. Because of the coarser powder, the total time of attritor milling was extended to 8 hrs. Prolonged milling time resulted in suspensions with median particle size of 1 µm. If milling time of 3 hours was applied, median particle size was close to 6 µm. This lead to significant instability of TCP suspensions characterised by quick sedimentation. Biphasic calcium phosphate (BCP) suspensions were prepared by direct mixing of HA and TCP suspensions. The HA and TCP for the preparation of BCP suspensions were prepared according to the standard protocol. Milled HA and TCP were mixed in desire ratio (calculated as a HA/TCP powder ratio), in the case of this study HA/TCP ratio was kept 1:1 (in wt. % of powders dispersed). The mixture was stirred for 15 minutes to homogenize it before foaming and casting. Prior foaming the foaming agent Triton X-100 (Triton X-100, Sigma-Aldrich, Saint Luis, MO, USA) and amine hardener (DPTA) (bis(3-aminodipropyl) amine, Sigma-Aldrich, Steinheim, Germany) were added. The foaming and casting parameters were adopted from previous chapter and coincided with the parameters described in Table 4 for the structure referred as „D“. The samples were casted as cylinders with a diameter 20 mm and the height of 30 mm. Before heat treatment the samples were impregnated with paraffin wax to improve mechanical strength after sintering. The heat treatment was the same for all types of the samples. The paraffin wax and epoxy gel were removed by heating at a rate of 50 °C/ h to 500 °C and then the sintering step followed by heating at a rate of 120 °C/ h to sintering temperature of 1250 °C. There was 2 h dwell at sintering temperature followed by cooling with a rate of 60

°C/ h to the room temperature, if not mentioned otherwise. The composition of suspensions prepared are in the Table 7.

Table 7 Composition of the ceramic suspensions

	HA powder		TCP powder		DI Water	EGDGE	DPTA	Darvan 821A	Triton X-100
	Wt.%	Vol.%	Wt.%	Vol.%	Wt.%	Wt.%	Wt.%	Wt.%	Wt.%
HA	58.5	31.4	-	-	30.8	5.9	1.8	0.7	2.3
TCP	-	-	61.1	34.4	28.0	5.4	1.6	0.6	3.3
BCP	29.7	16.1	29.7	16.6	29.0	5.7	1.7	0.7	3.5

3.3.2 Tests of Simulated Biodegradation

The osteoclastic activity was simulated on the sintered ceramic foams in a form of cylindrical samples with a diameter of approximately 15 mm and height of 24 mm by submerging the sintered samples into acidic solution of McIlvaine buffer (pH 5.5). The buffer enabled to perform the degradation tests 14 days long. These tests revealed the microstructural changes and allowed correlations of the microstructural changes with changes in mechanical strength of the scaffolds. Long-term degradation tests served as an approximation of the actual regeneration and resorption process of sintered ceramics in a living organism (see chapter 2.2.2 Solubility and Degradation of Calcium Phosphates). The samples for mechanical testing were degraded for 2, 7 and 14 days in McIlvaine buffer. The buffer solution was prepared as a mixture of 0,1 M solution of citric acid (citric acid monohydrate, p.a. 99.5 %, Penta, Czech Republic) and 0.2 M solution of disodium phosphate (disodium phosphate dodecahydrate, Lachema, Czech Republic). The set of samples of each type (HA, TCP, BCP) was placed into separate beakers and submerged into buffer solution keeping the ratio of 10 g of buffer per 1 g of sample. The beakers were sealed to avoid a drying and placed into a chamber with constant temperature of 37 °C. Buffer solution was changed every two days. The change of buffer´s pH was measured prior to the regular exchange of the buffer. After the time reserved for degradation test passed, the samples were gently washed in deionized water. The mechanical strength of degraded samples was tested in a wet state to minimize all effect which could be possibly introduced by drying (cracking etc.). The weight changes were evaluated on washed and dried samples.

3.3.3 Characterization of Microtructure and Mechanical Characterisation

SEM micrographs (Veriosl 460L, FEI, Czech Republic and Lyra3, Tescan, Czech Republic) of all types of sintered samples before and after degradation (2, 7 and 14 days) were taken to show the effect of acidic environment on microstructural features. The porous macrostructure of the sintered samples was characterised by the pore size and the size of pore interconnections (windows). Gwyddion software (Gwyddion 2.49, Czech Republic) was used to measure the pore and window sizes on SEM micrographs. The sizes of pores and windows were measured on fracture surface. At least 150 measurements were performed on each type of sample. The pores and windows were considered to be spherical and circular, respectively, and no correction factor was applied to take in account the skewness of a projection and location of a fracture with respect to the pore diameter. The most frequent pore and windows sizes were determined as the median value of the most frequent bin in histogram. The frequencies by volume and area were used, respectively. This method had been proven as a reliable method how to provide basic characteristics of the scaffold structures (see chapter 3.2). The grain size of sintered ceramics was evaluated from the micrographs of the pore walls. At least 150 grains for each type of ceramic material (HA, TCP, BCP) were measured. The average grain size was calculated by the linear intercept method. Open and closed porosities of the samples were measured by Archimedes method. Theoretical densities of 3.16 $g.cm^{-3}$ for HA, 3.07 $g.cm^{-3}$ for β-TCP and $Ca_2P_2O_7$ and 2.87 $g.cm^{-3}$ for α-TCP were used. The median density was calculated based on a phase composition of the samples after sintering. The XRD measurements of the phase composition were performed on Rigaku SmartLab diffractometer (Rigaku SmartLab 3 kW, Rigaku, Japan). Diffraction analysis was performed in Bragg-Brentano configuration from 10° to 100° (2θ) with Cu Kα radiation. Samples for XRD analysis were prepared from dried samples, having been powdered in mortar. The phase content was quantified by the Rietveld analysis. To evaluate mechanical performance of the samples before and after degradation compressive strength was measured. ISO 13314 referring to the mechanical testing of porous and cellular metals was cautiously adapted. Samples were cylindrical with a diameter of 15 mm and a height of 24 mm. The hight to diameter ratio was kept 1.6. Fifteen samples of each group (HA, TCP, BCP) for each time point (0, 2, 7, 14 days) were tested. As it has been mentioned in previous text, degraded samples were tested in wet state. Compressive strength and energy absorption were measured using MTS Mini Bionix 858.02 system (MTS, USA) equipped with 1000 N and 250 N cells. The measurements were carried out at a constant crosshead speed of 4.0 mm per minute. The stress–strain curves were recorded and used for the evaluation of ultimate compressive strength and an energy absorbed during fracture. The ultimate compressive strength was calculated as the maximum on stress-strain curve divided by the cross-sectional area of sample tested. Absorbed energy was calculated as the area under the stress-strain curve up to 20 % strain divided by the sample volume. The parameters of the Weibull distribution were calculated numerically according to the EN 843-5 standard. The distribution of CaP phases in sintered BCP ceramics was determined by the electron backscatter diffraction (EBSD) performed on a SEM (Verios 460L, FEI, Czech Republic) equipped with EBSD detector (EDAX DigiView IV, EDAX, Germany). Raw data were analysed in a data analysis software (OIM analysis v8, EDAX, Germany). The

EBSD analysis was performed on dense sintered samples prepared the same way as porous samples, omitting just foaming step.

3.3.4 Results and Discussion

Sintered ceramic samples exhibited cellular-like structure with interconnected porosity and circular pores. The porosity of samples reached the values 82 – 85 %, depending on the type of the sample. From microstructural point of view the samples were very similar to each other and no profound differences between HA, TCP and BCP scaffolds were found (Figure 23 a-c). The pore size ranged from 200 µm to 1.2 mm. Pores were interconnected by windows with a diameter in a range of 50 µm to 450 µm. The basic characteristics of the foams are in Table 8. Taking in account confidence interval, open porosity could be considered the same for all three types of the samples. The most frequent pore size and windows size could be considered same as well. Therefore, it was possible to consider HA, TCP and BCP the same from microstructural point of view and differences in their compressive strength before and after degradation were contributed only to their phase structure. The only profound difference was found in a grain size of sintered samples. In the case of HA, the ceramic walls were fine-grained with an average grain size of 1.7 µm. The microstructure of TCP bodies was created by the grains with average grain size reaching 5.9 µm. Multiphasic samples were characterized with a grain size around 2.2 µm. The microstructure can be described as a bimodal in the case of BCP. The phase composition of sintered scaffolds is summarized in Table 9. The HA samples were confirmed to be single-phase HA after sintering at 1250 °C for 2 hrs. The samples labelled as TCP were, in fact, biphasic. The major phase was β-TCP as expected with minor $Ca_2P_2O_7$ (calcium pyrophosphate) phase.

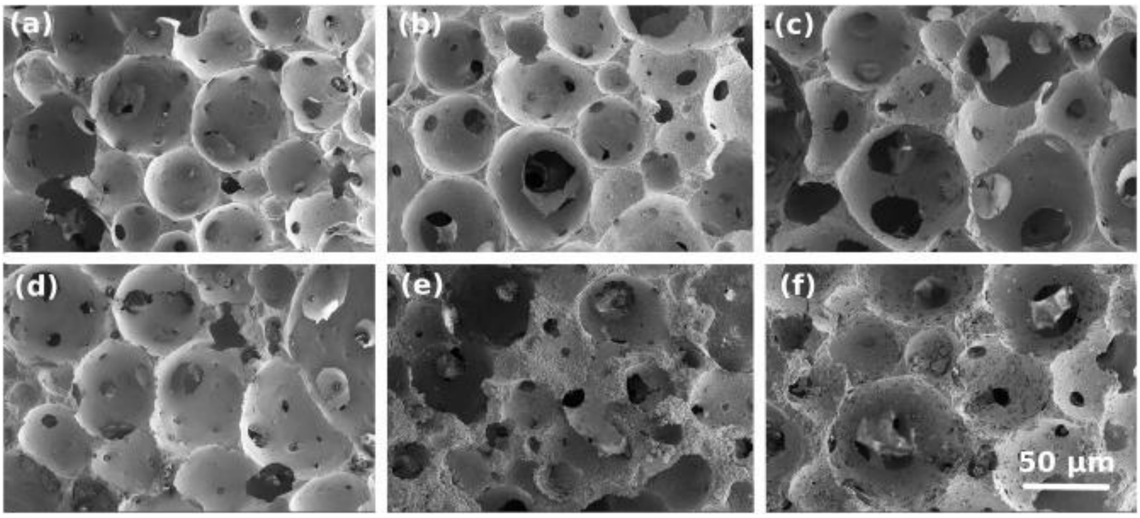

Figure 23 SEM micrographs of the macrostructure of the HA scaffold (a) and (d), TCP scaffold (b) and (e), and BCP scaffold (c) and (f) before and after degradation (14 days), resp.

Table 8 Basic characteristics of the HA, TCP and BCP scaffolds

Sample	Open Porosity* (%)	Pore Size$^+$ (µm)	Window Size$^+$ (µm)	Grain Size (µm)
HA	83.1±0.7	702	188	1.7
TCP	82.3±0.7	623	244	5.9
BCP	84.9±1.1	698	184	3.4

*Sample mean is given with 95% confidence interval of normal distribution

+The most frequent size

Calcium pyrophosphate was found in the β-TCP powder in as-received state. Calcium pyrophosphate is a common impurity in β-TCP powders. The amount of calcium pyrophosphate before and after sintering did not change and was determined as 11 wt.% by Rietveld refinement of XRD spectra. The phase structure of BCP samples changed dramatically after sintering resulting in the mixture of HA, β-TCP and α-TCP. This can be attributed to the high temperature reaction of HA with $Ca_2P_2O_7$. It has been described that around 900 °C HA and calcium pyrophosphate can react and create TCP [240]. This phase shift and its impact on mechanical and biological properties of BCP scaffolds will be discussed in following text. Triphasic structure was also confirmed by EBSD phase analysis where the distribution of individual phases was identified as well. The EBSD phase mapping performed on dense BCP sample confirmed the α-TCP phase with rather interesting distribution. The main occurrence of α-TCP was along the grain boundaries of HA and TCP grains whereas both HA and β-TCP were distributed evenly in the form of uniaxial grains (Figure 24). Regarding the uniformity of the phase distribution, no profound clustering of individual phases in BCP was found. The homogeneity of the phase distribution suggested that grain size of BCP somewhere between grain size of pure TCP and HA could be attributed to the multiphase composition. This is a well-known fact, that in the case of multiphasic structures grain growth of one phase can be restricted and hindered by second phase in its vicinity [244]. Moreover, bigger grains in the BCP structure were indexed as β-TCP whereas smaller grains were indexed as HA. This result is in good agreement with initial particle size of the suspensions used. The changes in a phase structure of the samples over degradation period are in Table 9. The phase composition of HA samples did not change during 14 days of degradation test and the composition remained single phase HA. This behaviour was in accordance with our expectations. The similar behaviour was observed even in the case of TCP scaffolds. The two phases identified by XRD

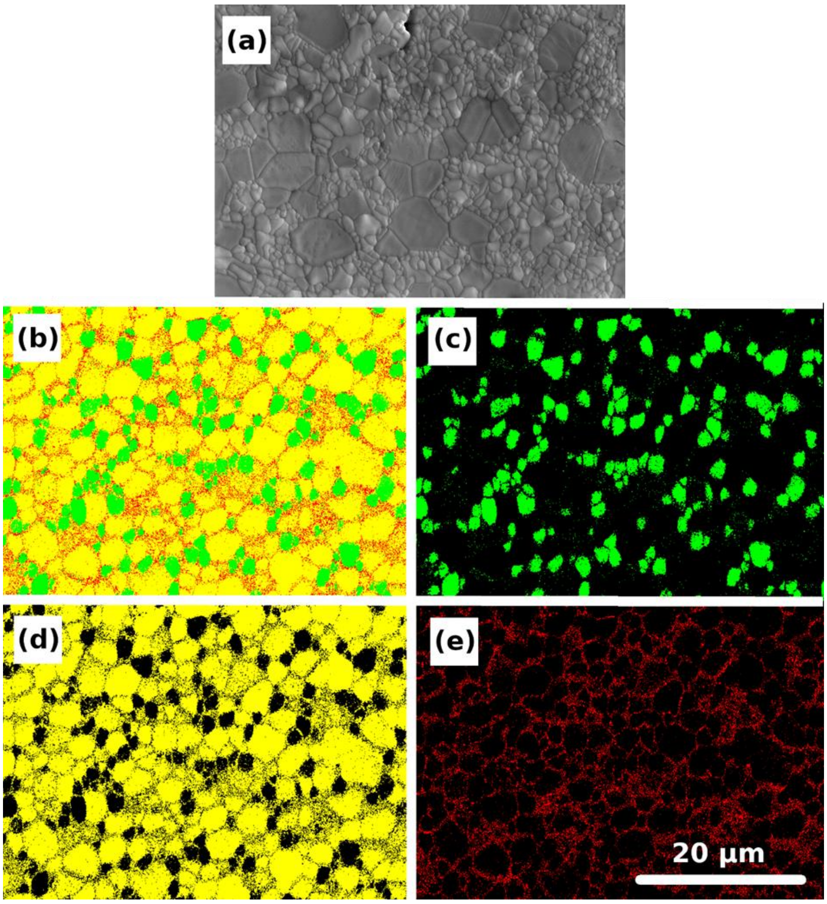

Figure 24 SEM image of the BCP ceramics (a) and EBDS phase mapping of all phases (b), HA phase (c), β-TCP phase (d), and α-TCP phase (e). SEM image does not correspond to the place of EBSD analysis

in sintered TCP samples (β-TCP and $Ca_2P_2O_7$) remained in the structure with slight ratio shift towards $Ca_2P_2O_7$ during the degradation process. The ratio of β-TCP/$Ca_2P_2O_7$ changed from 8.09 to 6.14. This shift can suggest preferential dissolution of β-TCP. The phase composition of BCP scaffolds was characterized by XRD with approximately 12 % α-TCP in the structure. The α-TCP disappeared during the first two days of degradation test leaving just β-TCP and HA in the structure (Table 9). Just negligible amount of α-TCP was detected in a structure of the sample after 2 days of the degradation. The ratio of β-TCP and HA remained almost the same during the degradation, reaching 2.38 before degradation and 2.57 after degradation, respectively. The β-TCP/HA remained stable from the day 7. The stability of β-TCP/HA ratio in BCP samples is proof of rapid dissolution of α-TCP. The corresponding morphological changes of sintered ceramics during the degradation are shown in the Figure 23. The macrostructure of the HA was almost intact after 14 days. Just negligible leaching of a surface and leaching along grain boundaries took place. The changes on HA microstructure can be defined as very low. On the other hand, the microstructure of TCP and BCP samples exhibited substantial changes. Changes were pronounced especially in the case of BCP scaffolds, where degradation of the thin pore walls resulted in creation of new interconnections. Due to the similar pattern on all samples we assume that the degradation started along grain boundaries as the weakest

Table 9 Phase composition of the samples before (0 day) and after exposition to the acidic environment (2, 7 and 14 days)

Sample	Degradation Time (d)			
	0	2	7	14
HA	100% HA	100% HA	100% HA	100% HA
TCP	89% β-TCP 11% $Ca_2P_2O_7$	88% β-TCP 12% $Ca_2P_2O_7$	86% β-TCP 14% $Ca_2P_2O_7$	84% β-TCP 14% $Ca_2P_2O_7$
BCP	62% β-TCP 12% α-TCP 26% HA	71% β-TCP 1% α-TCP 28% HA	72% β-TCP 28% HA	72% β-TCP 28% HA

point of the microstructure. This mechanism was obvious in the case of TCP samples. Significant etching along the grain boundaries could be observed after 14 days of degradation test (Figure 25 e). In the TCP and BCP samples weakening of grain boundaries was characterized by the loss of individual grains (TCP) or whole grain clusters (BCP) (Figure 26).The etching of the grain boundaries itself was less pronounced in the case of BCP samples, where the most characteristic features were deep pit holes (Figure 25 f). The mass loss of the scaffolds during degradation corresponded to the microscopic observations. The highest mass loss was recorded in the case of TCP scaffolds reaching 19 % followed by BCP with 15 % (Figure 27). The mass loss in the case of HA scaffolds was rather moderate reaching 3 % after 14 days of degradation (Figure 27). The dissolved material (calcium and phosphate ions) increased the pH of the acidic environment. The dependence of the pH change of acidic environment on the time (prior to its periodical exchange, every two days) is in the Figure 28. The buffer solution with the BCP scaffolds exhibited the highest pH shift from initial value. The highest shift was measured during the first periodical buffer change after 2 days when the pH value reached 5.95. This corresponds to XRD observations, where α-TCP disappeared during first two days of degradation (Table 9). The increased ionic concentration was beyond of a buffering capacity of McIlvain buffer which caused an increase in pH value. The exponential like decrease in pH change was observed during the whole testing period for BCP. The only exception occurred at the day eight, where steep increase of pH occurs. We were not able to explain this change. Since negligible increase in pH within the error of measurement was observed even for HA and TCP, we assume that this behaviour was a random mistake of some kind introduce during periodical buffer change. The pH change of the solutions with submerged TCP and HA scaffolds

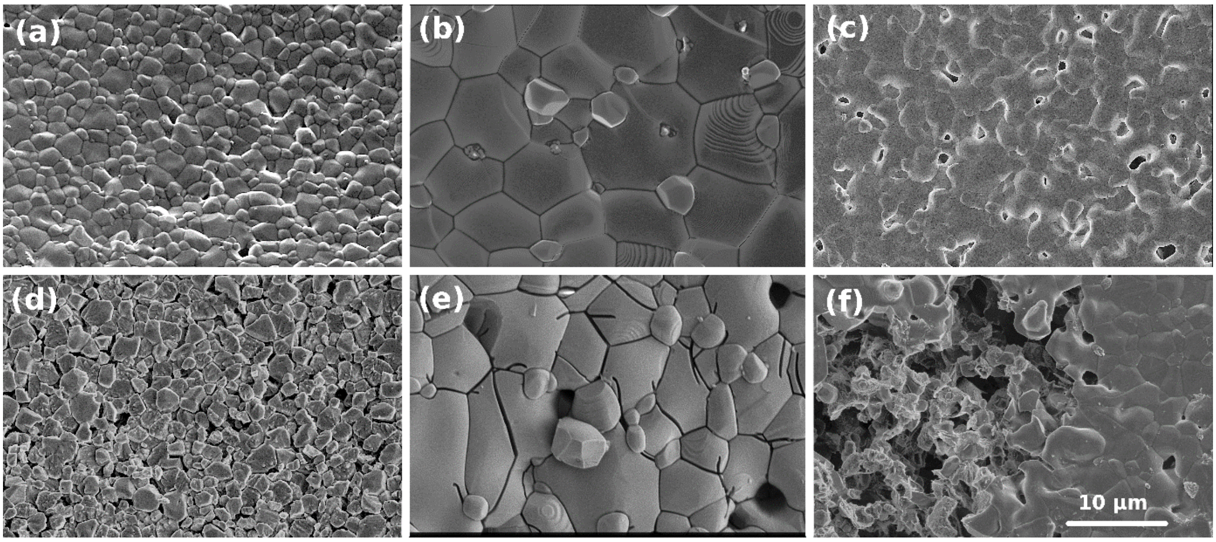

Figure 25 SEM micrographs of the microstructure before and after degradation of the HA scaffold (a) and (d), TCP scaffold (b) and (e), and BCP scaffold (c) and (f), resp.

was lower compared to the BCP scaffolds. The trend of pH increase was decreasing over the time, coming close to the original pH value of buffer solution after 14 days. The lowest changes in pH of buffer solution were observed in case of HA, which was in good agreement with microstructural changes and overall stability of HA samples. The mechanical characteristics defined by average and Weibull strength of the scaffolds before and after degradation are given in the Table 10. Lower strength of HA scaffolds (compared to the values from Table 5) can be explained due to higher porosity of this particular samples set [85] and slightly different measurement method. The Weibull plots corresponding to the Table 10 are shown in Figure 29. The statistical analysis of the results revealed that the average strength of the scaffolds before degradation was similar for HA and TCP samples. The BCP samples exhibited higher strength which can be attributed to the microstructural features (bimodal grain size) and multiphasic (composite) structure. The synergic effect of grain size and different phase composition is the most probable explanation, since other microstructural parameters (pore size, porosity etc.) were similar for all types of samples. The Weibull modulus, describing data scatter, was the same for all groups before degradation test. The energy absorbed during the strength test was statistically higher in case of the BCPs. The absorbed energies before degradation were 0.151, 0,063 and 0.097 MJ.m^{-3} for BCP, TCP and HA, respectively. After 14 days of degradation test the average strength of HA scaffolds was not affected. The ultimate strength of both TCP and BCP scaffolds were significantly affected (reduced) by degradation and both TCP and BCP exhibited exponential like decrease of ultimate strength value (Figure 30). The ultimate strength of BCP decrease from 1.67 MPa to 0.5 MPa after 14 days of degradation (70 % decrease). The decrease of the ultimate strength in case of TCP scaffolds were steep during first two days and then the trend was like the strength decrease of BCP scaffolds. The ultimate compressive strength of TCP scaffolds dropped from 1.22 MPa to 0.09 MPa after 14 days of degradation (93 % decrease) (Table 10). The same trend and similar values were observed in the Weibull strengths. Weibull modulus of individual groups did not change significantly. Based on Weibull plots, we can assume that fracture mechanism was

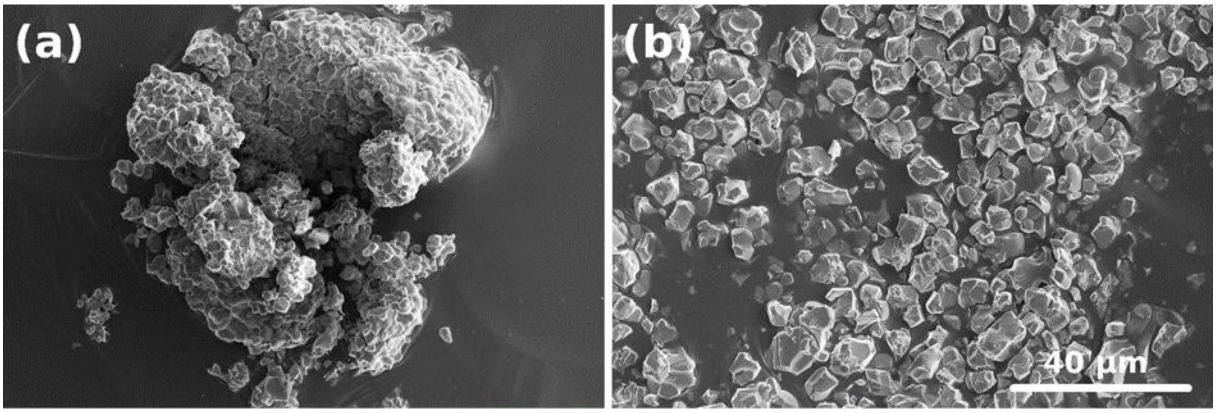

Figure 26 SEM micrographs of ceramic grains or grain clusters fallen out from the structure of the BCP scaffold (a) and TCP scaffold (b) during degradation in the acidic environment.

same for all samples within the individual groups. Comparing all groups together, TCP samples after 14 days of degradation exhibited the highest data scatter. This can be correlated with low strength of TCP scaffolds and substantial changes of a microstructure at a grain level, where deep etching along individual grain boundaries occurred. Therefore, majority of TCP material volume was affected by a degradation. Interestingly, even though the microstructure of BCP samples significantly changed data scatter was low. This can be attributed to significant but localised changes in a form of numerous pit holes. These pit holes served as the most significant defect of internal structure, decreasing the strength but keeping fracture mechanism same for all samples. Just slight shift of the Weibull plots for HA samples supports the idea of negligible surface etching of the samples which did not significantly affect the strength values. Considering all results, we can claim that the phase structure of the sample seems to be the most significant parameter influencing the response to the degradation of sintered CaP ceramics. The analysis of BCP scaffolds did not correspond to expected composition according to their initial mixing ratio. This discrepancy can be attributed to the phase composition of raw powders used as already mentioned. Whereas HA powder was single phase consisting only of HA the TCP powder was mixture of β-TCP (89 %) and $Ca_2P_2O_7$ (11 %) as impurity. After sintering, TCP powder kept the phase composition of raw powder. However, phase composition of BCP samples was rather shifted towards higher content of TCP. According to the literature findings [240], the calcium pyrophosphate ($Ca_2P_2O_7$) can react with hydroxyapatite during sintering according to the equation:

$$Ca_2P_2O_7 + 2Ca_5(PO_4)_3OH \rightarrow 4Ca_3(PO_4)_2 + H_2O \qquad (2)$$

Theoretical phase composition calculated according to this equation (neglecting type of TCP) contains 28 % of HA and 72 % of TCP. This theoretical composition is very close to the experimentally measured composition of 26 % of HA and 74 % of TCP (Table 9). The part of TCP content was retained in the high temperature form since the sintering was performed above alpha to beta transformation temperature of TCP (1125 °C). We hypothesized that at low temperature the yield of reaction was created by β-TCP but overcoming phase transformation temperature from β to α and due to high content of calcium pyrophosphate in BCP mixture, the

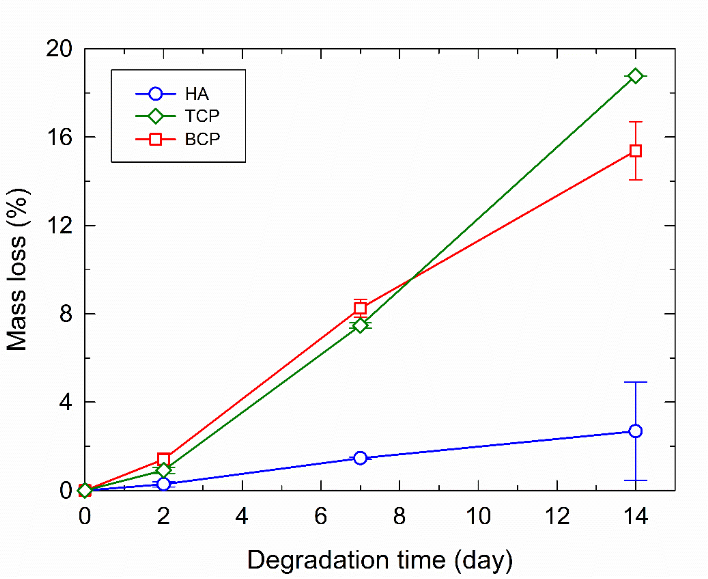

Figure 27 The mass loss of the scaffolds during degradation. The error bars show the standard deviation.

reaction was finished above transformation and product of the reaction was stabilized as α-TCP. According to the EBSD scan (Figure 24), it seems that the majority of α-TCP was located along grain boundaries. It worth mentioning that the lack of detailed analysis can be reason for controversial reports on sintering behaviour of BCP found in literature [134, 245]. The detailed description of phase distribution substantially contributed to the understatement of degradation of CaP scaffolds and mainly BCP scaffolds. The most soluble phase in BCP samples was α-TCP.

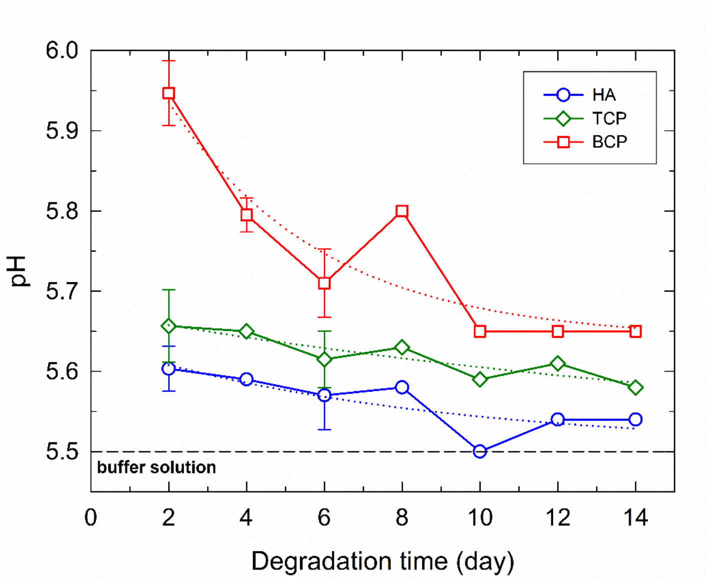

Figure 28 The pH change of medium with submerged HA, TCP and BCP scaffolds before regular solution exchange as a function of degradation time. Error bars show standard deviations. The dotted lines show the date trend.

Table 10 Average values and Weibull parameters of ultimate compressive strength of the scaffolds before and after degradation

	Compressive Strength			
Sample/Degradation Time	Average Strength*	Number of samples	Weibull Strength⁺	Weibull Modulus⁺
	(MPa)	(-)	(MPa)	(-)
HA/ 0 h	1.20±0.28	14	$1.31^{+0,18}_{-0,16}$	$4.85^{+2.73}_{-1.82}$
TCP/ 0 h	1.22±0.32	15	$1.34^{+0,22}_{-0,19}$	$3.82^{+2,05}_{-1,39}$
BCP/ 0 h	1.67±0.33	15	$1.81^{+0,20}_{-0,18}$	$5.60^{+3,01}_{-2,04}$
HA/ 336 h	1.01±0.13	12	$1.07^{+0,08}_{-0,08}$	$8.96^{+5,64}_{-3,60}$
TCP/ 336 h	0.09±0.04	14	$0.10^{+0,03}_{-0,02}$	$2.24^{+1,26}_{-0,84}$
BCP/ 336 h	0.50±0.13	15	$0.55^{+0,09}_{-0,08}$	$4.04^{+2,17}_{-1,47}$

*Sample mean is given with 95 % confidence interval of normal distribution

+ Weibull parameters are given with the 95 % confidence interval of Weibull distribution

This phase dissolved completely during first two day of degradation as discussed above. This rapid dissolution was confirmed by XRD measurements (Table 9) and indirectly by the change of the pH of buffer solution (Figure 28). Moreover, characteristic reprecipitation structures, the most probably CDHA, with leaf-like microstructure caused by oversaturation of environment due to α-TCP dissolution was observed on the samples after 2 days of degradation (Figure 31). This reprecipitation is well-known and often observed [111, 246], if α-TCP is presented. The dissolution of α-TCP was finished within first two days of degradation. After this time point no α-TCP phase was detected in the BCP samples. The preferential dissolution of α-TCP phase resulted in rather interesting degradation pattern where whole grain clusters of material fell off ceramic scaffolds resulting in microstructure with significant pit holes pattern all over the surface (Figure 25). We hypothesized that α-TCP was dissolved along grain boundaries. This resulted in loosening

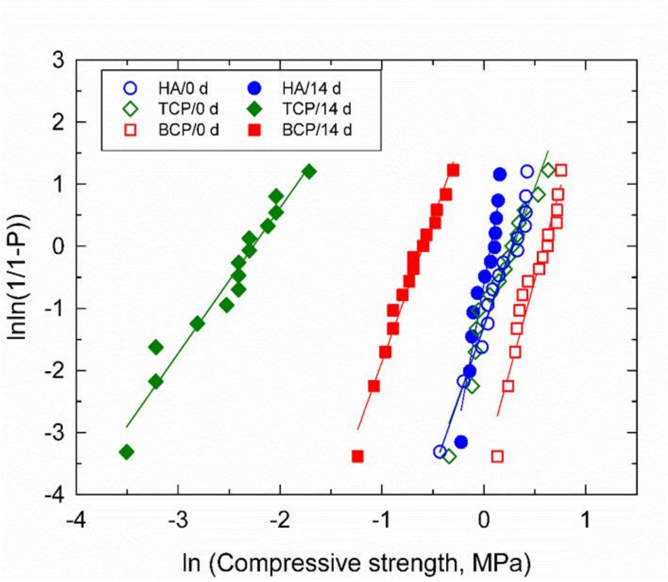

Figure 29 Weibull plots of compressive strength of scaffolds before degradation and after 14 days of degradation.

of HA + β-TCP grain clusters from BCP material at places with higher occurrence of α-TCP. The degradation of α-TCP-free structure of BCP scaffolds was further governed by degradation kinetics of β-TCP as the least stable phase in the microstructure. Due to specific microstructural layout of BCP material, scaffolds exhibited both reasonable strength and structural integrity after 14 days of simulated degradation. Furthermore, the combination of three CaPs phases demonstrated possibility how to control degradation of CaPs structures by the control of microstructural parameters. Combination of α-TCP, HA and β-TCP resulted in ceramic scaffold with hight initial strength and desirable degradation properties with reasonable strength after long term degradation. The degradation properties were governed by α-TCP and β-TCP

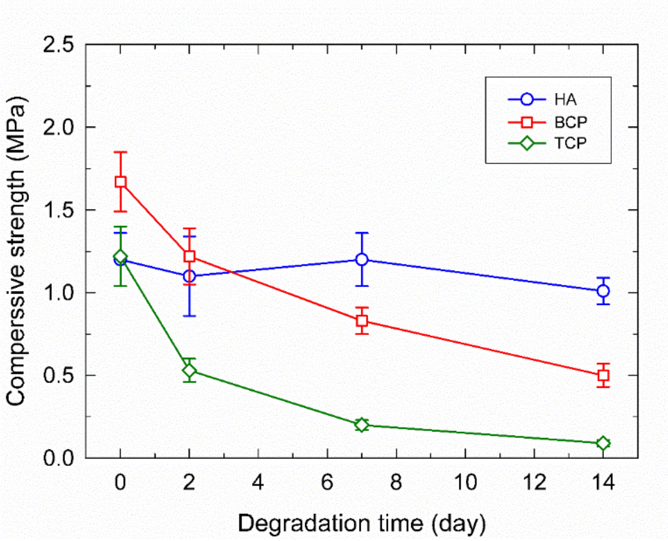

Figure 30 Compressive strength of scaffolds as a function of degradation time. Sample means are given with 95% confidence interval.

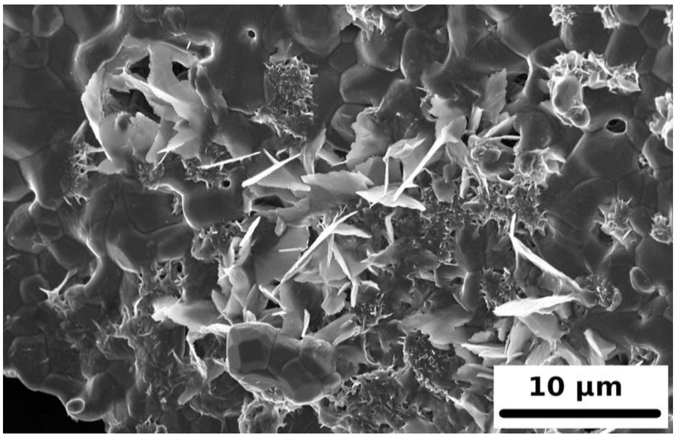

Figure 31 SEM micrographs of a precipitate on the surface of the BCP scaffold after 2 days of degradation in the acidic environment

dissolution and structural integrity of the BCP material was maintained by intrinsic HA scaffolding.

3.3.5 Summary

The effect of the phase composition was studied in simulated *in-vivo* conditions. The beneficial effect of multiphasic composition was described. The samples with the multiphasic composition exhibited a structural evolution resulting in the degradation of the mechanical properties with reasonable mechanical strength even after 14 days. This was the main reason why the multiphasic samples were used as a carrier ceramic material for further development of a hybrid bone scaffold material.

3.4 Phase Composition and Distribution of Individual Phases in Multiphasic Calcium Phosphate Scaffolds

As it was described in previous chapter, not only phase composition but even phase distribution is very important feature governing the degradation of multiphasic calcium phosphate scaffolds. Therefore, it was necessary to describe phase evolution taking place in our system during high temperature treatment and describe differences in phase composition and distribution when initial phase ratio changed. These results provided deep insight in our powder system and enabled us to prepare any phase composition required. Moreover, the knowledge of phase distribution enabled to predict the mechanism of degradation and mechanical response of an implant during wound healing.

3.4.1 Materials and Methods

To describe the evolution of the phase distribution in the scaffolds three types of multiphasic calcium phosphates were produced. The initial HA to TCP powders ratio was 1:4, 1:1 and 4:1. The materials were characterised at a grain level and individual grains were correlated with their phase structure using electron backscatter diffraction method (EBSD). The ceramic suspensions were prepared from HA powder (tri-calcium phosphate extra pure, Riedel de Haen, Germany) and tricalcium phosphate powder (Calcium phosphate, purum p.a. > 96 %, Honeywell, Germany). Suspensions were prepared in the same manner as it has been described in the chapters 3.2.1 and 3.3.1. HA and TCP suspensions were mixed to obtain required powder ratio (HA/TCP=4:1, 1:1, 1:4). The foaming step was omitted and samples were casted into plastic moulds to obtain dense samples. Dried samples were cut to rectangular plates (4 mm x 4 mm x 1 mm). The samples were sintered at 1250 °C for 2 h, the heating rate of 120 °C/min was used. The cooling rate of sintered samples was 10 °C/min, unless mentioned otherwise. The samples were in the state of the closed porosity after sintering. The sintered samples were mechanically ground and polished down to 1 µm diamond paste. Mechanically polished samples were ion polished (LeicaEM TIC3X, Leica, Germany) in order to minimize surface roughness, which was crucial for EBSD analysis. The polished samples had to be conductively coated prior the EBSD analysis. Since the diffraction patterns are created from the very top layer of the sample, even a thin coating of a metal with high atomic number such as Au with a thickness of below 10 nm made the analysis impossible. Therefore, coating was prepared in two-step process. Samples were gold-coated except a small masked area (1 mm x 1 mm). The thickness of a gold coating was 15 nm. The mask was removed after the first step and 5 nm of a fine carbon layer was deposited over the whole surface of the sample in the second step. The thin layer of C in the area of interest (masked area) allowed EBSD mapping analysis of the material. The EBSD analysis was conducted on a scanning electron microscope (SEM) (Verios 460l, FEI, Czech Republic). The SEM was equipped with an EBSD detector (EDAX DigiView IV, EDAX, Germany). The acceleration voltage of the electron beam was set to 25 kV. Beam current was 3.2 nA. The background corrections were calculated from 200 snapshots. Four types of phases were evaluated, previously confirmed by XRD analysis to be presented, namely: HA (ICSD code 87671), α-TCP (ICSD code 923), β-TCP (ICSD code 97500) and $Ca_2P_2O_7$ (ICSD code 14313). Raw datasets were analysed using data analysis software (OIM Analysis^{TM} v8, Edax, Germany). The XRD analysis (Rigaku SmartLab 3kW, Rigaku, Japan) was performed on sintered samples powdered in mortar. Powdered samples were scanned in Bragg-Brentano configuration. Diffraction patterns were collected from 10° to 100° (2θ). Cu Kα radiation was used for XRD analysis. The phase content was quantified using the Rietveld refinement. The sample used for EBSD analysis with (HA/TCP) = 1:4 was thermally etched at 1200°C for 10 min after EBSD scan. The SEM image was acquired from the place corresponding to the site of EBSD analysis to prove that the EBSD grain analysis matched with original grain distribution. A diffraction analysis in transmission electron microscope (TEM) was performed (Titan Themis 60 – 300 cubed, FEI, Czech Republic). A lamella for TEM was prepared from a randomly chosen site on a sintered sample (HA/TCP = 1:1) using SEM microscope equipped with a focused ion beam tubus (Helios 660 NanoLab 660, FEI, Czech Republic).

3.4.2 Results and Discussion

The XRD results are summarized in Table 11. The initial HA/TCP ratios (1:4, 1:1, 4:1) clearly did not correspond with results obtained and tabled in the Table 11. The difference between initial phase ratio and final phase ratio differed due to $Ca_2P_2O_7$ phase which was presented as an impurity in raw TCP powder. The TCP powder consisted of about 11 wt. % of $Ca_2P_2O_7$. Due to $Ca_2P_2O_7$ impurity initial system was not biphasic but triphasic which had resulted from high temperature reaction of HA and $Ca_2P_2O_7$. The reaction of HA and TCP is governed by equation (2) written as:

$$Ca_2P_2O_7 + 2Ca_5(PO_4)_3OH \rightarrow 4Ca_3(PO_4)_2 + H_2O \qquad (2)$$

Knowledge of eq. (2) allowed to calculate final phase composition of the material and, therefore, actively designed the phase composition of sintered scaffolds. The theoretically calculated phase composition according eq. (2) is in Table 11 (values in brackets). The predicted phase composition corresponds very well with experimentally measured phase composition. According to the XRD analysis, the α-TCP phase was presented only in the sample with composition HA/TCP= 1:1. The amount of α-TCP sample was low, estimated as 12 %. Due to low intensity of α-TCP the real value in sample can fluctuate. The occurrence of α-TCP was attributed to the diffusion driven transformation of the α-TCP to the low-temperature β-TCP during cooling from sintering temperature. This hypothesis is supported by the fact that annealing of the sample at a temperature around alpha to beta transition (i.e. at 1150 °C for 2 hrs) resulted to the sample with phase composition of 30 wt. % HA and 70 wt. % of β-TCP without any detectable (by XRD) amount of α-TCP in the ceramic structure. The reason why the α-TCP phase appeared in this sample is not fully understood. The reaction of HA with $Ca_2P_2O_7$ could had started already during heating, starting around 900 °C [240]. We assume that the reaction product at a temperature of 900°C is β-TCP. Although, in the sample with HA/TCP = 1:1 the highest yield of reaction could be expected, mutual contact of reacting phases was lower than in the case of other compositions. Therefore, the reaction described by eq. (2) was probably finished above alpha to beta transition temperature and part of reaction yield was formed as α-TCP and part of this phase was retained

Table 11 Phase composition of sintered multiphase CaP samples determined experimentally by XRD and by theoretical calculations (in brackets).

HA/TCP Initial powder ratio	HA (wt.%)	β-TCP (wt.%)	α-TCP (wt.%)	$Ca_2P_2O_7$ (wt.%)
1:4	0(0)	97(96)	0(0)	3(4)
1:1	24(28)	64(72)	12(0)	0(0)
1:1*	30(28)	70(72)	0(0)	0(0)
4:1	73(71)	27(29)	0(0)	0(0)

*Annealed at 1150°C for 2 h after sintering at 1250°C for 2 h

Values in bracket are calculated according to eq.2

during a cooling as explained in the previous text. Unfortunately, the theory mentioned was not fully validated, but according to our best knowledge it was most probable scenario. To confirm XRD results, the phase composition of the sample with HA/TCP = 1:1 was analysed by TEM (Figure 32). The TEM analysis confirmed presence of HA and β-TCP in the lamella. HA grains were considerably smaller than β-TCP. The smaller size of HA grains can be explained by granulometry of HA powder used (130 nm in suspension) which is considerably smaller than TCP powder (1 µm in the suspension). The α-TCP detected by XRD was not found in the form of a regular uniaxial grains. As highlighted in the Figure 32, areas with different contrast were detected by TEM, occurring as a thin envelope of mainly β-TCP phase. We tried to acquire diffraction pattern from those areas unsuccesfully. Their exact origin was not found out, but we assume, that these areas are in fact low symmetry crystalic structure very close with properties and crystal parameters to the α-TCP phase. These results were in a good agreement with degradation experiments, where the typical patterns of α-TCP dissolution and reprecipitation were found. Moreover, the mechanism of degradation correlated with α-TCP phase distributed mainly along grain boundaries, which was confirmed by subsequential EBSD analysis. To validate the accuracy of CaP grain detection by EBSD method the crystal structure of the sample of HA/TCP = 4:1 was scanned. The sample was subsequentially thermally etched and grain structure of the area corresponding to the area of interest during EBSD scanning were compared (Figure 33). The SEM image of the area of interest clearly confirmed the same grain distribution as detected by EBSD

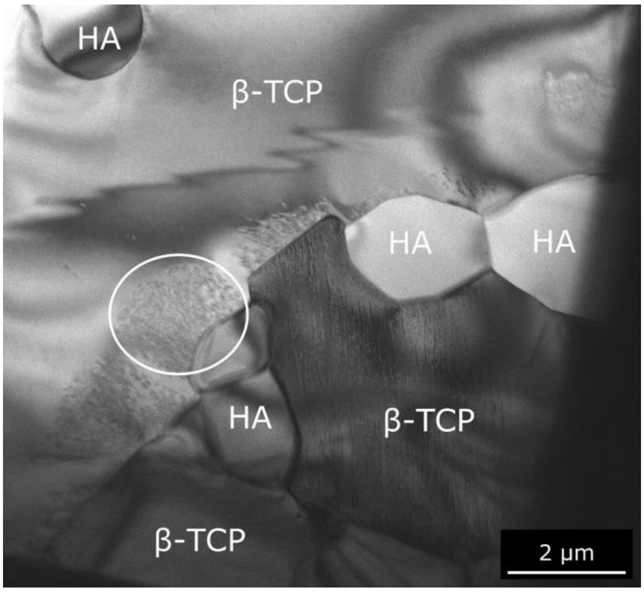

Figure 32 TEM analysis of HA/TCP = 1:1 with phase identification of individual grains. White circle marks the area with different contrast which was attributed to the occurrence of α-TCP

analysis. Specific shapes and orientation of grains and pores could be directly correlated with SEM image. The Figure 33 b shows as-scanned inverse pole figure map (IPF). Individual colours represent individual grain orientations, defining the grain itself. Majority of orientation detected were poorly indexed, which can be visible from the scan quality resulting in rather speckled image. The standard crystallographic triangles were omitted for the sake of clarity since the information of the exact crystal orientation was not crucial. In our case, the IPF were used just to highlight the shape of individual grains. The quality of raw scan was artificially enhanced by OIM Data analysis software. The grain dilatation procedure was applied, grain boundaries were defined as areas with a misoriented angle greater than 5°and each grain had to consist at least of 20 pixels in multiple rows. The image noise was significantly reduced (Figure 33 c) by this post processing but original distribution of detected grains was retained. The same procedure of data processing was applied in the study of phase distribution in the following text. Since the correlation of thermally etched microstructure matched the EBSD phase mapping, the thermal etching in the case of other samples was omitted. The phase distribution of the samples was successfully described by the EBSD. The results revealed phase distribution on a grain level. Summary of the phase analysis is in the Figure 34. The first column represents IPFs of the area of interest, representing a grain structure of the samples. The second column represents phase distribution of individual phases. Phases are colour coded and red colour represents α-TCP, yellow represents β-TCP, HA is represented by green colour and finally $Ca_2P_2O_7$ is coloured in blue. The phase composition derived from the EBSD scan agreed with phase composition detected by the XRD. The correlation of the grain structure with the phase identification improved our knowledge of the microstructure from application-based point of view. In the case of HA/TCP = 1:4 no HA was detected in the microstructure which is in full agreement with theory and XRD analysis. Just a negligible amount of $Ca_2P_2O_7$ was detected in a form of small grains. Calculated amount of $Ca_2P_2O_7$ phase should reach 4 wt.% (3 wt.% measured by XRD). It is unclear

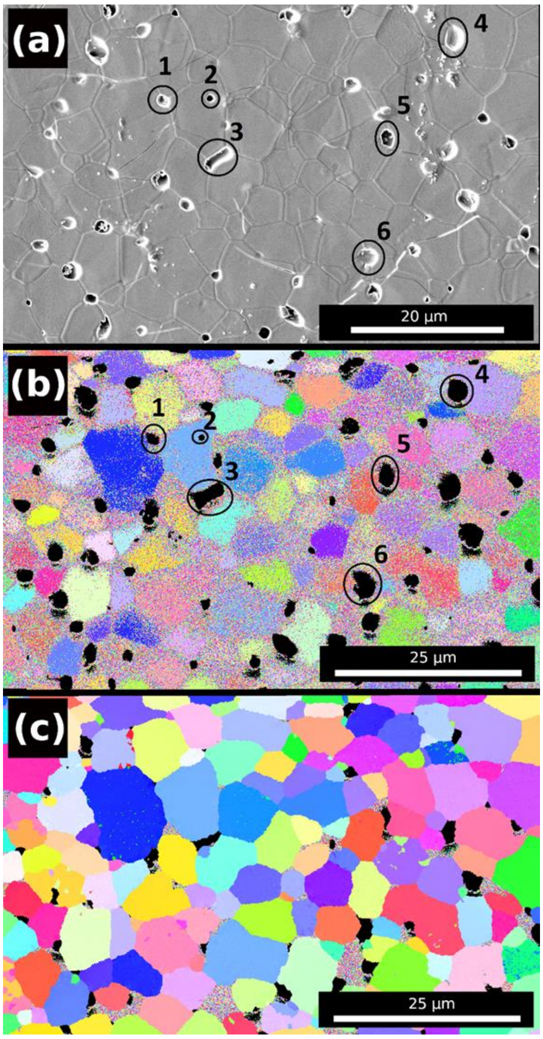

Figure 33 (a) thermally etched SEM microstructure with marked microstructural orientation points, (b) raw EBSD scan of inverse pole figures (representing individual grains) with microstructural orientation points marked, (c) processed EBSD inverse pole figures

whether $Ca_2P_2O_7$ phase creates even bigger grains in microstructure. If so, these were not detected by EBSD scan, the most probably due to their low occurrence. An analysis of the sample with HA/TCP = 1:1 revealed rather intriguing microstructure composed of three phases (HA, β-TCP and α-TCP). The monoclinic α-TCP phase was located along grain boundaries. There is some level of uncertainty, because part of pixels indexed as α-TCP could be misindexed points due to low symmetry of grain boundaries. But broad analysis of the sample agreed on some α-TCP phase being presented in microstructure. Since no other morphology of α-TCP phase except this along grain boundaries was detected both by TEM and EBSD method, we can conclude, that α-TCP was located along grain boundaries rather than in the form of individual grains. The phase composition of the sample with the highest HA/TCP ratio 4:1 revealed the composition of HA and β-TCP grains with β-TCP in the form of the uniaxial grains and some thin layers enveloping HA grains. The β-TCP network is believed to be caused by solid state reaction of HA and $Ca_2P_2O_7$. The distribution of different phases also affected the grain size in the sintered ceramics. The well-

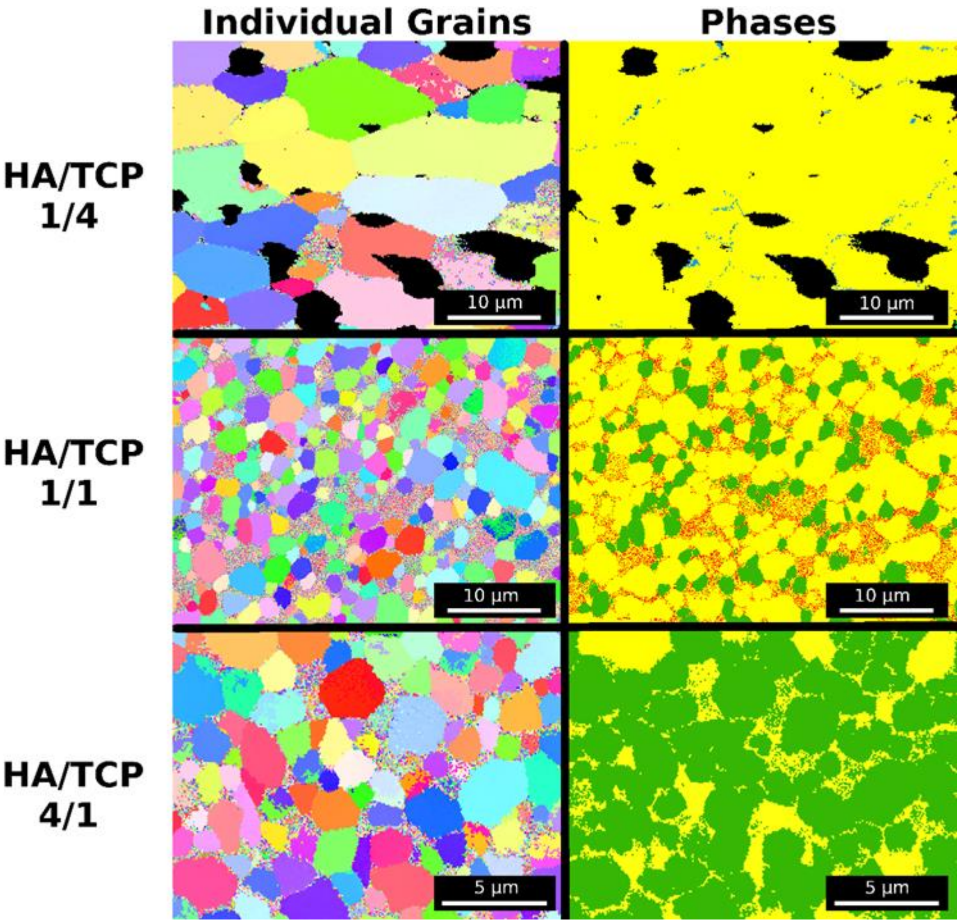

Figure 34 Grain and phase analysis of sintered samples with different HA/TCP ratio. The first column represents individual grains (marked in different colours). The second column represent phase distribution in the samples, colour coding of the phases: yellow colour – β-TCP, blue colour - Ca2P2O7, green colour – HA, red colour – α-TCP

known fact is, that homogenous dispersion of a second phase can prevent grain growth during sintering. This was the case of the sample with HA/TCP = 4:1 and 1:1. In these samples the small HA particles were homogeneously mixed with large TCP particles and mixture of these phases effectively prevented the grain growth of both phases. If we look at the sample with HA/TCP = 1:4 that the HA phase was fully consumed by the proposed high temperature reaction. There was only a limited barrier to the grain growth of remaining TCP grains since all HA was consumed during high temperature reaction resulting in a much coarser microstructure.

3.4.3 Summary

The in-depth study on a phase structure in multiphasic calcium phosphate systems was performed. The results suggested the importance of a heat treatment and initial phase composition on a final phase composition of samples. The phase composition and distribution are directly related to the biological response. Knowledge of the behaviour of the multiphasic systems can, therefore, help to design an appropriate phase structure of the scaffolds and introduces other level of customization.

3.5 In-Vitro Performance of Ceramic Scaffolds

In order to choose the best ceramic carrier possible HA, TCP and BCP (HA/TCP = 1:1) ceramic foams were tested *in-vitro* and their performance was mutually compared. The composition with the best biological response was then utilized in the *in-vivo* study.

3.5.1 Scaffolds Preparation

The HA, TCP and BCP samples prepared in the chapter 3.3 were used. The porous structure and porosity of the samples are described in the Table 8. Samples were produced in the form of round ceramic scaffolds with a diameter of 9 mm and a height of 4 mm after sintering. Sintering temperature was 1250°C for 2 hrs in order to correlate in-vitro test with the results obtained during the simulated degradation. The sintered samples were placed in 48-well plates and seeded with $30\text{x}10^3$ human bone marrow-derived mesenchymal stem cells (hMSCs) (ScienCell, USA) per well. Scaffolds with seeded cells were cultured in 700 µl of a growth medium (α-MEM supplemented with 10 % fetal bovine serum and 1 % Penicillin/Streptomycin, Gibco, UK) in an incubator with 5 % CO_2 at 37°C. One half of the culture medium was changed on a day 7. To determine the metabolic activity of hMSCs seeded on the scaffolds, the MTS assay (CellTiter96® AQueous One Solution Cell Proliferation Assay, Promega, USA) was used. The scaffolds were transferred into new wells to prevent the cells tissue culture to adhered to the plastic to misrepresent the measured data. Subsequently, 400 µL of fresh media and 80 µL of the MTS substrate were added to each well. After 2-hour incubation at 37°C, 100 µL of the culture solution was transferred to a new clean well. The absorbance of the media was detected at 490 nm using a microplate reader (Infinite® M200 PRO; Tecan, Switzerland). The adhesion and proliferation of the cells on the scaffolds was determined using a Quant-iT dsDNA Assay Kit (Thermo Fisher Scientific, USA) from the amount of DNA. The scaffolds were put into a vial with 500 µL of cell lysis solution (0.2% v/v Triton X-100, 10 mM Tris (pH 7.0), and 1 mM EDTA) and processed through 3 freeze/thaw cycles. Between each freeze/thaw cycle, the scaffolds were roughly vortexed. A sample (10 µL) was mixed with 200 µL of reagent solution and fluorescence intensity was detected using a multiplate fluorescence reader (Infinite M200 PRO, Tecan, Switzerland; λex= 485 nm, λem= 525 nm). The DNA content was determined according to the calibration curve using the standards in the kit. The tests for the cell metabolic activity and the proliferation were always performed on the same scaffold. Quantitative data of the cell metabolic activity and proliferation are presented as mean values, which were determined from at least 5 independently prepared samples. DiOC6(3) (3,3'-diethyloxacarbocyanine iodide; Invitrogen, Molecular Probes) staining was used to detect cell adhesion on the scaffolds. The samples were fixed with frozen methyl alcohol (-20°C) for 10 min and rinsed with phosphate buffered saline (PBS; pH 7.4). A fluorescent probe DiOC6(3) at a concentration of 1 $\mu g\ mL^{-1}$ in PBS was added and incubated with the samples for 30 min at room temperature. Subsequently, the samples were rinsed with PBS, and propidium iodide (Sigma Aldrich, USA) at concentration of 5 $\mu g\ mL^{-1}$ in PBS was added for 5 min., followed by rinsing with PBS. The samples were visualized using a confocal microscope (LSM 5 DUO, Carl-Zeiss MicroImigining, Germany). λ_{ex} = 488 and 560 nm and λ_{em} = 520 and 580 nm was used for DiOC6(3) and propidium iodide detection, respectively. The hMSC's morphology was evaluated by SEM (Tescan Vega 3, Brno, Czech Republic) on days 1 and 7. Scaffolds with hMSCs were washed in PBS and fixed in 2.5% glutaraldehyde for 2 hours at 4°C. Then the samples were dehydrated in ethanol. To dry the scaffolds hexamethyldisilazane (Sigma-Aldrich) was added.

3.5.2 Results and Discussion

To test the biocompatibility of the ceramic scaffolds the adhesion and the proliferation analysis as well as the metabolic activity of seeded mesenchymal stem cells were tested and evaluated on days 1, 3, 7 and 14. The DNA content referred to the amount of hMSCs adhered on the scaffolds. The data showed (Figure 35) that the number of cells was comparable for all scaffolds during the first week of the experiment. Subsequently, there was the most significant increase in the number of cells on the BCP sample. Data from the first day showed that on the day 1, statistically less cells were seeded on the BCP sample. But after 14 days the amount of DNA detected was the highest just on BCP sample. That suggested rapid proliferation of the cells on the surface of BCP material. Metabolic activity on TCP and BCP samples increased gradually over the 14-day of testing period (Figure 36). The BCP sample showed statistically the highest metabolic activity since the day 3 and the last day of the test metabolic activity on BCP sample was approximately two times higher than on HA and TCP samples. This suggest the effect of α-TCP on metabolic activity, since the α-TCP was proven to dissolute within the first few days releasing calcium and phosphate ions to the environment, even though this is little contradictory to the results obtained in the work of Tamai and et. al. [247]. In this work α-TCP was found cytotoxic. According to the authors explanation phosphoric acid generated during α-TCP hydrolysis was responsible for the cytotoxicity.

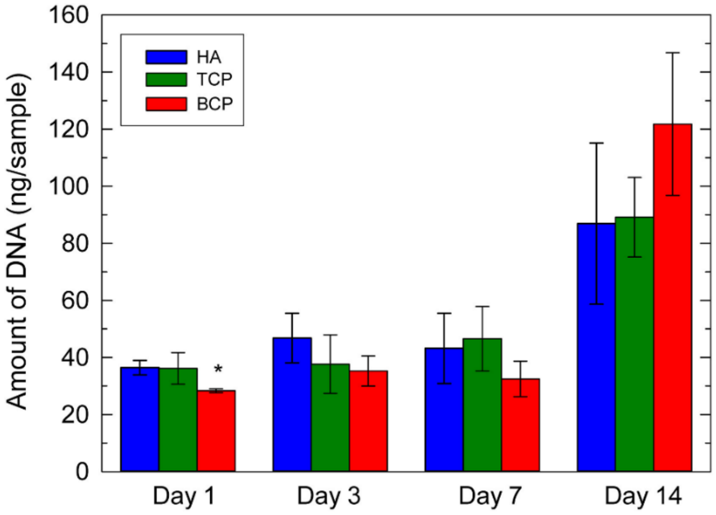

*Figure 35 Number of adhered cells on scaffolds quantified as an amount of DNA in dependence on culture time. The errors bars give standard deviation and statistical significance is shown above the columns (*p < 0.05)*

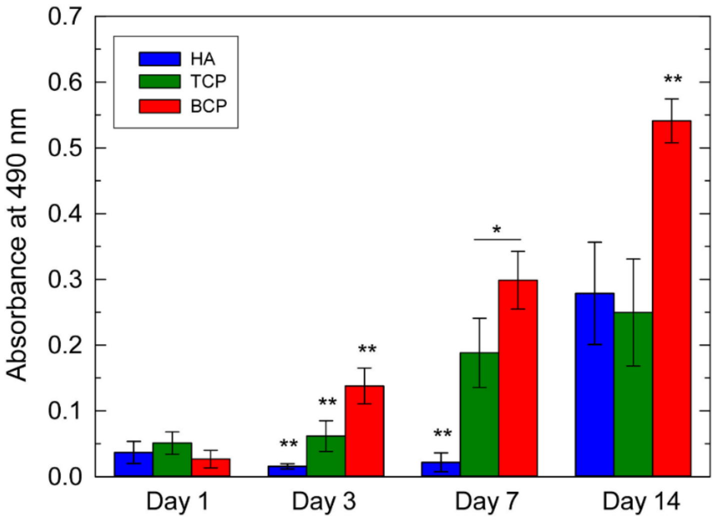

*Figure 36 Metabolic activity of cells adhered on scaffolds derived from MTS assay in dependence on culture time. The errors bars give standard deviation and statistical significance is shown above the columns (*p < 0.05; **p < 0.01).*

The main difference is just limited amount of α-TCP in our sample. So, we assume, that low concentration of α-TCP is beneficial as proven by other authors [248]. For the HA sample, the metabolic activity was at the same level for the first week. Subsequently, on day 14 an increase in metabolic activity was observed and metabolic activity of HA was comparable to TCP sample. Unfortunately, we cannot plausibly explain that increase in the metabolic activity. Confocal microscopy and scanning electron microscopy were used to analyze the cell spreading and their morphology. The cells adhered to all scaffolds and over the period of 14 days covered the surface of the scaffolds (Figure 37). The highest increase in the number of the cells was observed on BCP scaffold, which is in a good agreement with the measurements of DNA content. SEM revealed that the cells on the HA scaffold remained spindle-shaped morphology after 7 days while on the BCP and TCP scaffolds were cells flat like and widely spread in a form of confluent layers (Figure 38). This result agrees with low DNA amount detected on the HA sample, signalizing that HA structure was not convenient for early-stage cell proliferation. This behavior changed rapidly after the day 7 (Figure 35, Figure 38). All the *in-vitro* tests of adhesion, proliferation and viability showed the best cell response to the BCP scaffold. It is difficult to identify the most important parameter responsible for the different cell response to the tested scaffolds. The main differences were found in the phase composition and ionic concentration in the cell environment. This is directly connected with phase composition of ceramic scaffolds and their dissolution properties.

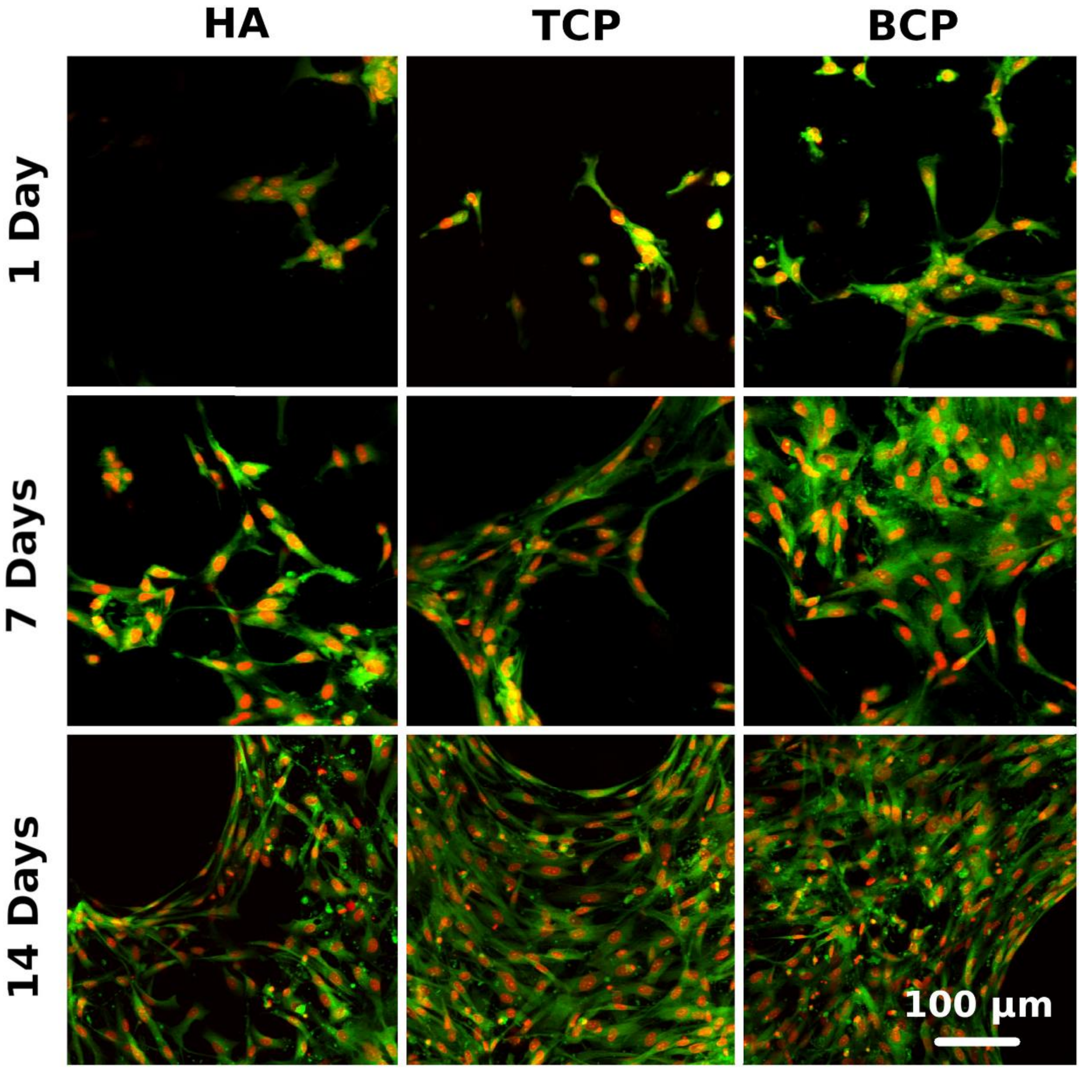

Figure 37 Visualization of cell adhesion and distribution on scaffolds using a confocal microscope. Cell nuclei were stained in red and cell internal membranes in green.

Another parameter affecting the cell response could be surface morphology that changed with different grain size of the scaffold ceramics and could evolve in time due to preferable dissolution of TCP phases. Rapid change in surface properties were reported in the case of BCP, where dissolution of α-TCP left surface rough with many pit holes which could serve as anchoring points for spreading cells. It seems that highly soluble α-TCP embedded in a less soluble matrix (β-TCP/HA) brings biological advantages and at the same time prevents undesirable instability and dissolution-precipitation issues reported with pure α-TCP scaffolds [14, 246, 247].

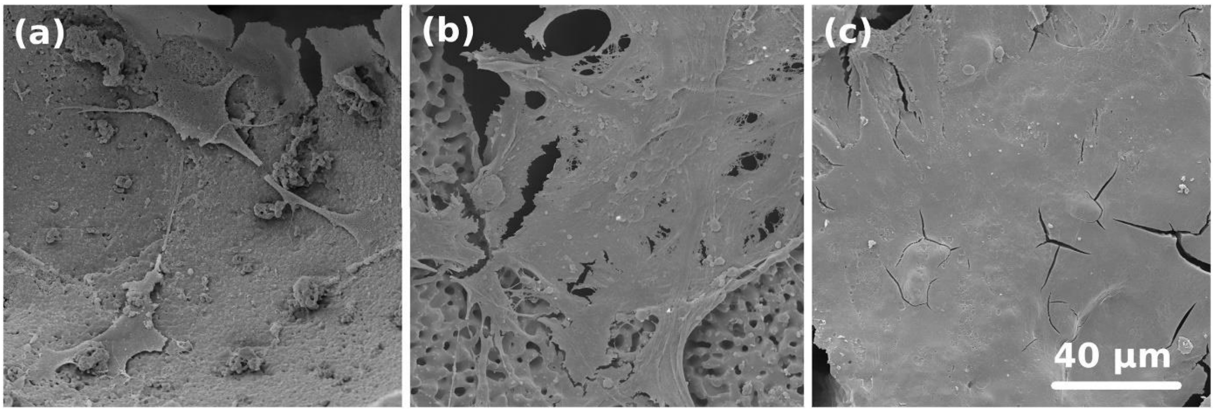

Figure 38 Morphologies of attached cells on the scaffolds visualized using scanning electron microscopy on day 7, sample HA (a), TCP (b), and BCP (c)

3.5.3 Summary

The *in-vitro* tests revealed outstanding *in-vitro* performance of the BCP scaffolds. Therefore, BCP scaffolds with HA/TCP = 1/1 were chosen as the ceramic material for hybrid bone scaffolds used for *in-vivo* tests.

3.6 In-Vivo Evaluation of Hybrid Bioceramic Scaffolds for Spinal Fusion

The BCP porous ceramic material sintered at 1250 °C with phase composition described in Table 9 was used for production of the hybrid bone scaffolds.

Let´s summarize the main reasons for this decision:

1. Gradual dissolution of BCP ceramic under the environment simulating the osteoclastic activity with a sufficient structural integrity and strength even after 14 days of degradation test (chapter 3.3). This is in very good agreement with demands put on resorbable structures [14].
2. The phase composition of BCP contains of both the most stable CaPs phase, HA, providing structural integrity and the strength of scaffold and TCP phases ensuring biodegradability. The β-TCP phase guarantees the long term degradation properties of scaffolds and α-TCP phase is believed to improve a bone proliferation during early stages of a healing (chapters 3.3, 3.4 and 3.5).
3. The cellular response to the material was clearly the best of all ceramic carriers tested (chapter 3.5)

The main task of following text is to show a comparison of the gold standard - autografts with the newly developed artificial material on *in-vivo* model. Moreover, *in-vivo* tests are final stage of the doctoral research on a development, production and incorporation of new material for a bone healing. This last chapter shows the force of multidisciplinary approach where a close collaboration of living and non-sciences come together and create the brand new carefully designed material which could help to improve life standards.

3.6.1 Scaffolds Preparation

The hybrid biodegradable ceramic/biopolymer implant was prepared in two steps. The first step was preparation of the porous ceramic material which served as a carrier for biopolymeric filling. The ceramic material was produced as a mixture of HA/TCP = 1/1. Preparation route has been already described in previous chapter 3.3.1. The phase composition of the sintered ceramic material is given in Table 9. The microstructural description is in Table 8. Dried foam was machined, and final sintered ceramic implants had dimensions of 25 mm x 15 mm x 3.3 mm. The sintered ceramic scaffolds were subsequently impregnated with biopolymer fibres based on bovine collagen and calcium salt of oxidized cellulose (oxycellulose) [69]. Collagen slurry mixed with oxycellulose in a ratio of 1:1 (giving total concentration of 0.5 wt. %) was administered into the ceramic foam, crosslinked and modified with FGF-2stab (Enantis, Ltd. Brno, Czech Republic) in the amount of 0.1 µg of protein per 1 cm^2. The final hybrid structure consisted of ceramic carrier filled with freeze-dried fine polymeric sponge with embedded factors accelerating a bone growth. The samples were sterilized using ethylene oxide and the sterile samples were used for surgeries. The lumbar fusion was performed on male piglets (Sus scrofa domesticus), 4-month-old with a weight around 40 kg. The piglets were used since biological evaluation of pig spine shows comparable features with human spine. Twenty-four piglets were used for *in-vivo* tests in total. Group of 24 piglets was divided into two subgroups. Both subgroups consisted of 12 piglets. The groups were lablled A and B. Group A underwent lumbar interbody fusion (L2/L3) with the autograft implant harvested from iliac crest. Group B underwent lumbar interbody fusion (L2/L3) with the newly developed hybrid bone graft material. Both group A and B were divided into two subgroups referred as A1, A2 and B1, B2, respectively. The animals from group A1 and B1 were sacrificed 8 weeks after the surgery and their spines were extracted whereas animals from group A2 and B2 were sacrificed after 16 weeks. The Extracted spines were CT scanned, biomechanically and histologically tested. The interbody fusion of individual spines between L2/L3 segments was evaluated. The implantation site was stabilized by titanium plates and screws to minimize any movements of site during healing. The spines after 8 and 16 weeks were extracted en-block (T15 – L6). The spines were used for biomechanical testing. The MTS mini Bionics (MTS, USA) was used to carry out biomechanical evaluation of a spinal behaviour and stability after intervertebral fusion. As a reference material the physiologically native spines were used. Tests were performed on 4 specimens of A1 and A2 subgroups and on 4 specimens of B1 and B2 subgroups and on 7 specimens of native spines (N). Non-destructive flexibility testing of specimens was performed during which pure moments with a load limit 5 Nm at a displacement rate 20 °per min was applied. Besides non-destructive testing, ultimate flexural strength of the same specimens was evaluated. The non-destructive CT measurement were made in order to describe 3D profile of unification on implant site. The micro CT system GE phoenix v|tome|x L 240 (GE Sensing & Inspection Technologies GmbH, Germany) equipped with Nanofocus180 kV/15 W X-ray tube and flat panel detector DXR 250 was used for the tomographic measurement. The fusion quality was evaluated.

3.6.2 Results and Discussion

The comparison of the autograft implant and artificial hybrid bone scaffold is in the Figure 39 (a). If we compare the surgeries utilizing the autologous bone graft harvested from iliac crest and artificial bone implant, we can conclude that surgical time in the case of artificial implant was significantly reduced. Moreover, the second operation site related to the bone graft harvesting was reduced diminishing the danger of a donor site morbidity and related problems. There was no problem related to the shape and dimensions of pre-prepared, sterile, artificial bone graft material. Handling strength of the artificial bone graft material was sufficient. Needless to say, that due to low thickness and porous structure it was necessary to handle material cautiously in order to avoid any damage prior implantation. Special implantation device had been invented prior surgeries to implant material safely (Figure 39 (b)). Due to a robust construction of the implantation device it was possible to apply high mechanical loading on the material during implantation without any damage made on implant itself. Postoperatively, just one animal was reported paraplegic, sacrificed, and excluded from study. No other general problems related to the postoperative complications were observed. It was reported that 3 animals from A1 subgroup had discrete screw loosening and 4 animals from A2 subgroup had completely loosened titanium stabilization structures. In these cases, implant migration from implantation site occurred. Subgroups Bs were reported with 2 cases of discrete screw loosening. The A group was characterised with huge fibrous reaction at spine fusion site and in two cases purulent collection took place, whereas group B was reported with osseous overgrowth of intervertebral space (Figure 40).

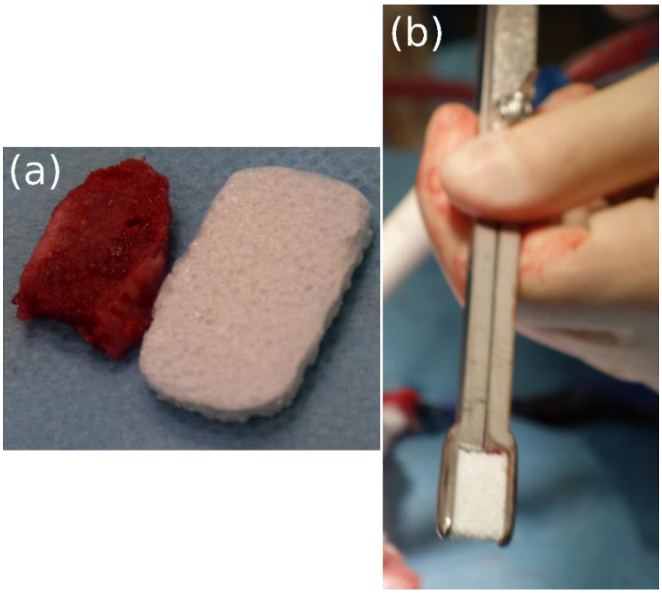

Figure 39 (a) comparison of autograft (left) and artificial hybrid scaffold (right), (b) implant in the implantation device, implant dimensions 25 mm x 15 mm x 3.3 mm

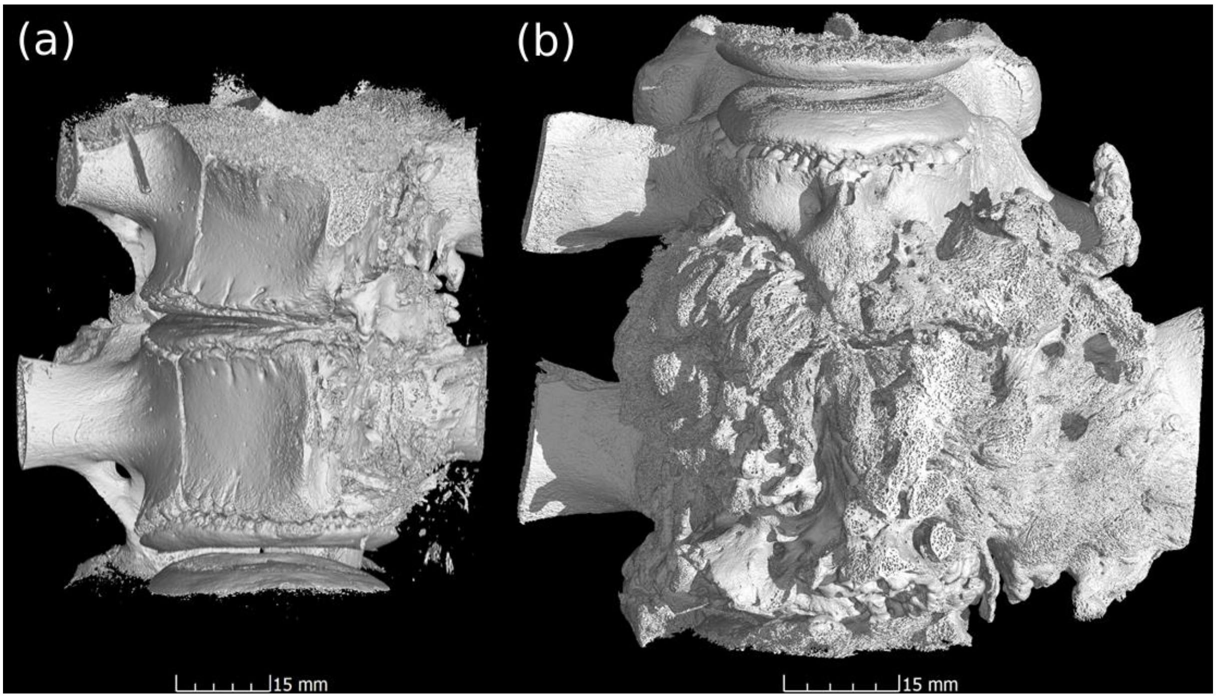

Figure 40 CT scan of treated site after 16 weeks after implantation, (a) novel hybrid material, (b) bone autograft, huge fibrous reaction is obvious

Biomechanical properties were tested on the extracted spine blocks. After 8 weeks there was no statistical difference in stiffness of spines harvested from A1 and B1 subgroups (Figure 41). Significant change occurred after 16 weeks where specimens extracted from B2 subgroup were reported with statistically significantly higher stiffness than specimens extracted from A2 subgroup. The higher stiffness suggests better fusion of L2/L3 block treated with artificial hybrid bone graft material than in the case of autologous bone grafts. This was supported by histological analysis of spines where osseous overgrowth was described. No unwanted reaction was observed in the case of artificial hybrid bone graft material and certain level of fusion, significantly higher than in the case of autograft material, was reached after 16 weeks after surgery (Figure 40 (a)). These preliminary results suggest an outstanding potential of newly developed artificial porous hybrid bone material based on porous multiphasic calcium phosphate carrier material combined with biopolymeric material with embedded factors accelerating bone growth.

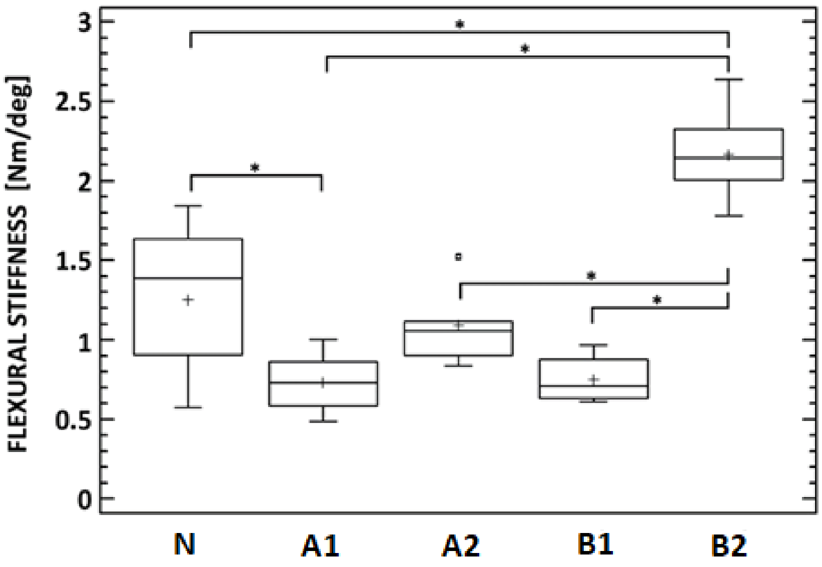

*Figure 41 Flexural stiffness of native lumbar spine cadavers (N), Specimens A1 and B1 measured after 8 weeks after surgery, specimens A2 and B2 measured after 16 weeks after surgery. * denotes statistically significant differences*

3.6.3 Summary

The biodegradable hybrid bone scaffold was tested *in-vivo* and compared with the gold standard grafting material – the autologous bone graft. Results suggested that the hybrid bone scaffold overcame autologous bone graft in the healing process and final quality of the bone fusion.

4 Conclusions

The doctoral thesis combines the latest theoretical knowledge about calcium phosphate ceramics used for bone regeneration with the experimental part in which the new material for a bone regeneration was investigated. The theoretical part of this work focused on calcium phosphate ceramic materials, their interaction with a living organism and challenges connected with their usage. The ideal scaffold has been defined in this part and its approximation to real materials has been made. The current state of the art in the field of commercially available materials has been introduced, giving an idea about calcium phosphate ceramics currently supplied and used. The knowledge having been acquired in this section helped to define the main goals of doctoral thesis. The main goal was to prepare calcium phosphate-based material for bone regeneration with properties at least the same or even better as the current gold-standard material, the autograft. The research part focused on ceramic processing feasible for preparation of a large volume of ceramic foams serving as stock-pile material for further implant customization. Moreover, internal structure of the ceramic foams had to meet quite strict criteria making them suitable for a bone regeneration. The concept of implant customization was tested on hydroxyapatite foams. The novel process of epoxy-based gelcasting has been introduced. This method overcame restriction of standard gelcasting methods. The novel system based on polymerization of epoxy monomers is not affected by oxygen and the whole process of ceramic foam preparation can be carry out under normal laboratory conditions. The process of foam production was optimised. As the result, reliable and simple method of ceramic foam processing has been developed. Subsequently, novel gelcasting method was utilized for processing of different types of calcium phosphate foams. The foams differed in phase composition. To evaluate the biodegradation properties of the materials the test simulating *in-vivo* degradation was conducted. The results allowed to directly compare three types of scaffolds – pure HA, pure TCP and multiphasic scaffold consisting of α and β TCP phases and HA. Only multiphasic composition combined both biodegradable properties and reasonable strength after a long-time exposure. The mechanical response was correlated with phase distribution on grain level. According to our best knowledge we reported on a distribution of calcium phosphate phases for the first time utilizing very powerful method of electron backscatter diffraction (EBSD). Data acquired allowed us to explain rather interesting degradation behavior of multiphasic calcium phosphate ceramics. The high temperature reaction leading to discrepancy between the initial phase ratio and the final phase ratio after sintering was described and the influence of calcium pyrophosphate impurities on final phase composition was explained. Furthermore, *in-vitro* tests targeting on biological properties indicated, that the multiphasic composition positively contributed not only to degradation of the scaffold in *in-vivo* like conditions but even enhanced bone marrow stem cell maturation and proliferation. Carefully chosen and tested porous sintered multiphasic calcium phosphate material was used as ceramic carrier for preparation of the hybrid bone scaffolds for *in-vivo* study of a lumbar interbody fusion and compared with an autologous bone graft harvested from iliac crest. The preliminary results suggested that the artificial material overcame standard autologous graft in all aspects. This result is the highlight of the whole work and is an astounding example how multidisciplinary approach, careful material selection and pre-clinical testing can result in the brand-new material with outstanding biological properties.

5 Published Articles Related to the Topic of Doctoral Thesis

P. Stastny, Z. Chlup, D. Kalasova, T. Zikmund, J. Kaiser, M. Trunec, Epoxy-based gelcasting of machinable hydroxyapatite foams for medical applications, J Am Ceram Soc, 101 (2018) 3317-3327.

P. Stastny, R. Sedlacek, T. Suchy, V. Lukasova, M. Rampichova, M. Trunec, Structure degradation and strength changes of sintered calcium phosphate bone scaffolds with different phase structures during simulated biodegradation in vitro, Mat Sci Eng C-Mater, 100 (2019) 544-553.

P. Stastny, P. Vacek, M. Trunec, Characterization of microstructure and phase distribution of sintered multiphasic calcium phosphate bioceramics, Ceram Int, (2019) 5500-5504.

6 References

[1] V.S. Gshalaev, Hydroxyapatite: Synthesis, Properties and Application, Nova Science Publishers, New York, 2012.

[2] R. Florencio-Silva, G.R.D. Sasso, E. Sasso-Cerri, M.J. Simoes, P.S. Cerri, Biology of Bone Tissue: Structure, Function, and Factors That Influence Bone Cells, Biomed Res Int, (2015).

[3] S.V. Dorozhkin, Calcium orthophosphate bioceramics, Ceram Int, 41 (2015) 13913-13966.

[4] L.Y. Chen, X.D. Yan, L.L. Tan, B.W. Zheng, F.K. Muhammed, K. Yang, Y. Liu, In vitro and in vivo characterization of novel calcium phosphate and magnesium (CaP-Mg) bilayer coated titanium for implantation, Surf Coat Tech, 374 (2019) 784-796.

[5] C. Hu, D. Ashok, D.R. Nisbet, V. Gautam, Bioinspired surface modification of orthopedic implants for bone tissue engineering, Biomaterials, 219 (2019).

[6] M. Navarro, A. Michiardi, O. Castano, J.A. Planell, Biomaterials in orthopaedics, J R Soc Interface, 5 (2008) 1137-1158.

[7] C. Pierre, G. Bertrand, C. Rey, O. Benhamou, C. Combes, Calcium phosphate coatings elaborated by the soaking process on titanium dental implants: Surface preparation, processing and physical-chemical characterization, Dent Mater, 35 (2019) E25-E35.

[8] E. Vidal, J. Buxadera-Palomero, C. Pierre, J.M. Manero, M.P. Ginebra, S. Cazalbou, C. Combes, E. Ruperez, D. Rodriguez, Single-step pulsed electrodeposition of calcium phosphate coatings on titanium for drug delivery, Surf Coat Tech, 358 (2019) 266-275.

[9] L. Xie, H.Y. Yu, Y. Deng, W.Z. Yang, L. Liao, Q. Long, Preparation, characterization and in vitro dissolution behavior of porous biphasic alpha/beta-tricalcium phosphate bioceramics, Mat Sci Eng C-Mater, 59 (2016) 1007-1015.

[10] P. Stastny, Z. Chlup, D. Kalasova, T. Zikmund, J. Kaiser, M. Trunec, Epoxy-based gelcasting of machinable hydroxyapatite foams for medical applications, J Am Ceram Soc, 101 (2018) 3317-3327.

[11] R.X. Shao, R.F. Quan, L. Zhang, X.C. Wei, D.S. Yang, S.J. Xie, Porous hydroxyapatite bioceramics in bone tissue engineering: current uses and perspectives, J Ceram Soc Jpn, 123 (2015) 17-20.

[12] R.G. Ribas, V.M. Schatkoski, T.L.D. Montanheiro, B.R.C. de Menezes, C. Stegemann, D.M.G. Leite, G.P. Thim, Current advances in bone tissue engineering concerning ceramic and bioglass scaffolds: A review, Ceram Int, 45 (2019) 21051-21061.

[13] S.V. Dorozhkin, Multiphasic calcium orthophosphate (CaPO4) bioceramics and their biomedical applications, Ceram Int, 42 (2016) 6529-6554.

[14] S.V. Dorozhkin, Biphasic, triphasic and multiphasic calcium orthophosphates, Acta Biomater, 8 (2012) 963-977.

[15] S.V. Dorozhkin, Calcium Orthophosphate Cements and Concretes, Materials, 2 (2009) 221-291.

[16] S.K.L. Levengood, S.J. Polak, M.J. Poellmann, D.J. Hoelzle, A.J. Maki, S.G. Clark, M.B. Wheeler, A.J.W. Johnson, The effect of BMP-2 on micro- and macroscale osteointegration of biphasic calcium phosphate scaffolds with multiscale porosity, Acta Biomater, 6 (2010) 3283-3291.

[17] P. Stastny, R. Sedlacek, T. Suchy, V. Lukasova, M. Rampichova, M. Trunec, Structure degradation and strength changes of sintered calcium phosphate bone scaffolds with different phase structures during simulated biodegradation in vitro, Mat Sci Eng C-Mater, 100 (2019) 544-553.

[18] Y.L. Ma, H.L. Dai, X.L. Huang, Y.P. Long, 3D printing of bioglass-reinforced beta-TCP porous bioceramic scaffolds, J Mater Sci, 54 (2019) 10437-10446.

[19] S.V. Dorozhkin, A detailed history of calcium orthophosphates from 1770s till 1950, Mat Sci Eng C-Mater, 33 (2013) 3085-3110.

[20] E. J.C., Structure and Chemistry of the Apatites and Other Calcium Phosphates, Elsevier Science B.V.1994.

[21] I.V. Antoniac, Handbook of Bioceramics and Biocomposites, Springer-Verlag GmbH.

[22] E.R. Kreidler, F.A. Hummel, Phase Relationships in System Sro-P2o5 and Influence of Water Vapor on Formation of Sr4p2o9, Inorg Chem, 6 (1967) 884-&.

[23] H.C.W. Skinner, Studies in Basic Mineralizing System, Cao-P2o5-H2o, Calc Tiss Res, 14 (1974) 3-14.

[24] V.R. Thakker, P.W. Whyte, T. Igarashi, Genetics of Bone Biology and Skeletal Disease, Second Edition ed., Academic Press2017.

[25] J. Bilezikian, J.T. Martin, T. Clemens, C. Rosen, Principles of Bone Biology, fourth edition ed., Academic press2019.

[26] A.R. Guntur, C.J. Rosen, Bone as an Endocrine Organ, Endocr Pract, 18 (2012) 758-762.

[27] S. Weiner, R.L. Reis, Learning from Nature: How to Design New Implantable Biomaterials, Kluwer Academic Publishers, Dordrecht, 2004.

[28] B.D. Burr, M.R. A., Basic and Applied Bone Biology, Second Edition ed., Academic press2019.

[29] Z. Sheikh, M.N. Abdallah, A.A. Hanafi, S. Misbahuddin, H. Rashid, M. Glogauer, Mechanisms of in Vivo Degradation and Resorption of Calcium Phosphate Based Biomaterials, Materials, 8 (2015) 7913-7925.

[30] R. Bartl, B. Frisch, Osteoporosis: Diagnosis, Prevention and Therapy, second edition ed., Springer Berlin Heidelberg2009.

[31] T.L. Andersen, T.E. Sondergaard, K.E. Skorzynska, F. Dagnaes-Hansen, T.L. Plesner, E.M. Hauge, T. Plesner, J.M. Delaisse, A Physical Mechanism for Coupling Bone Resorption and Formation in Adult Human Bone, Am J Pathol, 174 (2009) 239-247.

[32] C. Luxenburg, D. Geblinger, E. Klein, K. Anderson, D. Hanein, B. Geiger, L. Addadi, The Architecture of the Adhesive Apparatus of Cultured Osteoclasts: From Podosome Formation to Sealing Zone Assembly, Plos One, 2 (2007).

[33] O.D. Kennedy, M.B. Schaffler, The Roles of Osteocyte Signaling in Bone, J Am Acad Orthop Sur, 20 (2012) 670-671.

[34] G.S. Baht, L. Vi, B.A. Alman, The Role of the Immune Cells in Fracture Healing, Curr Osteoporos Rep, 16 (2018) 138-145.

[35] A. Schindeler, M.M. McDonald, P. Bokko, D.G. Little, Bone remodeling during fracture repair: The cellular picture, Semin Cell Dev Biol, 19 (2008) 459-466.

[36] J.L. Ford, D.E. Robinson, B.E. Scammell, The fate of soft callus chondrocytes during long bone fracture repair, J Orthop Res, 21 (2003) 54-61.

[37] D. Clark, M. Nakamura, T. Miclau, R. Marcucio, Effects of Aging on Fracture Healing, Curr Osteoporos Rep, 15 (2017) 601-608.

[38] T.J. Cypher, J.P. Grossman, Biological principles of bone graft healing, J Foot Ankle Surg, 35 (1996) 413-417.

[39] W.R. Moore, S.E. Graves, G.I. Bain, Synthetic bone graft substitutes, Anz J Surg, 71 (2001) 354-361.

[40] V. Campana, G. Milano, E. Pagano, M. Barba, C. Cicione, G. Salonna, W. Lattanzi, G. Logroscino, Bone substitutes in orthopaedic surgery: from basic science to clinical practice, J Mater Sci-Mater M, 25 (2014) 2445-2461.

[41] P. Baldwin, D.J. Li, D.A. Auston, H.S. Mir, R.S. Yoon, K.J. Koval, Autograft, Allograft, and Bone Graft Substitutes: Clinical Evidence and Indications for Use in the Setting of Orthopaedic Trauma Surgery, J Orthop Trauma, 33 (2019) 203-213.

[42] M. Hallman, A. Thor, Bone substitutes and growth factors as an alternative/complement to autogenous bone for grafting in implant dentistry, Periodontol 2000, 47 (2008) 172-192.

[43] M.L. Azi, A. Aprato, I. Santi, M. Kfuri, A. Masse, A. Joeris, Autologous bone graft in the treatment of post-traumatic bone defects: a systematic review and meta-analysis, Bmc Musculoskel Dis, 17 (2016).

[44] Z. Buser, D.S. Brodke, J.A. Youssef, H.J. Meisel, S.L. Myhre, R. Hashimoto, J.B. Park, S.T. Yoon, J.C. Wang, Synthetic bone graft versus autograft or allograft for spinal fusion: a systematic review, J Neurosurg-Spine, 25 (2016) 509-516.

[45] M.E. Murphy, B.A. Mccutcheon, J. Grauberger, D. Shepherd, P.R. Maloney, L. Rinaldo, P. Kerezoudis, J.L. Fogelson, A. Nassr, M. Bydon, Allograft versus autograft in cervical and lumbar

spinal fusions: an examination of operative time, length of stay, surgical site infection, and blood transfusions, J Neurosurg Sci, 63 (2019) 11-18.

[46] P.A. Kondell, T. Mattsson, P. Astrand, Immunological responses to maxillary on-lay allogeneic bone grafts, Clin Oral Implan Res, 7 (1996) 373-377.

[47] K.A. Shaw, M.S. Griffith, V.M. Shaw, J.G. Devine, D.M. Gloystein, Harvesting Autogenous Cancellous Bone Graft from the Anterior Iliac Crest, JBJS Essent Surg Tech, 8 (2018) e20.

[48] T. Albrektsson, Repair of bone grafts. A vital microscopic and histological investigation in the rabbit, Scand J Plast Reconstr Surg, 14 (1980) 1-12.

[49] C. Karger, T. Kishi, L. Schneider, F. Fitoussi, A.C. Masquelet, F.S.O. Surg, Treatment of posttraumatic bone defects by the induced membrane technique, Orthop Traumatol-Sur, 98 (2012) 97-102.

[50] P. Cano-Luis, P. Andres-Cano, F.J. Ricon-Recarey, M.A. Giraldez-Sanchez, Treatment of posttraumatic bone defects of the forearm with vascularized fibular grafts. Follow up after fourteen years, Injury, 49 (2018) S27-S35.

[51] A.R. Gazdag, J.M. Lane, D. Glaser, R.A. Forster, Alternatives to Autogenous Bone Graft: Efficacy and Indications, J Am Acad Orthop Surg, 3 (1995) 1-8.

[52] J.M. Colazo, B.C. Evans, A.F. Farinas, S. Al-Kassis, C.L. Duvall, W.P. Thayer, Applied Bioengineering in Tissue Reconstruction, Replacement, and Regeneration, Tissue Eng Part B-Re, 25 (2019) 259-290.

[53] W.Y. Man, T. Monni, R. Jenkins, P. Roberts, Post-operative infection with fresh frozen allograft: reported outcomes of a hospital-based bone bank over 14 years, Cell Tissue Bank, 17 (2016) 269-275.

[54] S.N. Khan, F.P. Cammisa, H.S. Sandha, A.D. Diwan, F.P. Girardi, J.M. Lane, The biology of bone grafting, J Am Acad Orthop Sur, 13 (2005) 77-86.

[55] L. Vastel, C. Masse, P. Mesnil, E. Crozier, F. Padilla, P. Laugier, D. Mitton, J.P. Courpied, Comparative Ultrasound Evaluation of Human Trabecular Bone Graft Properties After Treatment With Different Sterilization Procedures, J Biomed Mater Res B, 90b (2009) 430-437.

[56] F.F. Girlanda, H.S. Feng, M.G. Correa, M.Z. Casati, S.P. Pimentel, F.V. Ribeiro, F.R. Cirano, Deproteinized bovine bone derived with collagen improves soft and bone tissue outcomes in flapless immediate implant approach and immediate provisionalization: a randomized clinical trial, Clin Oral Invest, 23 (2019) 3885-3893.

[57] M.A.T. Aroni, G.J.P.L. de Oliveira, L.C. Spolidorio, O.Z. Andersen, M. Foss, R.A.C. Marcantonio, A. Stavropoulos, Loading deproteinized bovine bone with strontium enhances bone regeneration in rat calvarial critical size defects, Clin Oral Invest, 23 (2019) 1605-1614.

[58] T. Miyamoto, M. Lang, S. Khan, K. Kumagai, M.E. Nunn, The clinical efficacy of deproteinized bovine bone mineral with 10% collagen in conjunction with localized

piezosurgical decortication enhanced orthodontics: A prospective observational study, J Periodontol, 90 (2019) 1106-1115.

[59] M.D. Pierschbacher, E. Ruoslahti, Variants of the Cell Recognition Site of Fibronectin That Retain Attachment-Promoting Activity, P Natl Acad Sci-Biol, 81 (1984) 5985-5988.

[60] M.H. Helfrich, S.A. Nesbitt, E.L. Dorey, M.A. Horton, Rat Osteoclasts Adhere to a Wide-Range of Rgd (Arg-Gly-Asp) Peptide-Containing Proteins, Including the Bone Sialoproteins and Fibronectin, Via a Beta-3 Integrin, J Bone Miner Res, 7 (1992) 335-343.

[61] J. Alayan, S. Ivanovski, A prospective controlled trial comparing xenograft/autogenous bone and collagen-stabilized xenograft for maxillary sinus augmentationComplications, patient-reported outcomes and volumetric analysis, Clin Oral Implan Res, 29 (2018) 248-262.

[62] A. Temmerman, S. Cortellini, J. Van Dessel, A. De Greef, R. Jacobs, R. Dhondt, W. Teughels, M. Quirynen, Bovine-derived xenograft in combination with autogenous bone chips versus xenograft alone for the augmentation of bony dehiscences around oral implants: A randomized, controlled, split-mouth clinical trial, J Clin Periodontol, (2019).

[63] K. Moholkar, D. Taylor, M. O'Reagan, G. Fenelon, A biomechanical analysis of four different methods of harvesting bone-patellar tendon-bone graft in porcine knees, J Bone Joint Surg Am, 84a (2002) 1782-1787.

[64] S.T. Bendtsen, M. Wei, In vitro evaluation of 3D bioprinted tri-polymer network scaffolds for bone tissue regeneration, J Biomed Mater Res A, 105 (2017) 3262-3272.

[65] N. Celikkin, S. Mastrogiacomo, J. Jaroszewicz, X.F. Walboomers, W. Swieszkowski, Gelatin methacrylate scaffold for bone tissue engineering: The influence of polymer concentration, J Biomed Mater Res A, 106 (2018) 201-209.

[66] R. Mishra, R. Varshneya, N. Das, D. Sircar, P. Roy, Synthesis and characterization of gelatin-PVP polymer composite scaffold for potential application in bone tissue engineering, Eur Polym J, 119 (2019) 155-168.

[67] J.Z. Wang, M.L. You, Z.Q. Ding, W.B. Ye, A review of emerging bone tissue engineering via PEG conjugated biodegradable amphiphilic copolymers, Mat Sci Eng C-Mater, 97 (2019) 1021-1035.

[68] J.L. Wang, L.N. Wang, Z.Y. Zhou, H.J. Lai, P. Xu, L. Liao, J.C. Wei, Biodegradable Polymer Membranes Applied in Guided Bone/Tissue Regeneration: A Review, Polymers-Basel, 8 (2016).

[69] J. Babrnakova, V. Pavlinakova, J. Brtnikova, P. Sedlaecek, E. Prosecka, M. Rampichova, E. Filova, V. Hearnden, L. Vojtova, Synergistic effect of bovine platelet lysate and various polysaccharides on the biological properties of collagen-based scaffolds for tissue engineering: Scaffold preparation, chemo-physical characterization, in vitro and ex ovo evaluation, Mat Sci Eng C-Mater, 100 (2019) 236-246.

[70] A. Ataee, Y.C. Li, M. Brandt, C. Wen, Ultrahigh-strength titanium gyroid scaffolds manufactured by selective laser melting (SLM) for bone implant applications, Acta Mater, 158 (2018) 354-368.

[71] M. Hirota, T. Shima, I. Sato, T. Ozawa, T. Iwai, A. Ametani, M. Sato, Y. Noishiki, T. Ogawa, T. Hayakawa, I. Tohnai, Development of a biointegrated mandibular reconstruction device consisting of bone compatible titanium fiber mesh scaffold, Biomaterials, 75 (2016) 223-236.

[72] S. Kamrani, C. Fleck, Biodegradable magnesium alloys as temporary orthopaedic implants: a review, Biometals, 32 (2019) 185-193.

[73] B. Wysocki, J. Idaszek, K. Szlazak, K. Strzelczyk, T. Brynk, K.J. Kurzydlowski, W. Swieszkowski, Post Processing and Biological Evaluation of the Titanium Scaffolds for Bone Tissue Engineering, Materials, 9 (2016).

[74] G. Hannink, J.J.C. Arts, Bioresorbability, porosity and mechanical strength of bone substitutes: What is optimal for bone regeneration?, Injury, 42 (2011) S22-S25.

[75] P.S. Santos, T.M. Cestari, J.B. Paulin, R. Martins, C.A. Rocha, R.V.N. Arantes, B.C. Costa, C.M. dos Santos, G.F. Assis, R. Taga, Osteoinductive porous biphasic calcium phosphate ceramic as an alternative to autogenous bone grafting in the treatment of mandibular bone critical-size defects, J Biomed Mater Res B, 106 (2018) 1546-1557.

[76] Z.R. Tang, X.F. Li, Y.F. Tan, H.S. Fan, X.D. Zhang, The material and biological characteristics of osteoinductive calcium phosphate ceramics, Regen Biomater, 5 (2018) 43-59.

[77] B. Li, X.L. Liao, L. Zheng, X.D. Zhu, Z. Wang, H.S. Fan, X.D. Zhang, Effect of nanostructure on osteoinduction of porous biphasic calcium phosphate ceramics (vol 8, pg 3794, 2012), Acta Biomater, 9 (2013) 9588-9588.

[78] J.M. Bouler, P. Pilet, O. Gauthier, E. Verron, Biphasic calcium phosphate ceramics for bone reconstruction: A review of biological response, Acta Biomater, 53 (2017) 1-12.

[79] H.H. Enezei, A. Ahmad, M.F. Khamis, J. Suzuki, Y. Sugita, H. Maeda, S. Alshehadat, N.H.A. Razak, S.K. Abbas, A. Al Qabbani, M.K. Alam, Enhanced Osteogenic and Angiogenic-Related Gene Expression of Human Dental Stem Cells on Biphasic Calcium Phosphate Scaffold Treated with Vascular Endothelial Growth Factor: Part I, J Hard Tissue Biol, 26 (2017) 373-379.

[80] G.T. Qiu, Z.J. Shi, H.H.K. Xu, B. Yang, M.D. Weir, G.J. Li, Y. Song, J.X. Wang, K. Hu, P. Wang, L. Zhao, Bone regeneration in minipigs via calcium phosphate cement scaffold delivering autologous bone marrow mesenchymal stem cells and platelet-rich plasma, J Tissue Eng Regen M, 12 (2018) E937-E948.

[81] Y. Lin, S.H. Huang, R. Zou, X.L. Gao, J.P. Ruan, M.D. Weir, M.A. Reynolds, W. Qin, X.F. Chang, H.J. Fu, H.H.K. Xu, Calcium phosphate cement scaffold with stem cell co-culture and prevascularization for dental and craniofacial bone tissue engineering, Dent Mater, 35 (2019) 1031-1041.

[82] Z.M. Wang, K.F. Wang, X. Lu, M.Q. Li, H.R. Liu, C.M. Xie, F.Z. Meng, O. Jiang, C. Li, W. Zhi, BMP-2 encapsulated polysaccharide nanoparticle modified biphasic calcium phosphate scaffolds for bone tissue regeneration, J Biomed Mater Res A, 103 (2015) 1520-1532.

[83] Q.G. Cao, Z.W. He, W.Q. Sun, G.T. Fan, J.N. Zhao, N.R. Bao, T.J. Ye, Improvement of calcium phosphate scaffold osteogenesis in vitro via combination of glutamate-modified BMP-2 peptides, Mat Sci Eng C-Mater, 96 (2019) 412-418.

[84] L. de Siqueira, R.F. Gouveia, L. Grenho, F.J. Monteiro, M.H. Fernandes, E.S. Triches, Highly porous 45S5 bioglass-derived glass-ceramic scaffolds by gelcasting of foams, J Mater Sci, 53 (2018) 10718-10731.

[85] M. Trunec, Z. Chlup, Subtractive manufacturing of customized hydroxyapatite scaffolds for bone regeneration, Ceram Int, 43 (2017) 11265-11273.

[86] S. Bose, J. Darsell, H.L. Hosick, L. Yang, D.K. Sarkar, A. Bandyopadhyay, Processing and characterization of porous alumina scaffolds, J Mater Sci-Mater M, 13 (2002) 23-28.

[87] Y.W. Moon, I.J. Choi, Y.H. Koh, H.E. Kim, Porous alumina ceramic scaffolds with biomimetic macro/micro-porous structure using three-dimensional (3-D) ceramic/camphene-based extrusion, Ceram Int, 41 (2015) 12371-12377.

[88] G.C. Gazquez, H. Chen, A. Solmaz, B.A. Boukamp, J.E. Ten Elshof, L. Moroni, Flexible and osteoinductive Yttrium Stabilized Zirconia scaffold for bone regeneration, J Tissue Eng Regen M, 8 (2014) 117-118.

[89] S.H. An, T. Matsumoto, H. Miyajima, A. Nakahira, K.H. Kim, S. Imazato, Porous zirconia/hydroxyapatite scaffolds for bone reconstruction, Dent Mater, 28 (2012) 1221-1231.

[90] A. Marques, G. Miranda, D. Faria, P. Pinto, F. Silva, O. Carvalho, Novel design of low modulus high strength zirconia scaffolds for biomedical applications, J Mech Behav Biomed, 97 (2019) 375-384.

[91] P. Ducheyne, L.L. Hench, A. Kagan, M. Martens, A. Bursens, J.C. Mulier, Effect of Hydroxyapatite Impregnation on Skeletal Bonding of Porous Coated Implants, J Biomed Mater Res, 14 (1980) 225-237.

[92] R.S. Levine, In-Vitro Reprecipitation of Hydroxyapatite in Carious Dentin, Caries Res, 6 (1972) 279-&.

[93] R.L. Speirs, F. Brudevold, M. Spinelli, Solution Rate of Hydroxyapatite in Acetate Buffer Containing Low Concentrations of Foreign Ions, J Dent Res, 42 (1963) 811-&.

[94] I. Grigoraviciute-Puroniene, A. Zarkov, K. Tsuru, K. Ishikawa, A. Kareiva, A novel synthetic approach for the calcium hydroxyapatite from the food products, J Sol-Gel Sci Techn, 91 (2019) 63-71.

[95] C.J. Hsu, W.Y. Chou, H.P. Teng, W.N. Chang, Y.J. Chou, Coralline hydroxyapatite and laminectomy-derived bone as adjuvant graft material for lumbar posterolateral fusion, J Neurosurg-Spine, 3 (2005) 271-275.

[96] N.A.S. Mohd Pu'ad, P. Koshy, H.Z. Abdullah, M.I. Idris, T.C. Lee, Syntheses of hydroxyapatite from natural sources, Heliyon, 5 (2019) e01588.

[97] S. Pramanik, A.K. Agarwal, K.N. Rai, A. Garg, Development of high strength hydroxyapatite by solid-state-sintering process, Ceram Int, 33 (2007) 419-426.

[98] H.B. Zhang, K.C. Zhou, Z.Y. Li, S.P. Huang, Plate-like hydroxyapatite nanoparticles synthesized by the hydrothermal method, J Phys Chem Solids, 70 (2009) 243-248.

[99] Y.J. Wang, S.H. Zhang, K. Wei, N.R. Zhao, J.D. Chen, X.D. Wang, Hydrothermal synthesis of hydroxyapatite nanopowders using cationic surfactant as a template, Mater Lett, 60 (2006) 1484-1487.

[100] O. Yildiz, Combined precipitation and spray drying for the synthesis of hydroxyapatite nanopowders as soft spherical granules, Ceram Int, 44 (2018) 19809-19817.

[101] L.Y. Cao, C.B. Zhang, H.F. Huang, Synthesis of hydroxyapatite nanoparticles in ultrasonic precipitation, Ceram Int, 31 (2005) 1041-1044.

[102] J. Cihlar, A. Buchal, M. Trunec, Kinetics of thermal decomposition of hydroxyapatite bioceramics, J Mater Sci, 34 (1999) 6121-6131.

[103] C.J. Liao, F.H. Lin, K.S. Chen, J.S. Sun, Thermal decomposition and reconstitution of hydroxyapatite in air atmosphere, Biomaterials, 20 (1999) 1807-1813.

[104] I.S. Neira, F. Guitian, T. Taniguchi, T. Watanabe, M. Yoshimura, Hydrothermal synthesis of hydroxyapatite whiskers with sharp faceted hexagonal morphology, J Mater Sci, 43 (2008) 2171-2178.

[105] Bioceramics and their clinical application, Woodhead Publishing Limited 2008.

[106] G. Muralithran, S. Ramesh, The effects of sintering temperature on the properties of hydroxyapatite, Ceram Int, 26 (2000) 221-230.

[107] K. Nakata, T. Kubo, C. Numako, T. Onoki, A. Nakahira, Synthesis and Characterization of Silicon-Doped Hydroxyapatite, Mater Trans, 50 (2009) 1046-1049.

[108] T. Kanazawa, H. Monma, Y. Moriyoshi, Reaction chemistry of hydroxyapatite: formation and decomposition, Proc. Estonian Acad. Sci. Chem., 49 (2000) 19 - 28.

[109] P. Stastny, P. Vacek, M. Trunec, Characterization of microstructure and phase distribution of sintered multiphasic calcium phosphate bioceramics, Ceram Int, (2019).

[110] F.H. Perera, F.J. Martinez-Vazquez, P. Miranda, A.L. Ortiz, A. Pajares, Clarifying the effect of sintering conditions on the microstructure and mechanical properties of beta-tricalcium phosphate, Ceram Int, 36 (2010) 1929-1935.

[111] T.J. Brunner, R.N. Grass, M. Bohner, W.J. Stark, Effect of particle size, crystal phase and crystallinity on the reactivity of tricalcium phosphate cements for bone reconstruction, J Mater Chem, 17 (2007) 4072-4078.

[112] I.S. Cho, H.S. Ryu, J.R. Kim, D.W. Kim, K.S. Hong, Sintering behavior and microwave dielectric properties of tricalcium phosphate polymorphs, Japanese Journal of Applied Physics Part 1-Regular Papers Brief Communications & Review Papers, 46 (2007) 2999-3003.

[113] M. Kazemi, M.M. Dehghan, M. Azami, Biological evaluation of porous nanocomposite scaffolds based on strontium substituted beta-TCP and bioactive glass: An in vitro and in vivo study, Mat Sci Eng C-Mater, 105 (2019).

[114] Y.Z. Shi, J. Liu, L.M. Yu, L.Z. Zhong, H.B. Jiang, beta-TCP scaffold coated with PCL as biodegradable materials for dental applications, Ceram Int, 44 (2018) 15086-15091.

[115] X.S. Wang, M.H. Lin, Y.Q. Kang, Engineering Porous beta-Tricalcium Phosphate (beta-TCP) Scaffolds with Multiple Channels to Promote Cell Migration, Proliferation, and Angiogenesis, Acs Appl Mater Inter, 11 (2019) 9223-9232.

[116] S. Laasri, M. Taha, E.K. Hlil, A. Laghzizil, A. Hajjaji, Manufacturing and mechanical properties of calcium phosphate biomaterials, Cr Mecanique, 340 (2012) 715-720.

[117] H.S. Ryu, H.J. Youn, K.S. Hong, B.S. Chang, C.K. Lee, S.S. Chung, An improvement in sintering property of beta-tricalcium phosphate by addition of calcium pyrophosphate, Biomaterials, 23 (2002) 909-914.

[118] G. Cicek, E.A. Aksoy, C. Durucan, N. Hasirci, Alpha-tricalcium phosphate (alpha-TCP): solid state synthesis from different calcium precursors and the hydraulic reactivity, J Mater Sci-Mater M, 22 (2011) 809-817.

[119] A. Bandyopadhyay, S. Bernard, W.C. Xue, S. Bose, Calcium phosphate-based resorbable ceramics: Influence of MgO, ZnO, and SiO2 dopants, J Am Ceram Soc, 89 (2006) 2675-2688.

[120] S.S. Banerjee, S. Tarafder, N.M. Davies, A. Bandyopadhyay, S. Bose, Understanding the influence of MgO and SrO binary doping on the mechanical and biological properties of beta-TCP ceramics, Acta Biomater, 6 (2010) 4167-4174.

[121] R. Enderle, F. Gotz-Neunhoeffer, M. Gobbels, F.A. Muller, P. Greil, Influence of magnesium doping on the phase transformation temperature of beta-TCP ceramics examined by Rietveld refinement, Biomaterials, 26 (2005) 3379-3384.

[122] S.V. Dorozhkin, Mechanism of solid-state conversion of non-stoichiometric hydroxyapatite to diphase calcium phosphate, Russ Chem B+, 52 (2003) 2369-2375.

[123] U. Gbureck, T. Hoelzel, I. Biermann, J.E. Barralet, L.M. Grover, Preparation of tricalcium phosphate/calcium pyrophosphate structures via rapid prototyping, J Mater Sci-Mater M, 19 (2008) 1559-1563.

[124] T. Kanazawa, H. Monma, Y. Moriyoshi, Reaction chemistry of hydroxyapatite: formation and decomposition, Proc. Est. Acad. Sci. Chem., 49 (2000) 19–28.

[125] H. Zhou, S.S. Hou, M.J. Zhang, H. Chai, Y. Liu, S.B. Bhaduri, L. Yang, L.H. Deng, Synthesis of beta-TCP and CPP containing biphasic calcium phosphates by a robust technique, Ceram Int, 42 (2016) 11032-11038.

[126] Y.T. Lee, M.H. Youn, R.K. Paul, K.H. Lee, H.Y. Song, In situ synthesis of spherical BCP nanopowders by microwave asssisted process, Mater Chem Phys, 104 (2007) 249-253.

[127] Z. Mohammadi, A.S.M. Mesgar, F. Rasouli-Disfani, Preparation and characterization of single phase, biphasic and triphasic calcium phosphate whisker-like fibers by homogenous precipitation using urea, Ceram Int, 42 (2016) 6955-6961.

[128] C.K. Hsu, The preparation of biphasic porous calcium phosphate by the mixture of Ca(H2PO4)(2)center dot H2O and CaCO3, Mater Chem Phys, 80 (2003) 409-420.

[129] E. Champion, Sintering of calcium phosphate bioceramics, Acta Biomater, 9 (2013) 5855-5875.

[130] C. Zou, K. Cheng, W.J. Weng, C.L. Song, P.Y. Du, G. Shen, G.R. Han, Characterization and dissolution-reprecipitation behavior of biphasic tricalcium phosphate powders, J Alloy Compd, 509 (2011) 6852-6858.

[131] L. Orly, G. Daculsi, M. Heughebaert, L.M. Kerebel, High-Resolution Tem and Electron-Diffraction Studies of Calcium-Phosphate Biomaterials, J Dent Res, 65 (1986) 540-540.

[132] S.C. Curtze, M. Kratz, M. Steinert, S. Vogt, Step down Vascular Calcification Analysis using State-of-the-Art Nanoanalysis Techniques, Sci Rep-Uk, 6 (2016).

[133] R.B. Wang, W.J. Weng, X.L. Deng, K. Cheng, X.G. Liu, P.Y. Du, G. Shen, G.R. Han, Dissolution behavior of submicron biphasic tricalcium phosphate powders, Bioceramics 18, Pts 1 and 2, 309-311 (2006) 223-226.

[134] O. Brown, M. McAfee, S. Clarke, F. Buchanan, Sintering of biphasic calcium phosphates, J Mater Sci-Mater M, 21 (2010) 2271-2279.

[135] R.W.N. Nilen, P.W. Richter, The thermal stability of hydroxyapatite in biphasic calcium phosphate ceramics, J Mater Sci-Mater M, 19 (2008) 1693-1702.

[136] S.V. Dorozhkin, Dissolution mechanism of calcium apatites in acids: A review of literature, World J Methodol, 2 (2012) 1-17.

[137] L.C. Chow, Next generation calcium phosphate-based biomaterials, Dent Mater J, 28 (2009) 1-10.

[138] P. Ducheyne, Q. Qiu, Bioactive ceramics: the effect of surface reactivity on bone formation and bone cell function, Biomaterials, 20 (1999) 2287-2303.

[139] A. Carino, C. Ludwig, A. Cervellino, E. Muller, A. Testino, Formation and transformation of calcium phosphate phases under biologically relevant conditions: Experiments and modelling, Acta Biomater, 74 (2018) 478-488.

[140] W. Suchanek, M. Yoshimura, Processing and properties of hydroxyapatite-based biomaterials for use as hard tissue replacement implants, J Mater Res, 13 (1998) 94-117.

[141] S.M.H. Ghazanfari, A. Zamanian, Phase transformation, microstructural and mechanical properties of hydroxyapatite/alumina nanocomposite scaffolds produced by freeze casting, Ceram Int, 39 (2013) 9835-9844.

[142] H.W. Kido, D.A. Ribeiro, P. de Oliveira, N.A. Parizotto, C.C. Camilo, C.A. Fortulan, E. Marcantonio, V.H.P. da Silva, A.C.M. Renno, Biocompatibility of a porous alumina ceramic scaffold coated with hydroxyapatite and bioglass, J Biomed Mater Res A, 102 (2014) 2072-2078.

[143] S.F. Mansour, S.I. El-Dek, M.K. Ahmed, Physico-mechanical and morphological features of zirconia substituted hydroxyapatite nano crystals, Sci Rep-Uk, 7 (2017) 1-21.

[144] J.G. Dellinger, A.M. Wojtowicz, R.D. Jamison, Effects of degradation and porosity on the load bearing properties of model hydroxyapatite bone scaffolds, J Biomed Mater Res A, 77a (2006) 563-571.

[145] R.M. Pilliar, M.J. Filiaggi, J.D. Wells, M.D. Grynpas, R.A. Kandel, Porous calcium polyphosphate scaffolds for bone substitute applications - in vitro characterization, Biomaterials, 22 (2001) 963-972.

[146] A. Motealleh, S. Eqtesadi, A. Civantos, A. Pajares, P. Miranda, Robocast 45S5 bioglass scaffolds: in vitro behavior, J Mater Sci, 52 (2017) 9179-9191.

[147] M. Rumpler, A. Woesz, J.W.C. Dunlop, J.T. van Dongen, P. Fratzl, The effect of geometry on three-dimensional tissue growth, J R Soc Interface, 5 (2008) 1173-1180.

[148] C.M. Bidan, K.P. Kommareddy, M. Rumpler, P. Kollmannsberger, Y.J.M. Brechet, P. Fratzl, J.W.C. Dunlop, How Linear Tension Converts to Curvature: Geometric Control of Bone Tissue Growth, Plos One, 7 (2012).

[149] H. Jinnai, H. Watashiba, T. Kajihara, Y. Nishikawa, M. Takahashi, M. Ito, Surface curvatures of trabecular bone microarchitecture, Bone, 30 (2002) 191-194.

[150] C.M. Nelson, R.P. Jean, J.L. Tan, W.F. Liu, N.J. Sniadecki, A.A. Spector, C.S. Chen, Emergent patterns of growth controlled by multicellular form and mechanics, P Natl Acad Sci USA, 102 (2005) 11594-11599.

[151] S. Huang, C.S. Chen, D.E. Ingber, Control of cyclin D1, p27(Kip1), and cell cycle progression in human capillary endothelial cells by cell shape and cytoskeletal tension, Mol Biol Cell, 9 (1998) 3179-3193.

[152] M. Sladkova, M. Palmer, C. Ohman, R.J. Alhaddad, A. Esmael, J. Cheng, H. Engqvist, G. de Peppo, Development of Macroporous Ceramic Scaffolds for Bone Engineering Applications using Human Induced Pluripotent Stem Cells, Tissue Eng Pt A, 21 (2015) S117-S117.

[153] S. Teixeira, H. Fernandes, A. Leusink, C. van Blitterswijk, M.P. Ferraz, F.J. Monteiro, J. de Boer, In vivo evaluation of highly macroporous ceramic scaffolds for bone tissue engineering, J Biomed Mater Res A, 93a (2010) 567-575.

[154] M. Mastrogiacomo, S. Scaglione, R. Martinetti, L. Dolcini, F. Beltrame, R. Cancedda, R. Quarto, Role of scaffold internal structure on in vivo bone formation in macroporous calcium phosphate bioceramics, Biomaterials, 27 (2006) 3230-3237.

[155] Y. Kuboki, Q.M. Jin, H. Takita, Geometry of carriers controlling phenotypic expression in BMP-induced osteogenesis and chondrogenesis, J Bone Joint Surg Am, 83a (2001) S105-S115.

[156] E. Tsuruga, H. Takita, H. Itoh, Y. Wakisaka, Y. Kuboki, Pore size of porous hydroxyapatite as the cell-substratum controls BMP-induced osteogenesis, J Biochem-Tokyo, 121 (1997) 317-324.

[157] F. Bai, J.K. Zhang, Z. Wang, J.X. Lu, J.A. Chang, J.A. Liu, G.L. Meng, X. Dong, The effect of pore size on tissue ingrowth and neovascularization in porous bioceramics of controlled architecture in vivo, Biomed Mater, 6 (2011).

[158] B.J. Story, W.R. Wagner, D.M. Gaisser, S.D. Cook, A.M. Rust-Dawicki, In vivo performance of a modified CSTi dental implant coating, Int J Oral Max Impl, 13 (1998) 749-757.

[159] T.D. Roy, J.L. Simon, J.L. Ricci, E.D. Rekow, V.P. Thompson, J.R. Parsons, Performance of degradable composite bone repair products made via three-dimensional fabrication techniques, J Biomed Mater Res A, 66a (2003) 283-291.

[160] M.C. Kruyt, J.D. de Bruijn, C.E. Wilson, F.C. Oner, C.A. van Blitterswijk, A.J. Verbout, W.J.A. Dhert, Viable osteogenic cells are obligatory for tissue-engineered ectopic bone formation in goats, Tissue Eng, 9 (2003) 327-336.

[161] V. Karageorgiou, D. Kaplan, Porosity of 3D biomaterial scaffolds and osteogenesis, Biomaterials, 26 (2005) 5474-5491.

[162] A. Barba, A. Diez-Escudero, Y. Maazouz, K. Rappe, M. Espanol, E.B. Montufar, M. Bonany, J.M. Sadowska, J. Guillern-Marti, C. Ohman-Magi, C. Persson, M.C. Manzanares, J. Franch, M.P. Ginebra, Osteoinduction by Foamed and 3D-Printed Calcium Phosphate Scaffolds: Effect of Nanostructure and Pore Architecture, Acs Appl Mater Inter, 9 (2017) 41722-41736.

[163] A.L. Rosa, M.M. Beloti, P.T. Oliveira, R. Van Noort, Osseointegration and osseoconductivity of hydroxyapatite of different microporosities, J Mater Sci-Mater M, 13 (2002) 1071-1075.

[164] J. Vivanco, J. Slane, R. Nay, A. Simpson, H.L. Ploeg, The effect of sintering temperature on the microstructure and mechanical properties of a bioceramic bone scaffold, J Mech Behav Biomed, 4 (2011) 2150-2160.

[165] J.X. Lu, B. Flautre, K. Anselme, P. Hardouin, A. Gallur, M. Descamps, B. Thierry, Role of interconnections in porous bioceramics on bone recolonization in vitro and in vivo, J Mater Sci-Mater M, 10 (1999) 111-120.

[166] Q.M. Jin, H. Takita, T. Kohgo, K. Atsumi, H. Itoh, Y. Kuboki, Effects of geometry of hydroxyapatite as a cell substratum in BMP-induced ectopic bone formation, J Biomed Mater Res, 51 (2000) 491-499.

[167] F. Darus, R.M. Isa, N. Mamat, M. Jaafar, Techniques for fabrication and construction of three-dimensional bioceramic scaffolds: Effect on pores size, porosity and compressive strength, Ceram Int, 44 (2018) 18400-18407.

[168] S.H. Li, J.R. de Wijn, J.P. Li, P. Layrolle, K. de Groot, Macroporous biphasic calcium phosphate scaffold with high permeability/porosity ratio, Tissue Eng, 9 (2003) 535-548.

[169] M.J. Mienaltowski, D.E. Birk, Structure, Physiology, and Biochemistry of Collagens, Progress in Heritable Soft Connective Tissue Diseases, 802 (2014) 5-29.

[170] A.K. Lynn, I.V. Yannas, W. Bonfield, Antigenicity and immunogenicity of collagen, J Biomed Mater Res B, 71b (2004) 343-354.

[171] C.J. Dong, Y.G. Lv, Application of Collagen Scaffold in Tissue Engineering: Recent Advances and New Perspectives, Polymers-Basel, 8 (2016).

[172] S.M. Krane, Collagenases and Collagen Degradation, J Invest Dermatol, 79 (1982) S83-S86.

[173] K.K. Moncal, R.S.T. Aydin, M. Abu-Laban, D.N. Heo, E. Rizk, S.M. Tucker, G.S. Lewis, D. Hayes, I.T. Ozbolat, Collagen-infilled 3D printed scaffolds loaded with miR-148b-transfected bone marrow stem cells improve calvarial bone regeneration in rats, Mat Sci Eng C-Mater, 105 (2019).

[174] E. Prosecka, M. Rampichova, L. Vojtova, D. Tvrdik, S. Melcakova, J. Juhasova, M. Plencner, R. Jakubova, J. Jancar, A. Necas, P. Kochova, J. Klepacek, Z. Tonar, E. Amler, Optimized conditions for mesenchymal stem cells to differentiate into osteoblasts on a collagen/hydroxyapatite matrix, J Biomed Mater Res A, 99a (2011) 307-315.

[175] L. Chen, Z.X. Wu, Y.L. Zhou, L.L. Li, Y. Wang, Z.L. Wang, Y. Chen, P.B. Zhang, Biomimetic porous collagen/hydroxyapatite scaffold for bone tissue engineering, J Appl Polym Sci, 134 (2017).

[176] N.N. Panda, S. Jonnalagadda, K. Pramanik, Development and evaluation of cross-linked collagen-hydroxyapatite scaffolds for tissue engineering, J Biomat Sci-Polym E, 24 (2013) 2031-2044.

[177] M. Mohseni, A. Jahandideh, G. Abedi, A. Akbarzadeh, S. Hesaraki, Assessment of tricalcium phosphate/collagen (TCP/collagene)nanocomposite scaffold compared with hydroxyapatite (HA) on healing of segmental femur bone defect in rabbits, Artif Cell Nanomed B, 46 (2018) 242-249.

[178] J. Lee, G. Kim, Calcium-Deficient Hydroxyapatite/Collagen/Platelet-Rich Plasma Scaffold with Controlled Release Function for Hard Tissue Regeneration, Acs Biomater Sci Eng, 4 (2018) 278-289.

[179] P.O.E. Mueller, B.G. Harmon, W.P. Hay, L.M. Amoroso, Effect of carboxymethylcellulose and a hyaluronate-carboxymethylcellulose membrane on healing of intestinal anastomoses in horses, Am J Vet Res, 61 (2000) 369-374.

[180] A.A. Shefa, M. Taz, M. Hossain, Y.S. Kim, S.Y. Lee, B.T. Lee, Investigation of efficiency of a novel, zinc oxide loaded TEMPO-oxidized cellulose nanofiber based hemostat for topical bleeding, Int J Biol Macromol, 126 (2019) 786-795.

[181] F. Bassetto, V. Vindigni, C. Scarpa, C. Botti, G. Botti, Use of oxidized regenerated cellulose to stop bleeding after a facelift procedure, Aesthet Plast Surg, 32 (2008) 807-809.

[182] A.T. Rozanski, B.R. Viers, A.G. Liu, N.A. Shakir, T.J. Pagliara, J.M. Scott, M.L. West, A.F. Morey, Oxidized Regenerated Cellulose (Fibrillar) Reduces Risk of Postoperative Corporal Bleeding Following Inflatable Penile Prosthesis Surgery, Urology, 108 (2017) 190-194.

[183] D.S. Zimnitsky, T.L. Yurkshtovich, P.M. Bychkovsky, Synthesis and characterization of oxidized cellulose, J Polym Sci Pol Chem, 42 (2004) 4785-4791.

[184] W.K. Son, J.H. Youk, W.H. Park, Preparation of ultrafine oxidized cellulose mats via electrospinning, Biomacromolecules, 5 (2004) 197-201.

[185] K. Novotna, P. Havelka, T. Sopuch, K. Kolarova, V. Vosmanska, V. Lisa, V. Svorcik, L. Bacakova, Cellulose-based materials as scaffolds for tissue engineering, Cellulose, 20 (2013) 2263-2278.

[186] H. Qiao, T.F. Guo, Y.D. Zheng, L. Zhao, Y. Sun, Y. Liu, Y.J. Xie, A novel microporous oxidized bacterial cellulose/arginine composite and its effect on behavior of fibroblast/endothelial cell, Carbohyd Polym, 184 (2018) 323-332.

[187] A. Teotia, S. Ikram, B. Gupta, Structural characterization of chitosan and oxidized carboxymethyl cellulose based freeze-dried films, Polym Bull, 69 (2012) 175-188.

[188] Cellulose and cellulose derivatives: Synthesis, modification and application, Nova science publishers, New York, 2015.

[189] W.E.G. Muller, X.H. Wang, B. Diehl-Seifert, K. Kropf, U. Schlossmacher, I. Lieberwirth, G. Glasser, M. Wiens, H.C. Schroder, Inorganic polymeric phosphate/polyphosphate as an inducer of alkaline phosphatase and a modulator of intracellular Ca2+ level in osteoblasts (SaOS-2 cells) in vitro, Acta Biomater, 7 (2011) 2661-2671.

[190] X.H. Wang, H.C. Schroder, B. Diehl-Seifert, K. Kropf, U. Schlossmacher, M. Wiens, W.E.G. Muller, Dual effect of inorganic polymeric phosphate/polyphosphate on osteoblasts and osteoclasts in vitro, J Tissue Eng Regen M, 7 (2013) 767-776.

[191] W.E.G. Muller, M. Neufurth, E. Tolba, S.F. Wang, W. Geurtsen, Q.L. Feng, H.C. Schroder, X.H. Wang, A biomimetic approach to ameliorate dental hypersensitivity by amorphous polyphosphate microparticles, Dent Mater, 32 (2016) 775-783.

[192] M.E. Lynge, R. van der Westen, A. Postma, B. Stadler, Polydopamine-a nature-inspired polymer coating for biomedical science, Nanoscale, 3 (2011) 4916-4928.

[193] V. Ball, Polydopamine Nanomaterials: Recent Advances in Synthesis Methods and Applications, Front Bioeng Biotech, 6 (2018).

[194] M.O. Klein, D.S. Battagello, A.R. Cardoso, D.N. Hauser, J.C. Bittencourt, R.G. Correa, Dopamine: Functions, Signaling, and Association with Neurological Diseases, Cellular and Molecular Neurobiology, 39 (2019) 31-59.

[195] S.E. Park, A. Georgescu, J.M. Oh, K.W. Kwon, D. Huh, Polydopamine-Based Interfacial Engineering of Extracellular Matrix Hydrogels for the Construction and Long-Term Maintenance of Living Three-Dimensional Tissues, ACS Appl Mater Interfaces, 11 (2019) 23919-23925.

[196] Y. Zhu, D.D. Liu, X.L. Wang, Y. He, W.J. Luan, F.Z. Qi, J.D. Ding, Polydopamine-mediated covalent functionalization of collagen on a titanium alloy to promote biocompatibility with soft tissues, J Mater Chem B, 7 (2019) 2019-2031.

[197] J.S. Lee, J.C. Lee, J.S. Heo, Polydopamine-assisted BMP-2 immobilization on titanium surface enhances the osteogenic potential of periodontal ligament stem cells via integrin-mediated cell-matrix adhesion, J Cell Commun Signal, 12 (2018) 661-672.

[198] G.H. Lee, P. Makkar, K. Paul, B. Lee, Development of BMP-2 immobilized polydopamine mediated multichannelled biphasic calcium phosphate granules for improved bone regeneration, Mater Lett, 208 (2017) 122-125.

[199] G.H. Lee, P. Makkar, K. Paul, B.T. Lee, Comparative Bone Regeneration Potential Studies of Collagen, Heparin, and Polydopamine-Coated Multichannelled BCP Granules, Asaio J, 64 (2018) 115-121.

[200] L. Forte, P. Torricelli, F. Bonvicini, E. Boanini, G.A. Gentilomi, G. Lusvardi, E. Della Bella, M. Fini, E.V. Nepita, A. Bigi, Biomimetic fabrication of antibacterial calcium phosphates mediated by polydopamine, J Inorg Biochem, 178 (2018) 43-53.

[201] Y. Hu, W.H. Dan, S.B. Xiong, Y. Kang, A. Dhinakar, J. Wu, Z.P. Gu, Development of collagen/polydopamine complexed matrix as mechanically enhanced and highly biocompatible semi-natural tissue engineering scaffold, Acta Biomater, 47 (2017) 135-148.

[202] P.K. Forooshani, E. Polega, K. Thomson, M.S.A. Bhuiyan, R. Pinnaratip, M. Trought, C. Kendrick, Y.S. Gao, K.A. Perrine, L. Pan, B.P. Lee, Antibacterial Properties of Mussel-Inspired Polydopamine Coatings Prepared by a Simple Two-Step Shaking-Assisted Method, Front Chem, 7 (2019).

[203] P. Charoenlarp, A.K. Rajendran, S. Iseki, Role of fibroblast growth factors in bone regeneration, Inflamm Regen, 37 (2017) 10.

[204] J.D. Coffin, C. Homer-Bouthiette, M.M. Hurley, Fibroblast Growth Factor 2 and Its Receptors in Bone Biology and Disease, J Endocr Soc, 2 (2018) 657-671.

[205] A. Montero, Y. Okada, M. Tomita, M. Ito, H. Tsurukami, T. Nakamura, T. Doetschman, J.D. Coffin, M.M. Hurley, Disruption of the fibroblast growth factor-2 gene results in decreased bone mass and bone formation, J Clin Invest, 105 (2000) 1085-1093.

[206] G. Zellin, A. Linde, Effects of recombinant human fibroblast growth factor-2 on osteogenic cell populations during orthopic osteogenesis in vivo, Bone, 26 (2000) 161-168.

[207] K.S. Hong, E.C. Kim, S.H. Bang, C.H. Chung, Y.I. Lee, J.K. Hyun, H.H. Lee, J.H. Jang, T.I. Kim, H.W. Kim, Bone regeneration by bioactive hybrid membrane containing FGF2 within rat calvarium, J Biomed Mater Res A, 94a (2010) 1187-1194.

[208] H. Kawaguchi, S. Jingushi, T. Izumi, M. Fukunaga, T. Matsushita, T. Nakamura, K. Mizuno, T. Nakamura, K. Nakamura, Local application of recombinant human fibroblast growth factor-2 on bone repair: A dose-escalation prospective trial on patients with osteotomy, J Orthop Res, 25 (2007) 480-487.

[209] B. Poon, T. Kha, S. Tran, C.R. Dass, Bone morphogenetic protein-2 and bone therapy: successes and pitfalls, J Pharm Pharmacol, 68 (2016) 139-147.

[210] S. Govender, C. Csimma, H.K. Genant, A. Valentin-Opran, Y. Amit, R. Arbel, H. Aro, D. Atar, M. Bishay, M.G. Borner, P. Chiron, P. Choong, J. Cinats, B. Courtenay, R. Feibel, B. Geulette, S. Govender, C. Gravel, N. Haas, M. Raschke, E. Hammacher, D. van der Velde, P. Hardy, M. Holt, C. Josten, R.L. Ketterl, B. Lindeque, G. Lob, H. Mathevon, G. Mccoy, D. Marsh, R. Miller, E. Munting, S. Oevre, L. Nordsletten, A. Patel, A. Pohl, W. Rennie, P. Reynders, P.M. Rommens, J. Rondia, W.C. Rossouw, P.J. Daneel, S. Ruff, A. Ruter, S. Santavirta, T.A. Schildhauer, C. Gekle, R. Schnettler, D. Segal, H. Seiler, R.B. Snowdowne, J. Stapert, G. Taglang, R. Verdonk, L. Vogels, A. Weckbach, A. Wentzensen, T. Wisniewski, B.S. Grp, Recombinant human bone morphogenetic protein-2 for treatment of open tibial fractures - A prospective, controlled, randomized study of four hundred and fifty patients, J Bone Joint Surg Am, 84a (2002) 2123-2134.

[211] M.M. Abd-El-Barr, J.B. Cox, M.U. Antonucci, J. Bennett, G.J.A. Murad, D.W. Pincus, Recombinant Human Bone Morphogenetic Protein-2 as an Adjunct for Spine Fusion in a Pediatric Population, Pediatr Neurosurg, 47 (2011) 266-271.

[212] G.S. Cooper, T.D. Kou, Risk of Cancer After Lumbar Fusion Surgery With Recombinant Human Bone Morphogenic Protein-2 (rh-BMP-2), Spine, 38 (2013) 1862-1868.

[213] C. Sayama, M. Willsey, M. Chintagumpala, A. Brayton, V. Briceno, S.L. Ryan, T.G. Luerssen, S.W. Hwang, A. Jea, Routine use of recombinant human bone morphogenetic protein-2 in posterior fusions of the pediatric spine and incidence of cancer, J Neurosurg-Pediatr, 16 (2015) 4-13.

[214] K.A. Hing, L.E. Wilson, T. Buckland, Comparative performance of three ceramic bone graft substitutes, Spine J, 7 (2007) 475-490.

[215] M. Coughlan, M. Davies, A.K. Mostert, D. Nanda, P.C. Willems, G. Rosenberg, R. Ferch, A Prospective, Randomized, Multicenter Study Comparing Silicated Calcium Phosphate versus

BMP-2 Synthetic Bone Graft in Posterolateral Instrumented Lumbar Fusion for Degenerative Spinal Disorders, Spine, 43 (2018) E860-E868.

[216] M. Strnadová, Z. Strnad, P. Šponer, J. Jirošova, J. Strnad, In Vivo Behaviour of the Synthetic Porous Hydroxyapatite Prepared by Low Temperature Microwave Processing and Comparison with Deproteinized Bovine Bone, Key Engineering Materials, 493-494 (2012) 236-241.

[217] H. Yoshikawa, N. Tamai, T. Murase, A. Myoui, Interconnected porous hydroxyapatite ceramics for bone tissue engineering, J R Soc Interface, 6 (2009) S341-S348.

[218] M. Trouillas, M. Prat, C. Doucet, I. Ernou, C. Laplace-Builhé, P.S. Blancard, X. Holy, J.-J. Lataillade, A new platelet cryoprecipitate glue promoting bone formation after ectopic mesenchymal stromal cell-loaded biomaterial implantation in nude mice, Stem Cell Res Ther, 4 (2013) 1-1.

[219] P.M. Chopra, M. Johnson, T.R. Nagy, J.E. Lemons, Micro-computed tomographic analysis of bone healing subsequent to graft placement, Journal of Biomedical Materials Research Part B: Applied Biomaterials, 88B (2009) 611-618.

[220] P.G. Coelho, M.E. Coimbra, C. Ribeiro, E. Fancio, O. Higa, M. Suzuki, M. Marincola, Physico/chemical characterization and preliminary human histology assessment of a β-TCP particulate material for bone augmentation, Materials Science and Engineering: C, 29 (2009) 2085-2091.

[221] A.L.d.S. Fabris, L.P. Faverani, P.H.S. Gomes-Ferreira, T.O.B. Polo, J.F. Santiago-JÚNior, R. Okamoto, Bone repair access of BoneCeramic" in 5-mm defects: study on rat calvaria, J Appl Oral Sci, 26 (2018).

[222] E.R. Luvizuto, S. Tangl, G. Zanoni, T. Okamoto, C.K. Sonoda, R. Gruber, R. Okamoto, The effect of BMP-2 on the osteoconductive properties of β-tricalcium phosphate in rat calvaria defects, Biomaterials, 32 (2011) 3855-3861.

[223] G. Daculsi, E. Goyenvalle, E. Aguado, SPONGIOUS AND CORTICAL BONE SUBSTITUTION KINETICS AT THE EXPENSE OF MACROPOROUS BIPHASIC CALCIUM PHOSPHATE: ANIMAL AND HUMAN EVIDENCE, Bioceramics, WORLD SCIENTIFIC1999, pp. 287-290.

[224] P. Botez, P. Sirbu, L. Simion, F. Munteanu, I. Antoniac, Application of a biphasic macroporous synthetic bone substitutes CERAFORM®: clinical and histological results, European Journal of Orthopaedic Surgery & Traumatology, 19 (2009) 387-395.

[225] W. Ji, G. Kerckhofs, C. Geeroms, M. Marechal, L. Geris, F.P. Luyten, Deciphering the combined effect of bone morphogenetic protein 6 and calcium phosphate on bone formation capacity of periosteum derived cell-based tissue engineering constructs, Acta Biomater, 80 (2018) 97-107.

[226] S. Yamada, D. Heymann, J.M. Bouler, G. Daculsi, Osteoclastic resorption of calcium phosphate ceramics with different hydroxyapatite/β-tricalcium phosphate ratios, Biomaterials, 18 (1997) 1037-1041.

[227] S.D. Nunn, G.H. Kirby, Green Machining of Gelcast Ceramic Materlals, Proceedings of the 20th Annual Conference on Composites, Advanced Ceramics, Materials, and Structures—A: Ceramic Engineering and Science Proceedings, (1996) 209-213.

[228] J. Kastyl, Z. Chlup, P. Stastny, M. Trunec, Machinability and properties of zirconia ceramics prepared by gelcasting method, Adv Appl Ceram, (2019).

[229] A.R. Studart, U.T. Gonzenbach, E. Tervoort, L.J. Gauckler, Processing routes to macroporous ceramics: A review, J Am Ceram Soc, 89 (2006) 1771-1789.

[230] J.A. Lewis, Colloidal Processing of Ceramics, J Am Ceram Soc, 83 (2000) 2341-2359.

[231] X. Zhu, D. Jiang, S. Tan, Z. Zhang, Improvement in the Strut Thickness of Reticulated Porous Ceramics, J Am Ceram Soc, 84 (2001) 1654-1656.

[232] L. Ciocca, D. Donati, S. Ragazzini, B. Dozza, F. Rossi, M. Fantini, A. Spadari, N. Romagnoli, E. Landi, A. Tampieri, A. Piattelli, G. Iezzi, R. Scotti, Mesenchymal Stem Cells and Platelet Gel Improve Bone Deposition within CAD-CAM Custom-Made Ceramic HA Scaffolds for Condyle Substitution, Biomed Res Int, (2013).

[233] L. Ciocca, D. Donati, M. Fantini, E. Landi, A. Piattelli, G. Iezzi, A. Tampieri, A. Spadari, N. Romagnoli, R. Scotti, CAD-CAM-generated hydroxyapatite scaffold to replace the mandibular condyle in sheep: Preliminary results, J Biomater Appl, 28 (2013) 207-218.

[234] G. Staffa, A. Barbanera, A. Faiola, M. Fricia, P. Limoni, R. Mottaran, B. Zanotti, R. Stefini, Custom made bioceramic implants in complex and large cranial reconstruction: A two-year follow-up, J Cranio Maxill Surg, 40 (2012) E65-E70.

[235] J.D. Cawley, Solid freeform fabrication of ceramics, Current Opinion in Solid State and Materials Science, 4 (1999) 483-489.

[236] R. Detsch, S. Schaefer, U. Deisinger, G. Ziegler, H. Seitz, B. Leukers, In vitro-Osteoclastic Activity Studies on Surfaces of 3D Printed Calcium Phosphate Scaffolds, J Biomater Appl, 26 (2011) 359-380.

[237] R. Vaishya, M. Chauhan, A. Vaish, Bone cement, J Clin Orthop Trauma, 4 (2013) 157-163.

[238] O.O. Omatete, M.A. Janney, S.D. Nunn, Gelcasting: From laboratory development toward industrial production, J Eur Ceram Soc, 17 (1997) 407-413.

[239] X.J. Mao, S.Z. Shimai, M.J. Dong, S.W. Wang, Investigation of new epoxy resins for the gel casting of ceramics, J Am Ceram Soc, 91 (2008) 1354-1356.

[240] T. Kanzawa, H. Monma, Y. Moriyoshi, Reaction chemistry of hydroxyapatite: formation and decomposition, Proc. Est. Acad. Sci. Chem., 49 (2000) 19 - 28.

[241] A.L. Mori, Schalege.Ll, M.A. Porzio, Kinetics and Mechanism of Epoxy Ether Hydrolysis .1. Mechanism of Hydrolysis of an Acyclic Hemiacetal Intermediate, J Am Chem Soc, 94 (1972) 5034-&.

[242] O. Bera, M. Trunec, Optimization of Fine Alumina Gelcasting Using In Situ Dynamic Rheology, J Am Ceram Soc, 95 (2012) 2849-2856.

[243] G.W. Scherer, Theory of Drying, J Am Ceram Soc, 73 (1990) 3-14.

[244] F.F. Lange, M.M. Hirlinger, Hindrance of Grain-Growth in Al2o3 by Zro2 Inclusions, J Am Ceram Soc, 67 (1984) 164-168.

[245] M. Ebrahimi, M.G. Botelho, S.V. Dorozhkin, Biphasic calcium phosphates bioceramics (HA/TCP): Concept, physicochemical properties and the impact of standardization of study protocols in biomaterials research, Mat Sci Eng C-Mater, 71 (2017) 1293-1312.

[246] R.G. Carrodeguas, S. De Aza, alpha-Tricalcium phosphate: Synthesis, properties and biomedical applications, Acta Biomater, 7 (2011) 3536-3546.

[247] M. Tamai, R. Nakaoka, T. Tsuchiya, Cytotoxicity of various calcium phosphate ceramics, Bioceramics 18, Pts 1 and 2, 309-311 (2006) 263-266.

[248] J. Wiltfang, H.A. Merten, K.A. Schlegel, S. Schultze-Mosgau, F.R. Kloss, S. Rupprecht, P. Kessler, Degradation characteristics of alpha and beta tri-calcium- phosphate (TCP) in Minipigs, J Biomed Mater Res, 63 (2002) 115-121.